A Trapped Single Ion Inside a Bose-Einstein Condensate

This dissertation is submitted for the degree of Doctor of Philosophy

by

Christoph Zipkes

Robinson College

Cambridge, April 2011

This dissertation is my own work and contains nothing which is the outcome of work done in collaboration with others, except as specified in the text and/or acknowledgements. It has not been submitted in whole or in part for the award of a degree at the University of Cambridge or any other University. This thesis does not exceed the prescribed word limit of 60'000 words.

Abstract

In recent years, improved control of the motional and internal quantum states of ultracold neutral atoms and ions has opened intriguing possibilities for quantum simulation and quantum computation. Many-body effects have been explored with hundreds of thousands of quantum-degenerate neutral atoms and coherent light-matter interfaces have been built. Systems of single or a few trapped ions have been used to demonstrate universal quantum computing algorithms and to detect variations of fundamental constants in precision atomic clocks. Now in our experiment we investigate how the two systems can be advantageously combined. We immerse a single trapped Yb^+ ion in a Bose-Einstein condensate of Rb atoms. Our hybrid setup consists of a linear RF-Paul trap which is overlapped with a magnetic trap and an optical dipole trap for the neutral atoms.

A first synergetic effect is the sympathetic cooling of the trapped ions to very low temperatures through collisions with the ultracold neutral gas and thus without applying laser light to the ions. We observe the dynamics of this effect by measuring the mean ion energy after having an initially hot ion immersed into the condensate for various interaction times, while at the same time monitoring the effects of the collisions on the condensate. The observed ion cooling effect calls for further research into the possibility of using such hybrid systems for the continuous cooling of quantum computers.

To this end a good understanding of the fundamental interaction processes between the ion and the neutrals is essential. We investigate the energy dependent elastic scattering properties by measuring neutral atom losses and temperature increase from an ultracold thermal cloud of Rb. By comparison with a Monte-Carlo simulation we gain a deeper understanding of how the different parameters affect the collisional effects. Additionally, we observe charge exchange reactions at the single particle level and measure the energy-independent reaction rate constants. The reaction products are identified by in-trap mass spectrometry, revealing the branching ratio between radiative and non-radiative charge exchange processes.

Contents

Introduction

In recent years, large improvements in the control of quantum systems both for ultracold neutral atomic gases and trapped ions have been achieved.

The break-through event with neutral atomic gases has been accomplished in 1995 with the first creation of a Bose-Einstein condensate (BEC) of alkali atoms [1, 2]. This novel state of matter exhibits non-classical behaviour such as superfluidity [3, 4] and long range coherence [5, 6]. Being a quantum degenerate gas, it is well suited to study non classical many-body effects [7]. Also, the system is a promising candidate to perform quantum simulation [8, 9], and coherent light-matter interfaces have been built [10, 11].

Traps for few or single ions, which can confine electrically charged particles for extended times, have first been developed in 1958 [12, 13]. The long trapping times allow for various precision measurements such as the investigation of variations of fundamental constants with precision atomic clocks [14, 15]. Also, trapped ion systems are an auspicious candidate to perform quantum computation [16, 17, 18], fundamental quantum logic gates have been demonstrated [19, 20, 21, 22], and a complete set of operations for scalable ion trap quantum information processing have been implemented in a single system [23].

Until before this work, single ions and quantum degenerate gases have only been treated separately. Here, we investigate how these two systems can be advantageously combined into one such hybrid system. It has been anticipated that the combination of the two systems could allow continuous immersion cooling of trapped ions to very low temperatures [24, 25] or the local manipulation of a quantum degenerate gas using a single particle probe [26]. The general expectation is, that by combining two such advanced constituent systems, the synergies should be manifold, adding new experimental possibilities to each of the two systems and additionally generating new effects. In April 2009, we have successfully created the first overlap between a single trapped ion and a Bose-Einstein condensate and we have observed sympathetic cooling of the ion by the Bose-Einstein condensate [27]. Moreover, we have used the ion to measure local properties within the ultracold gas and have investigated chemical reactions at ultralow energies and at the single particle level [28]. Related experiments with ions and cold neutral atoms are also being conducted by other groups [29, 30, 31] and more are currently being set up.

For the quantum gas, the introduction of an impurity can have dramatic effects. In superconductors for example, impurities can profoundly affect the system's properties, both in

conventional [32, 33] and high-transition-temperature [34] superconductors. The distinguishability of the impurity can be used to detect structures within the medium it is immersed in. In liquid helium for instance, vortex lattices have been observed by using charged particles as markers [35]. For a trapped ion immersed in a quantum gas, scanning probe microscopy techniques have been suggested [26, 36]. Also, the ion could be used to locally manipulate the quantum gas [37]. For future investigations of quantum matter in combination with impurities, the degree of available control over the impurities is crucial. In this regard, the trapped ion system is highly promising.

For the trapped ion, the presence of an ultracold bath is expected to lead to sympathetic cooling [24, 38]. Immersion cooling has previously been successful with polar molecules [39] and nanomechanical resonators [40]. Moreover, it has been predicted that even internal degrees of ionic molecules could be cooled by an ultracold neutral gas [41]. Further, the entanglement between properties of the ion and the neutral atoms [42], possibly leading towards hybrid atom-ion quantum processors can be thought of. Also, the combined system might allow the study of decoherence of single, locally controlled impurities in a quantum environment [43, 44].

Collision processes between ions and neutral atoms at low energies play a decisive role in cold and ultracold chemistry. They have previously not been studied in detail experimentally, and they are essential to understand the physics in our hybrid system. Efficient sympathetic cooling relies on elastic collisions occurring at much higher rates than inelastic processes. The interaction between an ion and a neutral atom is dominated by the long range induced dipole potential, which decays with internuclear separation to the fourth power. Therefore, the collision cross-section is considerably larger than for the case of scattering between two neutral atoms [45, 46]. In a classical picture [47], collisions can be divided into two regimes. If the impact parameter is larger than a critical value b_c, the particle trajectory is only slightly deflected, leading to forward scattering. These collisions have only a negligible effect on sympathetic cooling of the ion. However, if the impact parameter is smaller than the critical value b_c, the particles approach each other to very close distances until they get reflected by the hard-core potential. These trajectories are deflected almost uniformly into any direction and lead to significant energy transfer between the colliding particles, see Fig. 1, and are therefore responsible for sympathetic cooling. Also, since the particles get very close during the collision, such that their electronic wavefunctions overlap significantly, inelastic processes are expected. The classical cross-section for the close encounter collisions can be defined by $\sigma = \pi b_c^2$, with the critical impact parameter $b_c = (2C_4/E_c)^{1/4}$. This leads to an energy-independent collision rate constant, which results in simplified system behaviour, which has been used for example in ion mobility spectrometry [49]. Alternatively, the quantum mechanical description of the collision process predicts an energy dependent collision rate, as it involves both forward scattering and close-encounter events. At very low collision energies, where only few partial waves contribute, the interaction strength might become tunable with atom-ion Feshbach resonances [50, 51].

Inelastic collisions involve charge exchange [52, 24, 45, 53, 54, 51, 55], spin exchange [24]

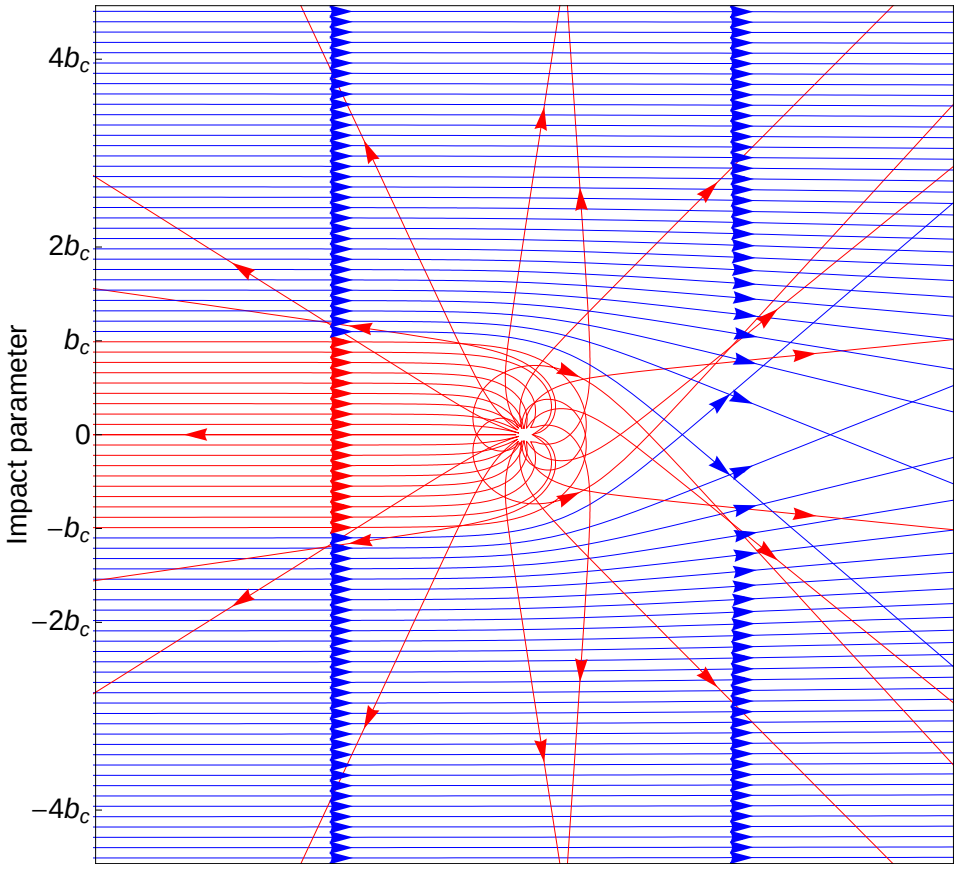

Figure 1: Classical trajectories in the C_4 potential [48]. The Langevin cross-section accounts for all trajectories with an impact parameter smaller than $b_c = (2C_4/E_c)^{1/4}$ (red), while forward scattering (blue) is neglected.

and formation of molecules [56], which lead into the field of ultracold chemistry [57]. In neutral atomic systems, at ultralow temperatures, atom-molecule coherence in dimers [58], the formation of trimers [59], and polar molecules [60] have been observed. Molecular ions have the advantage that they can be trapped for long times, allowing to perform precise measurements on them, such as mass spectrometry [61, 62, 63, 64, 65]. Ion-neutral chemical reactions are also thought to play an important role in explaining the composition of the interstellar gas [66]. So far, such chemical reactions have been investigated between trapped ions and a hot neutral gas [67, 62, 63]. Due to both reactants being at ultralow temperatures, the new hybrid system might open the way to control the chemical reaction paths on the quantum level.

This thesis describes measurements we have conducted on the new hybrid system with a Yb^+ ion immersed in a ^{87}Rb Bose-Einstein condensate. In chapter 1 and chapter 2 the experimental setup is described. Chapter 3 introduces all the methods which have been used in the experiments. Chapter 4 discusses the experimental results. They include the observation of sympathetic cooling, effects on the Bose-Einstein condensate, the influence of micromotion, and the measured rates and reaction channels of inelastic collisions. Chapter 5 describes

the Monte-Carlo simulation which has been written to explain the experimental observations with elastic collisions. The role of micromotion, the ion-neutral mass-ratio and the applied cross-section model are investigated.

List of Publications

C. Zipkes, L. Ratschbacher, C. Sias, M. Köhl
Kinetics of a single trapped ion in an ultracold buffer gas
New J. Phys. 13, 053020 (2011).

C. Zipkes, S. Palzer, L. Ratschbacher, C. Sias, M. Köhl
Cold heteronuclear atom-ion collisions
Phys. Rev. Lett. 105, 133201 (2010).

C. Zipkes, S. Palzer, C. Sias, M. Köhl
A trapped single ion inside a Bose-Einstein condensate
Nature, 464, 388-391 (2010).

S. Palzer, C. Zipkes, C. Sias, M. Köhl
Quantum transport through a Tonks-Girardeau gas
Phys. Rev. Lett. 103, 150601 (2009).

Chapter 1

Experimental Setup

This chapter gives an overview of our experimental apparatus. The setup to create a Bose-Einstein condensate will be described in brief. The ion trap with its specific features to fit in the hybrid system and our ion loading technique will be explained, and the laser setup will be introduced.

1.1 Bose-Einstein Condensate

We create Bose-Einstein condensates of ^{87}Rb in a two compartment vacuum chamber, shown in Fig. 1.1. The first section of the vacuum chamber is used to magneto-optically trap (MOT) [68] the atoms from a background pressure of approximately 10^{-9} mbar. This background pressure is sustained by firing Rb-dispensers for about 20 s per experimental cycle of 80 s length. The loading of the MOT with 10^9 atoms takes somewhat more than 20 s. Next, the magnetic field

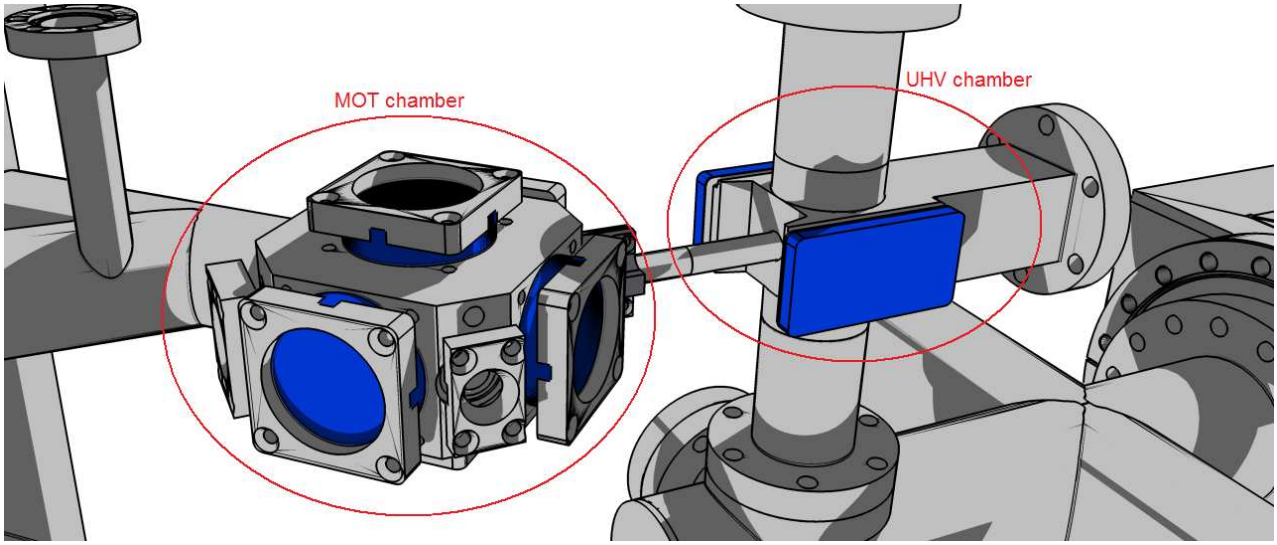

Figure 1.1: Section of the vacuum chamber showing the chamber of the magneto-optical trap (MOT) connected to the ultrahigh vacuum chamber (UHV) via a differential pumping tube. Stainless steel parts are shown in grey, windows are depicted in blue.

is turned off to cool the atoms further in an optical molasses for which the cooling light is further detuned ($-6\,\Gamma$) and its intensity reduced. Then the atoms are optically pumped into the $F = 2$, $m_F = 2$ hyperfine state to confine and compress them in a magnetic quadrupole field. The atoms are transported over a distance of 140 mm into the second section of the vacuum chamber by tuning the currents of three overlapping quadrupole coil pairs. This second part of the vacuum chamber, connected to the MOT chamber by a differential pumping tube, has a much lower background pressure of about $2 \cdot 10^{-11}$ mbar. The lower pressure is required to keep the atom losses, induced by collisions with the background gas, low during the evaporative cooling process. A QUIC trap [69] is used to avoid atom losses by nonadiabatic spin flips. Evaporative cooling [70, 71] can be controlled either with RF frequencies in the range from 25 MHz to 1 MHz, driving transitions between different m_F states, or by using microwave frequencies between 6.9 GHz and 6.8 GHz, driving transitions between the different F ground states, see Fig. 1.2. The evaporative cooling process in the magnetic trap takes about 35 s until the atoms start to Bose-Einstein condense. Alternatively, the atoms can be loaded into an optical dipole trap shortly before they reach quantum degeneracy, and the last step of evaporation is then achieved by lowering the optical confinement.

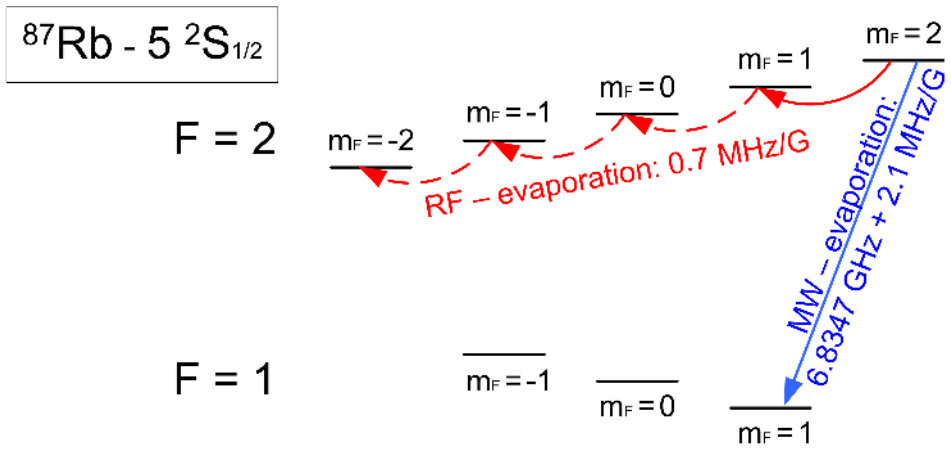

Figure 1.2: Zeeman levels of the ^{87}Rb ground state. Evaporation is achieved either by applying radio-frequency (red) to couple the different Zeeman levels of the $F = 2$ hyperfine state, or by applying microwave (blue) to couple to the $F = 1$ hyperfine state.

With the described apparatus we created our first MOT in November 2007 and the first Bose-Einstein condensate in April 2008. An experiment of quantum transport in a one-dimensional system [72] has been setup and measurements taken, mainly by Carlo Sias, until February 2009. The BEC setup, which has been described here only in brief, is explained in more detail in [73].

In the meanwhile the ion trap has been set up and tested. Our ion trap design will be introduced in the next section.

1.2 Ion Trap Design

We started designing our ion trap system shortly after the creation of our first Rb-MOT in November 2007. While Stefan Palzer has been responsible for the planning and building of the laser system, to cool and probe the Yb ion (a short overview will be given in section 1.4), I have set up the ion trap with control electronics and software. The design of the trap and its part of the vacuum chamber has been mostly complete by the end of 2007. Assembly started in June 2008, after all parts had been manufactured or delivered. By November 2008 we trapped our first Yb ions in the test setup, which was not yet connected to the vacuum chamber of the BEC setup. In February 2009 we joined the two systems, the ion trap and the BEC setup, to start the first measurements of a single trapped ion immersed in the BEC in April 2009. In this section, the ion trap design will be described, with a special focus on the considerations required for combining the ion trap with the BEC apparatus.

1.2.1 Pseudopotential Approximation

The general equation of motion for a charged particle in the electric field $\vec{E}(\vec{r},t)$ is given by

$$m\,\ddot{\vec{r}} = Q\,\vec{E}(\vec{r},t) \tag{1.1}$$

where m is the mass of the ion and Q its charge. According to Earnshaw's theorem, with only static electric fields $\vec{E}(\vec{r})$ no ions can be trapped. Nevertheless, in oscillating fields it is possible [13, 74] and a pseudopotential can be derived for the motion of the ion (cf. [75, 76]). The electric field is assumed to be oscillating with one frequency Ω_T only and having a spatial distribution described by $\vec{E}_0(\vec{r})$.

$$\vec{E}(\vec{r},t) = \vec{E}_0(\vec{r}) \cdot \sin(\Omega_T\, t) \tag{1.2}$$

Because of the oscillatory behavior of the field the mean force on the particle over one period $2\pi/\Omega_T$ is much smaller than the peak force in (1.1). Therefore one assumes the position $\vec{r}$ of the ion to consist of a mean position $\vec{r}_m$ and an oscillatory deviation from the mean position $\delta\vec{r}$

$$\vec{r} = \vec{r}_m + \delta\vec{r}\ \ . \tag{1.3}$$

The equation of motion (1.1) is then solved by (1.3) with

$$\delta\vec{r} = -\frac{Q\,\vec{E}_0(\vec{r})}{m\,\Omega_T^2} \cdot \sin(\Omega_T\, t)\ . \tag{1.4}$$

The electric field $\vec{E}_0(\vec{r})$ is linearly approximated by

$$\vec{E}_0(\vec{r}) = \vec{E}_0(\vec{r}_m) + \delta\vec{r}\left[\frac{\partial\vec{E}_0(\vec{r})}{\partial\vec{r}}\right]_{\vec{r}=\vec{r}_m} . \tag{1.5}$$

Now the mean force on the ion over one oscillatory period $2\pi/\Omega_T$ is calculated,

$$\vec{F}(\vec{r}_m) = \left\langle \vec{F}(\vec{r}) \right\rangle = Q\left\langle \vec{E}(\vec{r}) \right\rangle = Q\left[\frac{\partial\vec{E}_0(\vec{r})}{\partial\vec{r}}\right]_{\vec{r}=\vec{r}_m} \frac{Q\,\vec{E}_0(\vec{r})}{2\,m\,\Omega_T^2} . \tag{1.6}$$

With the usual convention

$$\vec{F}(\vec{r}_m) = -\vec{\nabla}U(\vec{r}_m) \tag{1.7}$$

the pseudopotential $U(\vec{r}_m)$ can now be defined as

$$U(\vec{r}_m) = \frac{Q^2\vec{E}_0^2(\vec{r}_m)}{4\,m\,\Omega_T^2} . \tag{1.8}$$

This result of the pseudo potential approximation is for a general electric field geometry and the motion an ion exhibits due to $U(\vec{r}_m)$ is usually termed secular motion.

1.2.2 Linear RF-Quadrupole Trap Potential

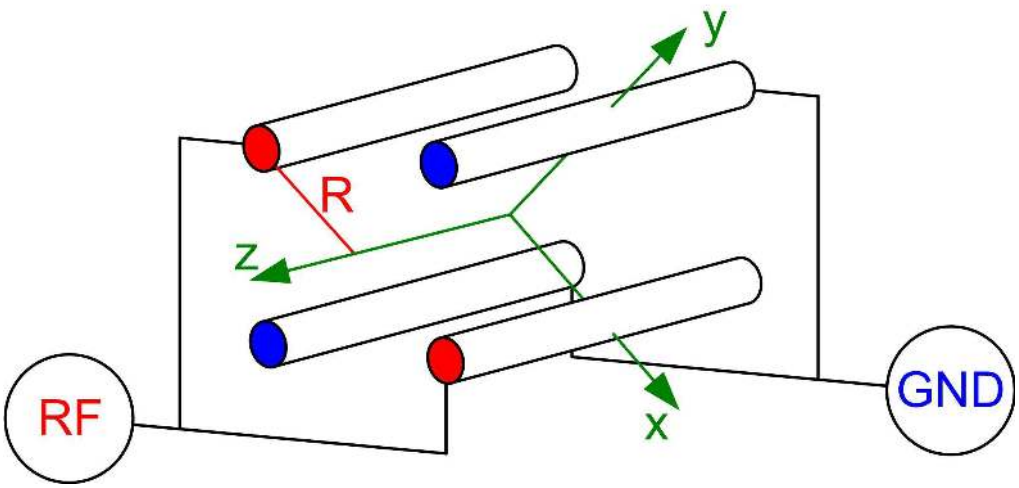

Figure 1.3: Schematic configuration of the trap electrodes. Four parallel rods define an electric field with a dominating quadrupole term in the centre of the trap. Two opposing rods are on an oscillating electric potential (RF) the other two on ground (GND). The distance from the centre of the trap to the surface of an electrode is R.

In the linear Paul trap configuration, which we use in our experiment, the electric RF potential is defined by four electrodes arranged as in Fig. 1.3, with the diagonally opposing electrodes being on the same voltage. The applied voltage difference between the two diagonal

electrode pairs is $V_0 \cdot \sin(\Omega_T\, t)$. In the central region of the trap the electric potential can then be approximated by the quadrupole

$$\Phi_{RF}(\vec{r}, t) = \frac{V_0}{2}\left(c + \frac{x^2 - y^2}{R^2}\right) \cdot \sin(\Omega_T\, t) \tag{1.9}$$

where R is the distance from the centre of the trap to the surface of the electrode, x and y are the coordinates pointing towards the electrodes, and V_0 is the voltage amplitude between the electrode pairs. c is equal to one for the configuration where one electrode pair is set to ground as shown in Fig. 1.3. Independent of this common mode c, the relevant electric field is

$$\vec{E}_0(\vec{r}) = \frac{V_0}{R^2}\begin{pmatrix} x \\ -y \\ 0 \end{pmatrix} . \tag{1.10}$$

In combination with equation (1.8) the corresponding pseudopotential is

$$U(\vec{r}_m) = \frac{Q^2\, V_0^2}{4\, m\, R^4\, \Omega_T^2}\left(x_m^2 + y_m^2\right) . \tag{1.11}$$

This potential is harmonic in the region where the electric potential $\Phi(\vec{r}, t)$ can be assumed to follow the quadrupole shape of Eqn. (1.9). The pure radial trap frequency in the absence of any confinement along the axial direction is

$$\omega_p = \frac{Q}{\sqrt{2}\, m}\, \frac{V_0}{R^2\, \Omega_T} . \tag{1.12}$$

Longitudinal confinement is obtained by adding a static electric quadrupole potential of the form

$$\Phi_{static}(\vec{r}) = \frac{V_{dccL}}{d_{ec}^2}(2z^2 - x^2 - y^2) , \tag{1.13}$$

with V_{dccL} typically being a voltage applied to some end-cap electrodes which are separated by a distance d_{ec}. In the combined ion trap potential $U(\vec{r}_m) + Q\, \Phi_{static}(\vec{r}_m)$, the longitudinal confinement lowers the radial trapping frequencies, which if exaggerated renders the ion trap unstable. Additionally, electric potentials due to accumulated static charges present in an experimental environment are likely to lift the degeneracy between the two radial trapping frequencies and also to rotate the main trapping axes away from the coordinate system suggested by the trap electrode geometry.

The description of the ion's motion in the RF-trapping field is given here only in the pseudo-potential approximation. A more exact description is given by the solutions to the Mathieu equations [74, 75, 76], which also provide information on the stability of the ion trap for different mass to charge ratios. A link between the pseudo potential approximation and the stability parameters a and q of the Mathieu equations will be given later in chapter 5.

1.2.3 Offset Fields and Micromotion

The presence of static charges or stray fields will also shift the position of the ion away from the trap symmetry axis where the RF field amplitude is zero and will lead to excess micromotion. To control it, electric compensation fields need to be applied in the radial direction.

Micromotion is used here as a general term for any oscillatory motion of the ion at the frequency Ω_T of the RF driving field. In a homogeneous RF-field, it is simply the difference between the real ion position and its time average, or $\delta\vec{r}$ as defined in Eqn. (1.3). The amplitude of that micromotion evaluates with Eqn. (1.4) to

$$\vec{a}_{mm} = \frac{Q\,\vec{E}_0(\vec{r}_m)}{m\,\Omega_T^2}\ . \tag{1.14}$$

Intrinsic micromotion is the micromotion the ion undergoes in a trap with perfect field compensation. Its amplitude is calculated by using the quadrupole field for $\vec{E}_0(\vec{r}_m)$ in Eqn. (1.14). If the ion was at rest in the centre of the trap $\vec{r}_{m_0}$ there would be zero intrinsic micromotion. However, in the presence of uncompensated static electric fields the micromotion in the centre of the trap is non-zero, and termed excess micromotion. To evaluate its amplitude we first calculate the displacement $\Delta\vec{r}_{m_0}$ of the trap centre caused by the static offset field $\vec{E}_{\text{Offset}}$. In its presence, the new trap potential is

$$U(\vec{r}_m) = \frac{Q^2\,\vec{E}_0^2(\vec{r}_m)}{4\,m\,\Omega_T^2} + Q\,\vec{E}_{\text{Offset}}\,\vec{r}_m\ . \tag{1.15}$$

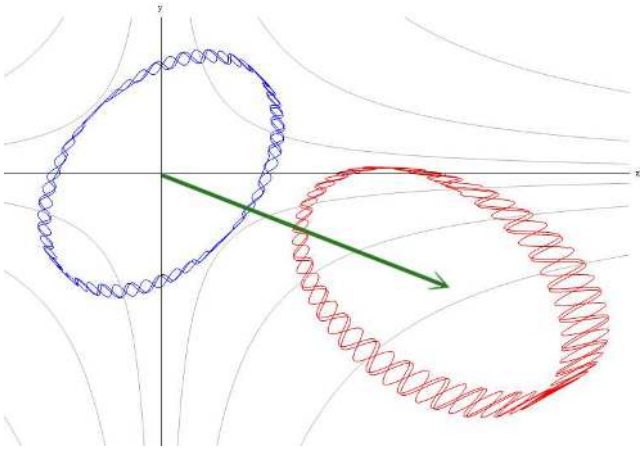

Figure 1.4: Numerically calculated ion trajectories for compensated electric offset fields (blue) and for an uncompensated field (red). The displacement of the ion trap centre $\Delta\vec{r}_{m_0}$ is indicated by the green arrow. Field lines of the RF-electric quadrupole are shown in grey.

In the special case where this offset term is added to the linear quadrupole field given in (1.10), with $\vec{E}_{\text{Offset}}$ pointing in the radial direction, the position of the minimum $\vec{r}_{m_0}$ of $U(\vec{r_m})$ shifts by

$$\Delta\vec{r}_{m_0} = \frac{2\,m}{Q}\,\frac{\vec{E}_{\text{Offset}}\,\Omega_T^2\,R^4}{V_0^2} \tag{1.16}$$

which results in an excess micromotion amplitude of

$$|\vec{a}_{mm,e}| = \frac{2\,\left|\vec{E}_{\text{Offset}}\right|\,R^2}{V_0}\ . \tag{1.17}$$

Note that the direction of $\vec{a}_{mm,e}$ is the same as the direction of $\vec{E}_0(\vec{r}_{m_0})$, and not the direction of $\vec{E}_{\text{Offset}}$.

For illustration of the secular motion and the micromotion, Fig. 1.4 shows two possible ion

trajectories calculated by numerically solving the equation of motion (1.1). In the first case, the applied electric field is given by the RF-quadrupole while in the second case a static offset field is added, as in Eqn. (1.15). The centre of the RF-field stays in its position and the shift $\Delta\vec{r}_{m_0}$ of the trap centre can be seen, indicated by the green arrow.

Micromotion and in particular the excess micromotion play a crucial role in the collision dynamics between a trapped ion and an ultracold neutral gas. Therefore a good electric field compensation is essential. We apply compensation voltages directly to the RF-electrodes by adding a DC-offset. The electronics required to do so will be explained in section 2.4, while the method to detect excess micromotion and the procedure to optimize the electric offset fields will be described in section 3.2. Observed effects depending on micromotion will be presented in section 4 and explained in section 5.1.

1.2.4 BEC Compatible Ion Trap Design and Assembly

The prerequisites set by the form of the previously installed BEC vacuum chamber and the needed spatial access, to transport the neutral atoms into the ion trap, for laser beams to set up an optical dipole trap, and to do absorption imaging after time of flight have set a number of constraints on the design of our ion trap. Also, we decided to first set up a small vacuum chamber on its own, to test the ion trap separately, while at the same time being able to do experiments with the BEC. This has set additional demands to the design of the ion trap side of the vacuum chamber and its supporting structure. Moreover, the condensation of a Bose gas can only be achieved with a low vacuum background pressure, requiring all the materials of the ion trap being ultrahigh-vacuum (UHV) compatible. A special loading procedure had to be thought of, explained in section 1.3, as the high temperature, the Yb needs to acquire a sufficient vapour pressure for trap loading, also negatively affects the UHV. The access port to connect the ion trap setup to the UHV vacuum chamber is a CF35 flange (seen in Fig. 1.1 on the right side of the UHV chamber). The distance from there to the centre of the magnetic trap, where the BEC can be produced, is about 100 mm. The access port has a square shaped cross-section with a side length of 30 mm. The ion trap is mounted on a copper holder with a slightly smaller cross-section, see Fig. 1.5. The ion trap head needs to be centred on the location of the BEC. To this end, the copper holder can be steered, similar as a mirror holder, with four adjustment screws on its one side. Copper has been used as material for the holder, to additionally provide efficient thermal and electrical grounding.

The ion trap head consists of the four RF-trap electrodes, the two end-cap electrodes, and pieces of ceramics, see Fig. 1.6. The six electrodes are made from beryllium-copper, which is much harder than copper but suffers less from oxidization when exposed to air during assembly, and with a similar electric and heat conductivity as copper. Also, it is non-magnetic, which is important as the ultracold neutral atoms will be located just a few 100 μm away from the electrodes. The ceramic parts are made from an aluminium nitride (*Shapal-M*), with good electrical isolation and heat conductivity properties, and with a low dielectric constant and

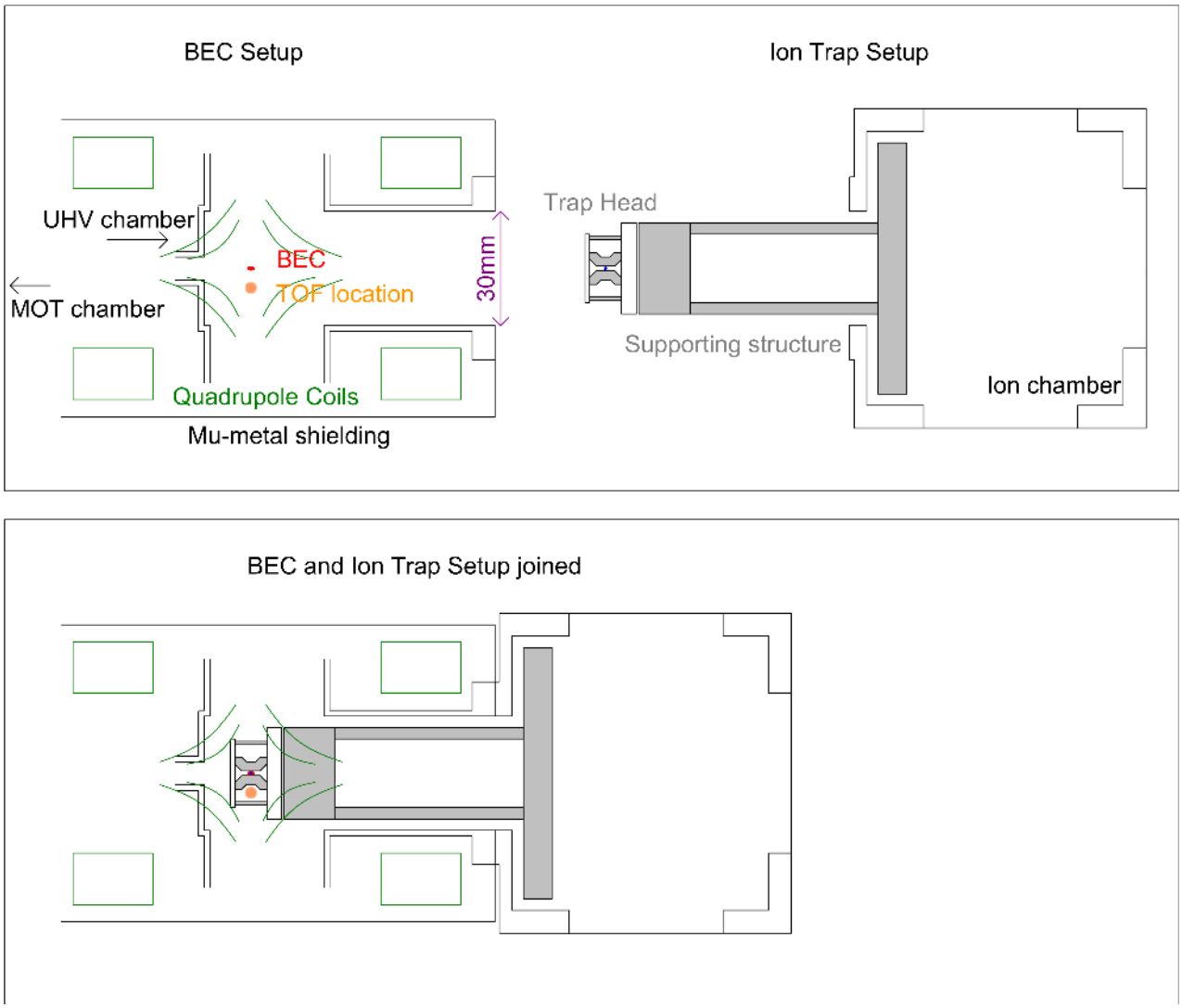

Figure 1.5: The BEC chamber and the ion trap setup are first shown separated (above), then joined together (below). Note the special shape of the trap electrodes to enable imaging the cold atomic cloud in time of flight (TOF). The BEC is brought into the ion trap from the left side by changing the magnetic confinement fields, thus a magnetic transport.

loss tangent. A compilation of the detailed material properties of Shapal-M and other ceramic materials considered for our setup, can be found in Appendix C.

The shape of our RF-electrodes is inspired by the Innsbruck design of blade shaped ion trap electrodes [77]. To allow optical access to the neutral atoms after about 25 ms time of flight (TOF), our electrodes need a clearance at the corresponding position. This is schematically indicated in Fig. 1.5 with the TOF location, the actual shape of the electrodes can be seen in Fig. 1.6 or Fig. 1.7. The electrodes on the upper side have the same clearance to keep the trap symmetric. The four electrodes have a minimal distance of 466 μm from the trap symmetry axis, which corresponds to the parameter R in Eqn. (1.9). Their knife edges are of cylindrical shape with a radius of 100 μm. Along the horizontal or vertical direction, the gap between the electrodes

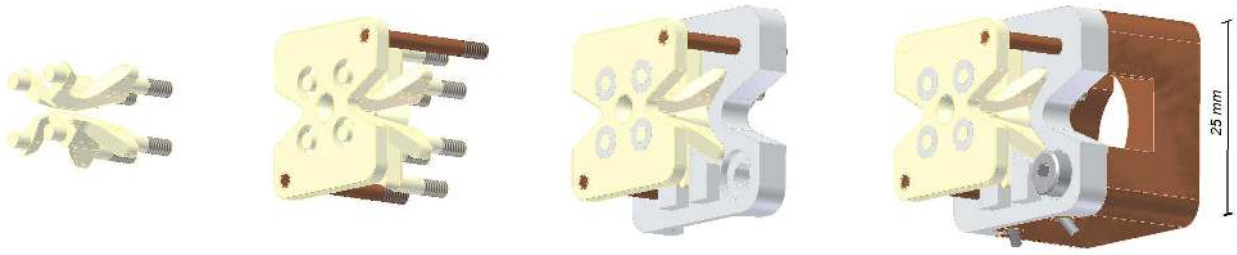

Figure 1.6: Shown is the ion trap head, in a) the four electrodes in their position, in b) the end cap electrodes are added, in c) the ceramic sheet on the right side and the four ceramic washers on the left between the end cap and the electrodes. d) shows the trap mounted to the copper block which itself is then connected to the vacuum chamber as shown in Fig. 1.9

has a size of 600 μm. The end-cap electrodes have a conical shape with a bore through its centre. The tips of the two end-caps are separated by 4.33 mm and the bores have a diameter of 700 μm. All the dimensions specified here are by design, the actual values in the experiment might vary on the order of a few 10 μm, limited by manufacturing tolerances.

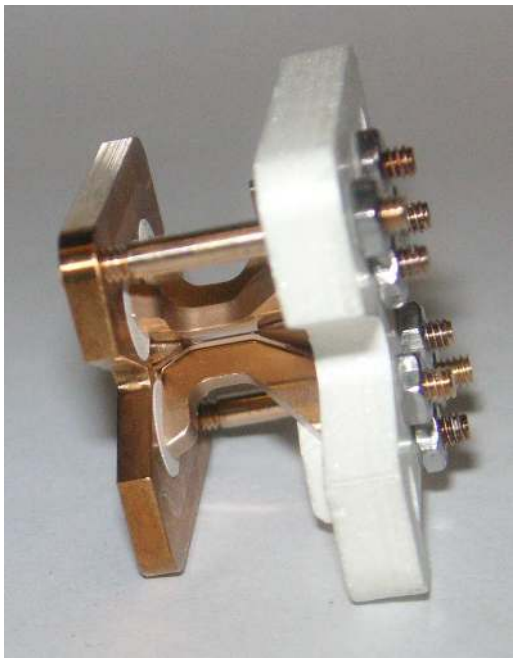

Figure 1.7: Image of the ion trap head taken during assembly.

Implementing external cooling of the ion trap structure has initially been motivated by the work of [78], where a strong dependence of the ion heating rate on the temperature of the trap electrodes has been observed. Additionally, we expect our system to drift less due to thermal expansion of the supporting structure if we can control its temperature externally. To this end, the copper holder of the ion trap is mounted to a copper ring with an integrated loop of copper tubing, which connects to a liquid feedthrough at the top of the vacuum chamber. The copper ring is fixed to the vacuum chamber with long stainless steel screws and spacers made from a plastic with low heat conductivity (*Vespel*), to provide only little thermal contact between the ion trap structure and the vacuum chamber. Special care has been taken in the design of the coolant tubing. To avoid damage to the structure from thermal stresses, the tubes have some extra bendings for length compensation. The feedthrough should allow the use of coolants with temperatures as low as −95 °C. However, we have never tried to cool the setup to such low temperatures and today we usually operate at 5 °C. The copper ring is best seen in Fig. 1.9a, the bending of the tubes in Fig. 1.9b. To monitor the temperature of the ion trap, two probes (PT100) are glued to the trap head (cf. Fig. 1.11).

The cooling efficiency between the trap head and the cooling liquid is calculated to be on the order of 350 mW/K [79]. With the sensors we detect a temperature increase of less than 100 mK when the ion trap is turned on, from which we conclude that there is less than 35 mW heat dissipated, by ohmic resistance within the electrodes, and dielectric losses in the ceramics.

Figure 1.8: Image of the experiment setup just before joining the ion trap chamber, on the right side of the image, with the BEC part, on the left side.

The part of the vacuum chamber which holds the ion trap consists of a custom made stainless steel cube with seven access ports with a standard CF63 cross connected to the top of it. One other access port is used for a viewport to allow optical access along the ion trap symmetry axis. Three access ports are used for electrical feedthroughs, to connect the trap electrodes, the Yb-ovens and the temperature probes. The two ports on the sides of the CF63 cross are connected to an ion getter pump and to a titanium sublimator, which has been home-built for it to fit next to the coolant tubing. A drawing of the described ion vacuum chamber is shown in Fig. 1.9c, and a picture of the actual setup is shown in Fig. 1.8. In the test setup, before joining the ion trap with the BEC apparatus, we used a small vacuum chamber with five viewports, a pressure gauge and a valve for initial vacuum pumping, shown in Fig. 1.9d.

The Z-shaped legs of the ion trap vacuum chamber, seen in Fig. 1.9c, were necessary for them to fit around the big ion getter pump of the UHV-chamber, as can be seen in Fig. 1.8. Conveniently, a breadboard has directly been fixed to these legs, to mount some of the ion trap optics. The legs stand on two baseplates, which themselves are lifted from the experiment table with four M6 screws. This allows a fine adjustment of the relative position between the two vacuum chambers, before the central combining flange gets closed. The final alignment of the ion trap position has been guided by a laser previously pointed at the BEC, which had to pass through the end-cap bores after a successful positioning of the ion trap.

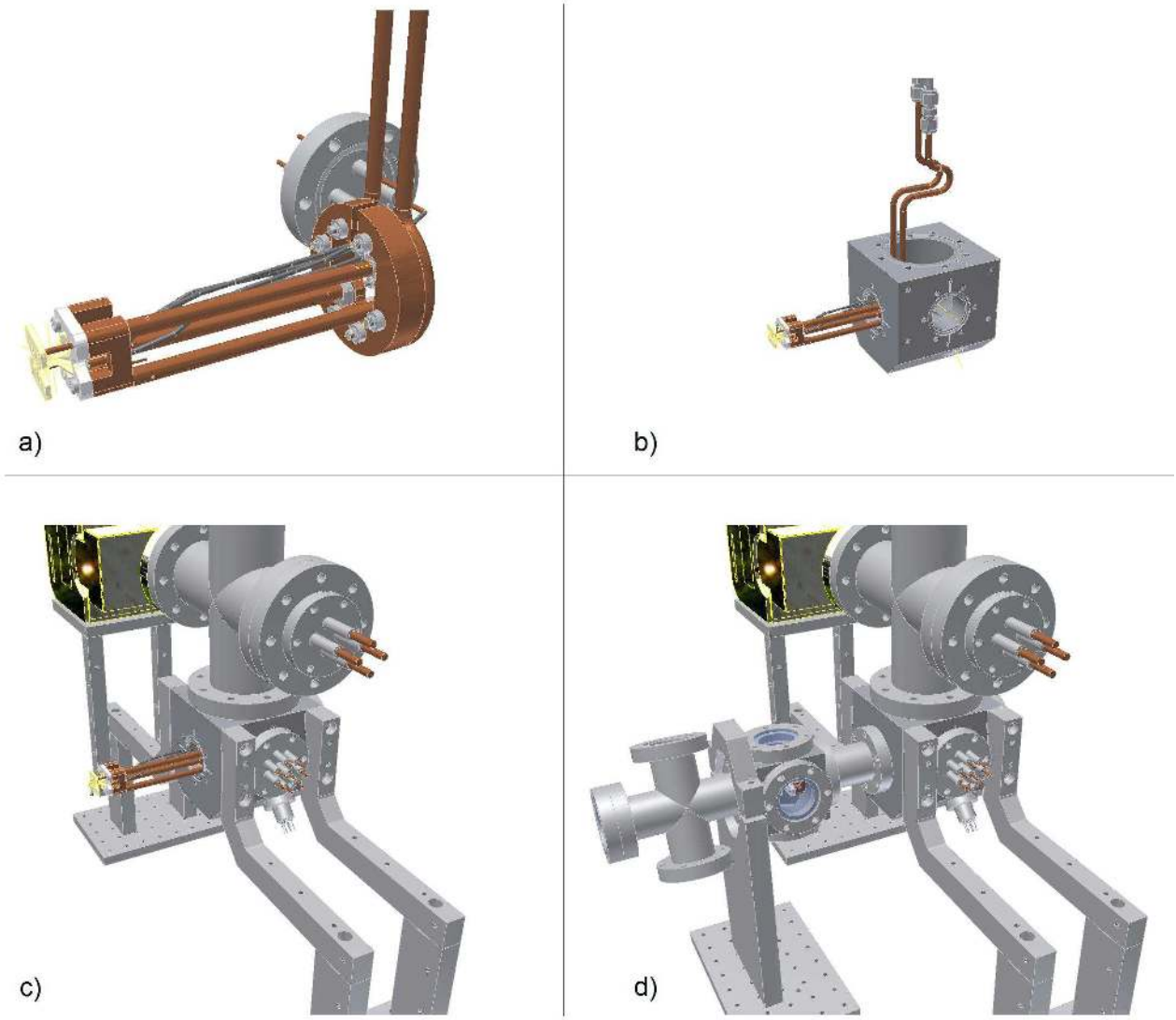

Figure 1.9: The ion trap setup is shown in four different levels of detail. In a) the trap head on the left is connected via three copper rods to the cooling ring. The copper tubes pointing upwards deliver the coolant to the ring. The electrodes are connected with silver wires to the high voltage feedthrough in the back. The cooling ring is screwed to the stainless steel cube seen in b). *Vespel* rings between the cooling ring and the stainless steel are put in place for thermal isolation. In c) the cube vacuum chamber is mounted to the four Z-shaped legs. A CF-63 cross with ion getter pump at the back and titanium sublimator at the front is put on top of the cube chamber. On top of the cross the cooling liquid feedthrough is located (not shown in figure) where the coolant tubes connect to. In d) the test vacuum chamber is added with four viewports to provide optical access to the trap. The two loose ends on the left side of the test chamber are used for a pressure gauge and to connect the turbo molecular pump during initial evacuation and bake-out.

1.3 Yb Oven Design

1.3.1 Loading Techniques

In other ion trapping experiments some different ways of loading the trap have been tested and used. One, for a long time preferred method was to ionize atoms by electron impact using an electron beam [80]. By doing so, multiply charged ions can be produced and the ionization process is not selective for species of atoms and isotopes. Another method is to use lasers to ionize atoms by photo-ionization. By using a two photon process the ionization can be done isotope selectively [81], where the first photon drives the neutral atom into an excited state and the second photon takes one electron from the excited state to the continuum. The first transition into the excited, but yet bound state provides the isotope-selectivity if the frequency-shifts between the transitions of different isotopes can be spectroscopically resolved. For the ionization of Yb, a laser at 398 nm is used to pump the neutral Yb on the $^1S_0$ - $^1P_1$ transition. The second photon needs to be of wavelength shorter than 394 nm in order to ionize the Yb atom to the ground state of the Yb^+ ion. Therefore the laser light for the ion cooling transition at 369.5 nm is suitable to ionize the Yb atoms from the $^1P_1$ state.

1.3.2 Isotope Selective Loading

To enable isotope selective loading two conditions need to be fulfilled. The resonances of the different isotopes must be separated by more than both the natural linewidth of the transition and the Doppler broadening given by the atoms velocity distribution along the ionization laser axis. The second condition is that the laser can be stabilized on the selected transition and the laser linewidth being small enough to resolve the resonance lines of the different isotopes. For Yb the natural linewidth of the $^1S_0$ - $^1P_1$ transition is on the order of 28 MHz while the separation between resonances of different isotopes is in the 100 MHz range [82]. Roughly calculated, this means that the velocity distribution should be smaller than 20 m/s. This can be achieved by collimating an atom beam from a hot atom source and pointing the atom beam perpendicular to the isotope selective laser. In [83] a small metal tube is used as an oven, the tube is heated at the lower end where the Yb is and kept cool at the other end to collimate the atomic beam. For isotopic selective loading of Yb it should be sufficient if the angle of divergence of the atomic beam is smaller than 5 ° assuming the oven temperature is kept below 1000 K.

1.3.3 Oven Design

Our oven design is mostly inspired by the work of [83]. A small stainless steel tube of 1.4 mm diameter and 4 mm length contains a small amount of Yb with a natural abundance isotope distribution. The top end of the small tube is held by a much larger copper piece acting as

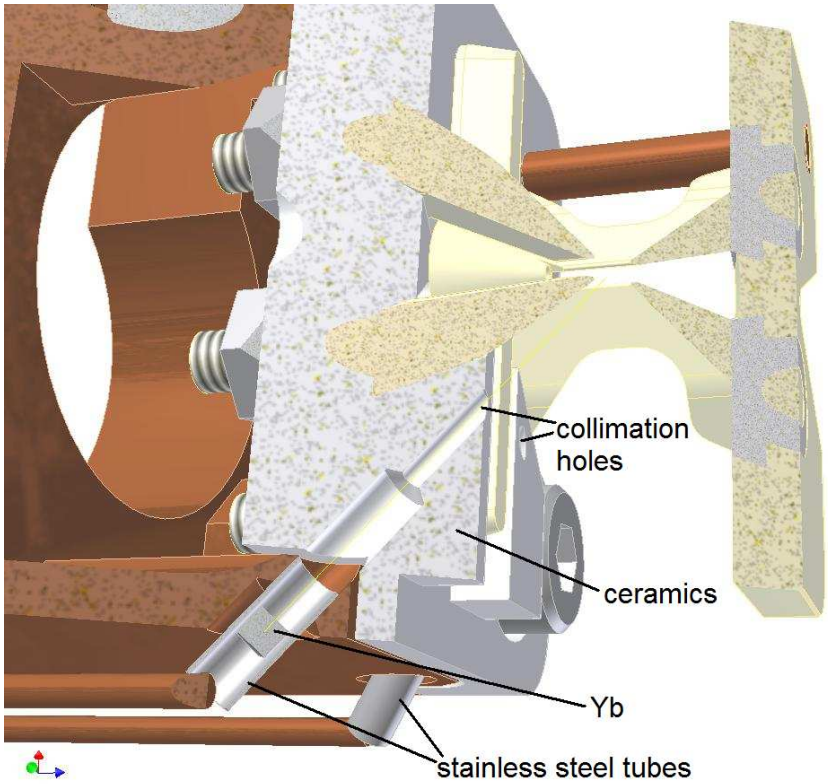

Figure 1.10: Shown is a section view of the Yb oven for loading the ion trap. A copper wire (lower left) connects to a stainless steel tube that contains a small Yb block with a natural abundance isotope distribution. The stainless steel tube fits into the large copper piece that supports the ion trap. The atomic beam coming out of the oven is collimated by the smaller hole in the ceramic part in front of the oven. The beam points to the centre of the trap where the atoms can be photo-ionized.

both thermal and electric ground. A *Kapton* isolated copper wire connects to the lower end of the stainless steel tube to deliver the current needed to heat the oven.

One major constraint in our setup is the limitation on space. Since the whole ion trap setup has to fit into the BEC vacuum chamber the length of the oven was limited to a maximum of 4 mm. The collimation that could be achieved with only this short stainless steel tube would not have been sufficient for isotope selective loading of the trap. Therefore an additional collimation is provided by a small hole ($\varnothing = 0.5$mm) in the ceramic part that supports the ion trap. Also, there is no direct thermal contact between the oven and the collimating ceramic part which can lead to a better collimation if the ceramic part is colder than the copper part. The oven setup is illustrated in Fig. 1.10 .

The orientation of the oven is such that the velocity of the collimated atomic beam is perpendicular to the 398 nm laser which crosses the ion trap in the horizontal plane at an angle of 60 ° relative to the trap axis. It also needs to point upwards such that the Yb, which might become liquid, does not fall out of the oven. The lower end of the oven is sealed by crimping as described in [83].

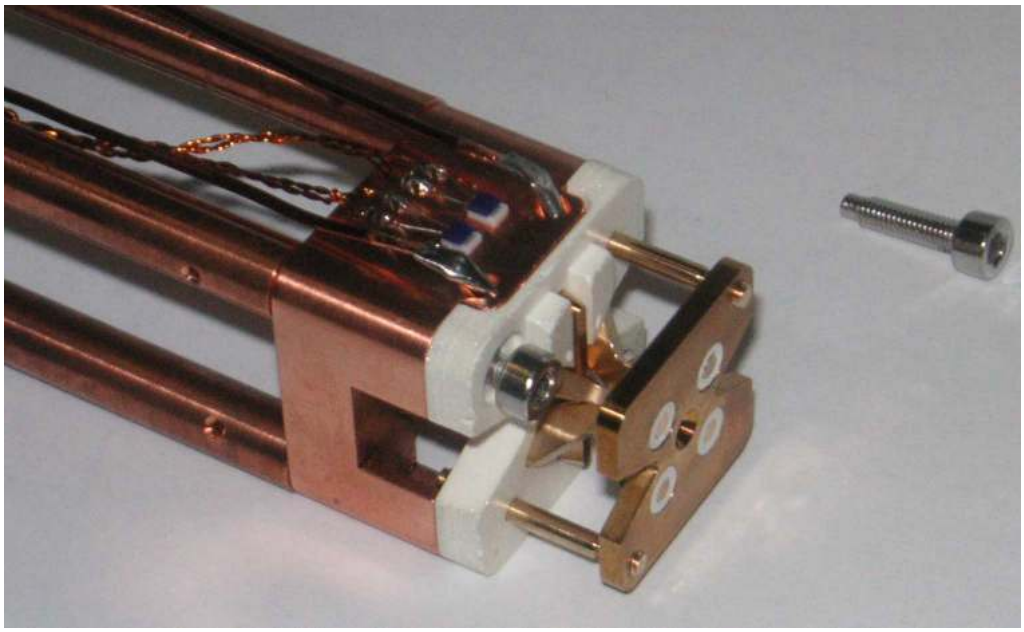

Figure 1.11: Image of the ion trap head during assembly, seen from the bottom. This view shows the two Yb ovens and how they are connected to the copper wire. The Yb beam collimation bore can be seen at the point where the atoms will exit from the ceramic part. In between the ovens, two temperature sensors of the type PT100 have been placed.

Two separate but identical ovens are built into our setup. This allows, in the case of failure or depletion of one of the ovens, to use the second oven without opening the vacuum. As the two ovens provide atoms moving along different vectors, the laser axis for Doppler free photo-ionization changes in that case.

1.3.4 Calculation of Temperature Increase

Usually ovens for loading ion traps are being heated for several minutes with a few amperes to reach a temperature where they evaporate enough atoms for the trap to be loaded. This scheme was not directly applicable to our experiment because the high temperature of the oven over a few minutes could easily spoil the ultra high vacuum which is needed for the creation of a BEC. Additionally, some of our measurements require an ion loss as a signal, therefore the trap needs to be frequently and quickly reloaded. So the aim was to develop an oven loading scheme that allows for fast temperature increase without putting to much heat in the surrounding materials and a subsequent fast cooling back to a normal temperature.

Resistive heating in a cable is proportional to the current squared and the resistance, $P_{heat} = R\,I^2$. The local temperature increase due to this heating is given by $\Delta T/\Delta t = P_{heat}/(c_p\,m)$, where c_p is the specific heat capacity of the material and m its mass. Calculated for the copper wire with 1 mm diameter this gives a temperature increase of $0.008\,\mathrm{K\,A^{-2}\,s^{-1}}$, whereas in the stainless steel tube there is a temperature increase of $0.5\,\mathrm{K\,A^{-2}\,s^{-1}}$. The temperature increase of the bulk copper is very small compared to these values and therefore

negligible. With these values one gets for a 100 ms short current pulse of 100 A a temperature increase of 500 K in the oven, and a temperature increase of 8 K in the copper wire. Considering now the heat conduction that has been neglected so far one finds that in the short time of 100 ms only less than 10 percent of the heat deposited in the oven can flow out to the surrounding materials. This fraction gets larger of course if one goes to lower currents and longer heating times, all the surrounding materials would heat up more and the total of energy that has to be put into the system to reach the same oven temperature would increase. In the case of the 100 ms short pulse the total energy put into the system is on the order of only 10 J.

This heating scheme with the short high current pulse has been previously tested on a sample oven with similar dimensions. The outcome of the tests confirmed the calculations: The stainless steel tube could easily be heated up such that one could see it glowing by eye while the temperature of the surrounding material did not heat up significantly and the copper wire's temperature increased only by some degrees, as predicted by the calculation.

1.3.5 Characterization of Neutral Yb Fluorescence

As Yb quickly oxidizes when exposed to air, the two ovens integrated in the ion trap have only been tested after being placed in the vacuum. It is still possible to see the oven glowing through one of the viewports. This visual check has mostly been used to confirm the oven is working when ions could not be loaded. The first oven has now been working reliably for the last three years and the second one has not yet been used.

The short current pulse of typically 94 A is provided by the same power supply used to drive the magnetic coils for the MOT. A fuse connected in series, consisting of three thin wires, has been designed such that the fuse burns before the oven does, and has been tested on the sample oven. To prevent any small currents from flowing through the Yb oven when not required, we placed two MOSFETs between both the oven supply and ground connection, and the power supply. These MOSFETs are opened by the control system of the BEC for accurate timing (cf. section 2.2) with respect to the current control of the power supply. Additionally, a digital output from the ion control system gates the first control signal. This allows the ion software (section 2.3) to enable or disable the firing of the oven, once in every cycle of the BEC.

The vapour pressure of Yb is given by [84]

$$p_{Yb}(T) = 1\,\mathrm{Pa}\,\exp\left(32.5 - 18680\,T^{-1} - 1.0849\log(T)\right)\ , \tag{1.18}$$

with the temperature T in units of Kelvin. The pressure increases quite rapidly with temperature. In the range of interest the increase is on the order of a factor 2 in pressure per 2% of current increase. Finding the right amount of oven current is therefore critical to achieve reasonable ion loading rates.

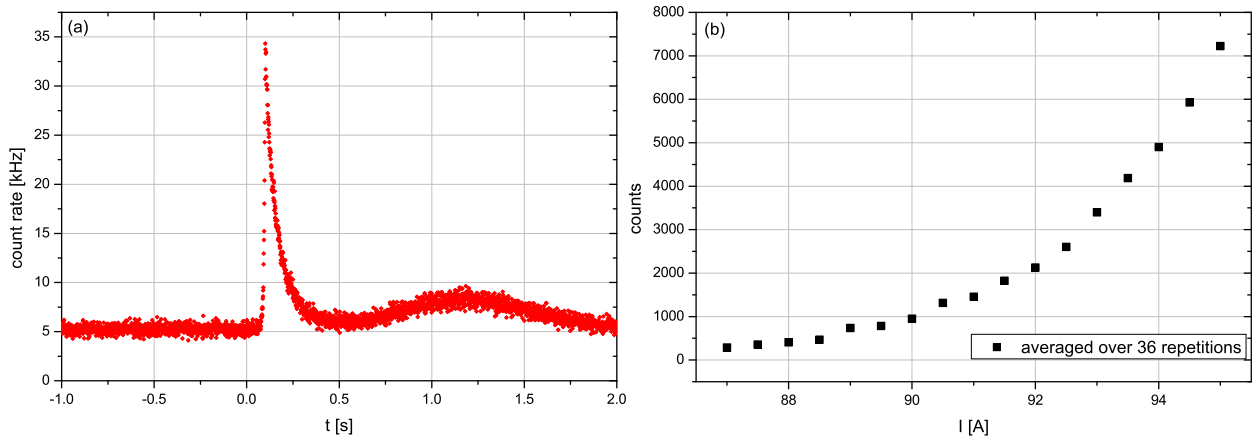

Figure 1.12: (a) The neutral ^{174}Yb fluorescence signal is recorded with a PMT and averaged over 36 realizations. The fluorescence is binned with 1 ms resolution over 3 s. At $t = 0$ the current ($I = 94$ A) pulse of 100 ms length starts, during which the oven heats up by several 100 K. After the 100 ms the oven's temperature is at its maximum and the fluorescence peaks. (b) The integrated neutral ^{174}Yb fluorescence counts are shown against oven current. The observed increase in fluorescence for higher currents slightly exceeds the expectation from the calculated vapour pressure.

The observation of fluorescence light of the neutral Yb marks the presence of Yb atoms in the trapping region and can be used to determine the required oven current. For this measurement, the frequency stabilized laser at 398 nm is focused to the centre of the ion trap and the fluorescence light is detected with a photo-multiplier-tube (PMT). The time resolved fluorescence rate is shown in Fig. 1.12a and the integrated fluorescence counts for different oven currents in Fig. 1.12b. The detection efficiency of scattered photons is on the order of 0.001, which means at 94 A there are about $5 \cdot 10^6$ photons scattered. Each atom is expected to scatter about 4 photons while traversing the laser beam. The number of atoms passing close enough to the ion trap centre, such that they can be trapped when ionized, is estimated on the order of 10^5. For this, an effective trapping radius of 25 μm has been assumed.

The data of Fig. 1.12b are expected to reflect the shape of Eqn. (1.18). The measured increase in fluorescence counts is however slightly higher than the calculated increase in pressure. This might be on one side due to Eqn. (1.18) being strictly applicable only to a steady state situation while we look at a dynamic system. On the other side, it is possible that the electric resistance of the oven increases with the temperature. For this second effect to be relevant the temperature of the stainless steel needs to be well above 1000 K, at least locally. This could be the case at contact points or where the material has been weakened, for example by the crimping or bending.

The shape of Fig. 1.12a behaves as anticipated up to $t = 0.5$ s. Within the 100 ms of heating, a linear increase in temperature together with Eqn. (1.18) fits the data. From $t = 0.1$ s to $t = 0.5$ s, a model with exponential temperature decay yields a characteristic, initial cool

down time of 0.95 s, consistent with the calculated 10% heat loss during 100 ms. The second observed increase in fluorescence rate thenafter is however difficult to explain. It is most probably due to a hot spot forming somewhere at the back of the oven during the 100 ms of heating. Thereafter the heat flows from there towards the Yb within the next 1 s, causing the second peak in fluorescence.

During the pulsed oven operation typically no effect is observed on the vacuum. A small temperature increase of 0.5 K can be seen on the sensor placed next to the oven. A temperature recording will be shown in Fig. 2.15. The pressure gauges can register an increase in the vacuum background pressure only when firing the oven for the first time, or after it has not been used for an extended period, when dirt has deposited on the oven. In normal operation, when the oven is fired several times per hour, this pressure increase is not seen. Even the size of the BEC is not affected when the oven is fired just 4 s before condensation. In the standard experimental cycle, the oven fires about 50 s before Bose-Einstein condensation.

1.4 Laser Setup

1.4.1 Rb Lasers

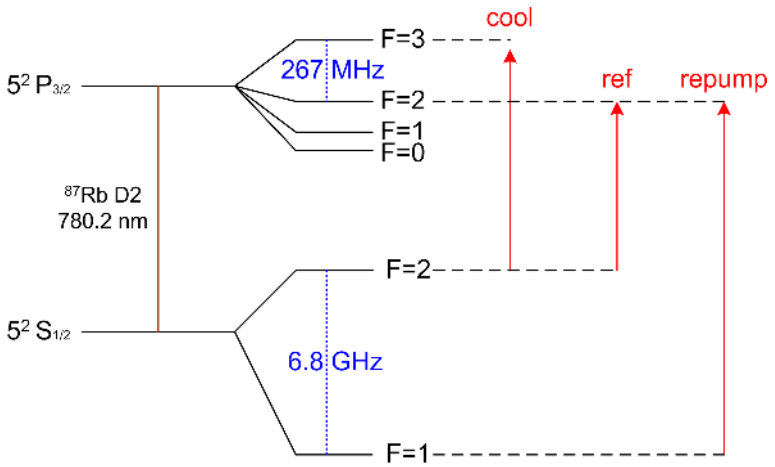

Figure 1.13: The ^{87}Rb D2 line hyperfine level scheme is shown with the relevant splittings. Accurate numbers can be found in [85]. The red lines on the right side indicate the laser frequencies of the three lasers used in our setup.

In the experiments with the ^{87}Rb condensate we use lasers to cool, manipulate, trap and image the atoms. Three home-built diode lasers, with an external grating for frequency stabilization, are used to drive atomic transitions on the D2 line, indicated in Fig. 1.13. The transition from $F = 2$ to $F = 3$ is used in the Doppler cooling during the MOT and for the absorption imaging (cf. later chapter 3.6). Our MOT operates with large beam diameters and therefore requires more laser power than the diode delivers directly. To this end, the output

from the diode laser is amplified by a tapered amplifier, resulting in about 300 mW of optical power in the MOT. The frequency of the MOT laser is controlled with an offset lock [86]. As a reference, we use another diode which is locked to the $F = 2$ to $F = 2$ transition by Doppler free RF-spectroscopy [87] on a Rb vapor cell. Part of the light of this reference laser is used for the absorption imaging, for which the optical frequency is increased by 267 MHz with an acousto-optical modulator (AOM). The AOM serves two purposes. It controls the exact frequency of the imaging light and allows for fast intensity switching. The third diode laser is locked to the $F = 1$ to $F = 2$ transition by means of another RF-spectroscopy on a Rb vapor cell. The light is used for repumping atomic population from the otherwise dark $F = 1$ ground state back to the D2 cycling transition between $F = 2$ and $F = 3$. The repumping light is enabled during the MOT, and optionally during the imaging. A schematic of the laser setup is shown in Fig. 1.15.

1.4.2 Yb Lasers

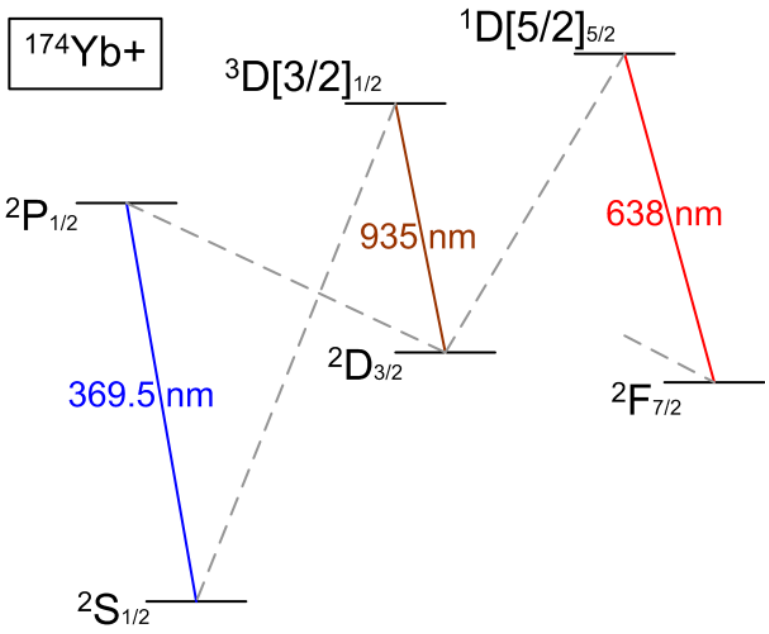

Figure 1.14: Level scheme of the ^{174}Yb ion. The main cooling transition $S_{1/2}$ to $P_{1/2}$ can be driven with a laser at 369.5 nm. Two long lived states, the $D_{3/2}$ and the $F_{7/2}$ can be repumped with light at 935 nm and 638 nm respectively. The level structure for the other isotopes of Yb without nuclear spin, such as ^{172}Yb or ^{176}Yb, looks identical and the transitions are shifted by a few 100 MHz [82].

The Yb ion is laser cooled on the $S_{1/2}$ to $P_{1/2}$ transition with a wavelength of 369.5 nm. A level scheme for the ^{174}Yb ion is shown in Fig. 1.14. One dark state, the $D_{3/2}$ requires a repump laser at 935 nm. A second dark state, the $F_{7/2}$ can be repumped with a laser at 638 nm. However, since this state very rarely gets occupied, we have not used the 638 nm laser

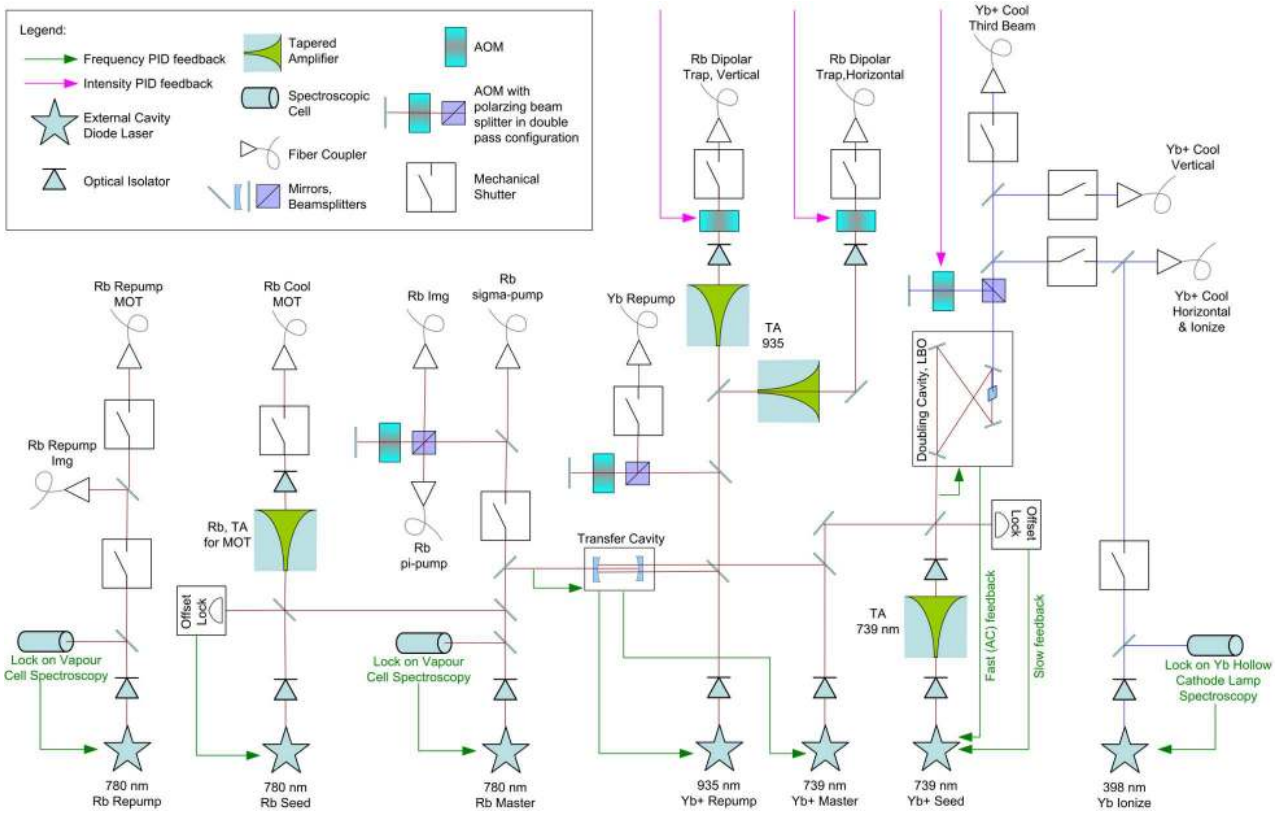

Figure 1.15: Schematic drawing of the laser setup with an emphasis on the control of frequency and intensity. The seven diode lasers are all PID-frequency stabilized, either by Doppler free RF-spectroscopy (Rb Repump, Rb Master, Yb Ionization), by offset-locking (Rb Seed, 739 Seed), or by a transfer lock on a cavity (Yb Repump, Yb Master). The transfer cavity is locked to the Rb Master. The frequency doubling cavity is locked to its seeding laser. Intensity controls are realized by PID-feedback from a photodiode placed after the fiber output. They are implemented for the dipolar trap and the ion cooling light. In the latter case, an electronic logic switches between three UV-photodiodes depending on the states of the three shutters for the Yb cooling light.

in any of our experiments. Additionally, for the two-photon ionization process, another laser at 398 nm is required to drive an S to P transition in the neutral Yb.

The laser system, which has been designed and built by Stefan Palzer, consists of five diode lasers, two cavities and one tapered laser. A schematic of the laser setup is shown in Fig. 1.15, and a more detailed documentation can be found in [73]. All lasers are frequency stabilized. The 398 nm laser is locked to a specific isotope neutral Yb resonance with RF-spectroscopy on a hollow-cathode lamp. All the other lasers for the Yb ion system, are locked to a transfer cavity which is itself locked to the Rb reference laser. The frequency lock is stable over long terms within a few MHz. Drifts are primarily caused by air pressure fluctuations in the cavity. Fine tuning of the repump laser frequencies is achieved by sending the beams through an AOM. The light at 369.5 nm is created by frequency doubling the light of a 739 nm tapered laser. The frequency doubling is achieved with an LBO crystal in a bow tie cavity.

For frequency control, the tapered laser is seeded by a diode laser at 739 nm. The frequency of this diode is offset locked to another diode laser, which is locked to the transfer cavity. The tuning range of the offset lock is 245 MHz, allowing to continuously scan the UV frequency over about 20 times the natural linewidth of the ion cooling transition. The exact frequency settings are calibrated by direct spectroscopy on the ion (cf. section 2.3.3).

1.4.3 Optical Access

Our experiment is set up on two different tables. The above described lasers shown in Fig. 1.15 are placed on the first table, while the BEC apparatus and the ion trap are on the second table. The laser light is transmitted through single mode fibers from the first to the second table. A small amount of the outcoupled UV and dipole trap light is sent to photo-diodes for intensity control. The light from most of the lasers is then sent to the atoms and ions, from various different angles. Fig. 1.16 shows all the laser beams which can be applied to the interaction region between the ion and the condensate. The ion repump light is sent along the ion trap symmetry axis. UV light, to drive the ion cooling transition, can be sent on three different axes, necessary for micromotion detection (cf. section 3.2). The light at 398 nm used in the two-photon ionization process is sent copropagating with on of the UV beams, as it conveniently is coupled into the same fiber. The ion fluorescence light is imaged onto a CCD-camera by an objective situated above the vacuum chamber. On one horizontal axis, another objective collects ion fluorescence photons to be counted with a photo-multiplier tube (PMT). Several apertures and an interference filter are employed to reduce the background count rate. Two different objectives have been used for photon collection in the experiments which will be described in chapter 4. The more recent one, designed by Lothar Ratschbacher [88], has a ten-fold better photon collection efficiency than the previous objective. The Rb atoms can be imaged on one horizontal axis and on the vertical axis. The crossed beam optical dipole trap consists of two beams, one along the vertical axis, the other counter propagating to the ion repump light on the horizontal axis. In those situations where different beams use the same axis of optical access and need to be separated, polarization dependent, spatial, or chromatic filtering is used.

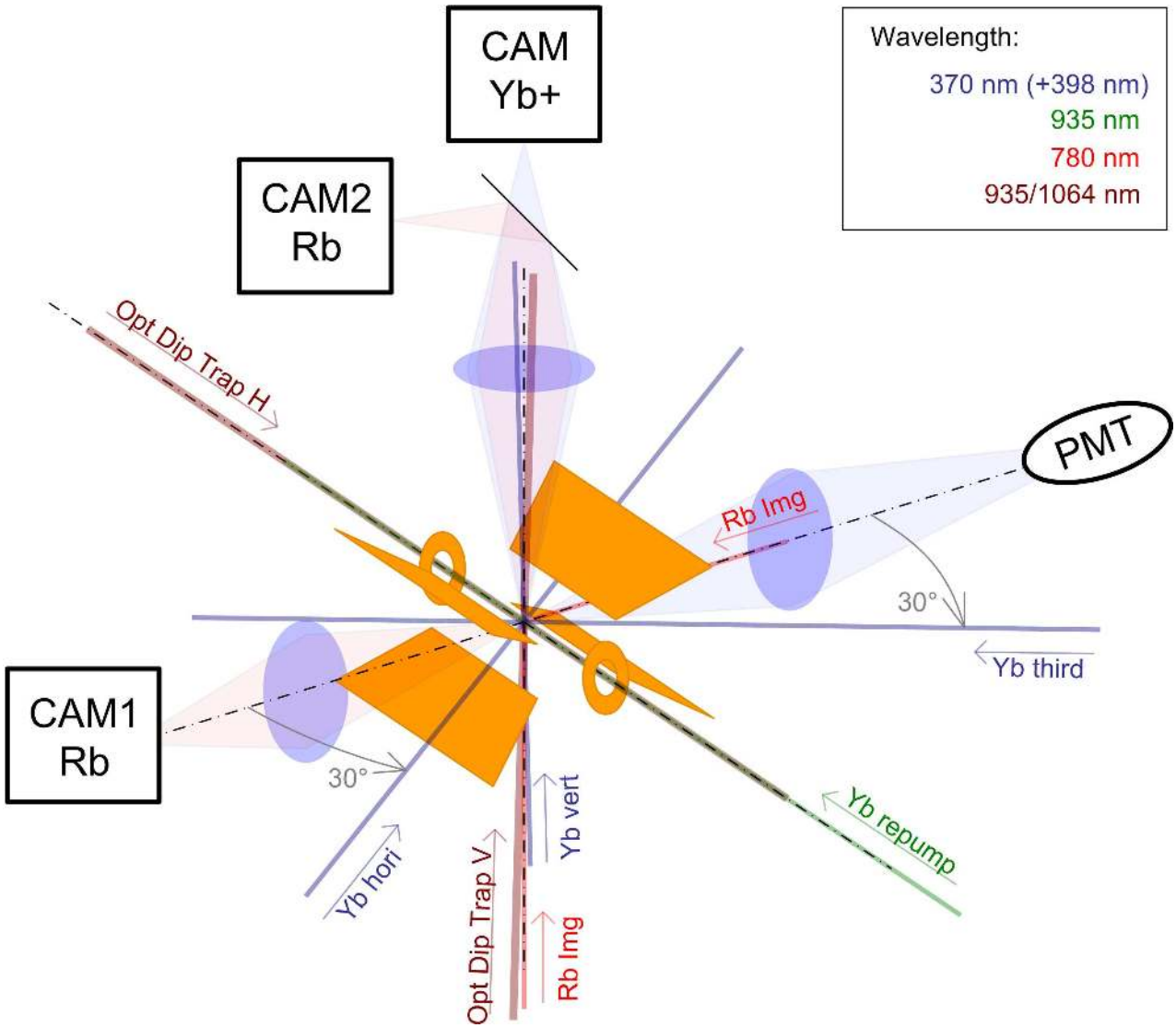

Figure 1.16: The drawing shows all the laser beams intersecting in the combined trap centre region. The ion trap electrodes are sketched in orange. Three beams, driving the main Yb^+ fluorescence line at 370 nm, are required to detect micromotion in all three dimensions. On one beam (Yb hori), light at 398 nm is additionally used in the two-photon ionization of the neutral Yb. The repump light for Yb^+ is sent from one side through the holes in the end-cap electrodes. The fluorescence light of the ion is collected by an objective and detected with a photomultiplier-tube (PMT), or imaged on a camera through a different objective at the top of the setup. The same objective is used to take an absorption image of the Rb cloud in the vertical direction on a different camera, after a 50/50 beamsplitter. The Rb atoms can be illuminated with 780 nm imaging light from either the bottom, or through the objective used in conjunction with the PMT to image the neutral atoms along the horizontal direction. For this, another objective and a camera (CAM1 Rb) are set on that horizontal axis. The crossed-beam optical dipole trap uses two laser beams, one on the horizontal axis through the holes in the end-cap electrodes, and the second one pointing upwards along the vertical direction.

Chapter 2

Electronics and Software

This chapter describes the control of our experiment. We are using two different software controlling systems and a variety of home-built and commercial electronic devices. Clock synchronization for these devices will be explained, which is essential for example for our scheme of micromotion compensation. The two software systems, one of which has been developed in the course of this work, will be introduced, including a few methods of data evaluation. The electronics to drive the ion trap RF-voltage and a few more essential electronics will be characterized.

2.1 Timing and Synchronization

In an experiment with many devices involved, synchronization between them is essential. The use of a single master clock greatly facilitates this task. In our system we use a Rubidium atomic clock source with an output at 10 MHz of the type *Efratom LPRO*. With the help of two distribution amplifiers of the type *MAX4135* the 10 MHz signal is split into 12 identical signals. They are then used by various devices such as synthesizers, spectrum analyzers or buffered digital to analog converters. Another device, which we use to measure time difference with a high resolution of 25 ps, is the *RoentDek TDC8HP* time-to-digital converter (TDC). It is mainly used to measure photon arrival times of the fluorescence light from the ion. The TDC requires an external clock at 39.0625 MHz. To provide this frequency, a clock generator board has been designed (see Fig. 2.2) which phase locks a voltage controlled oscillator (VCO) to the 10 MHz signal. The phase locked loop (PLL) is

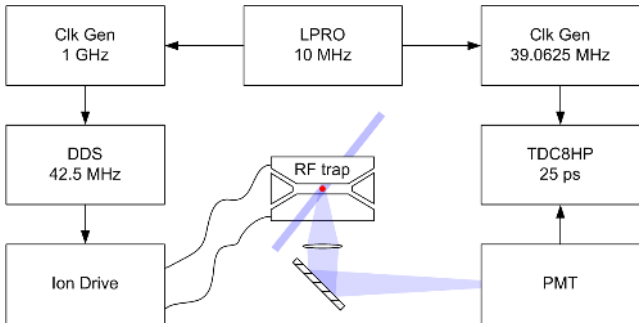

Figure 2.1: Schematic of clock distribution to synchronize the measured photon arrival times with the ion trapping RF field.

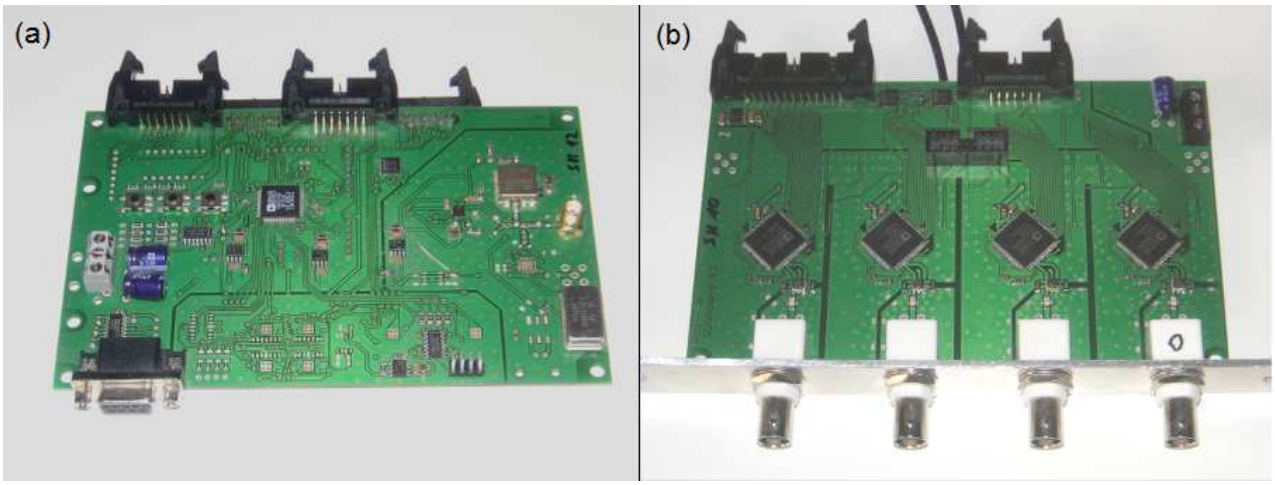

Figure 2.2: (a) Clock Generation Board (b) DDS Board

controlled by a *ADF4154*. This device must be configured over a serial peripheral interface (SPI). For this purpose, a microcontroller (*ADuC7026*) is used, which can be connected via RS-232 to a computer. The frequency of the PLL is set once upon power up of the system. The same microcontroller is however used for many other applications as well, making use of the serial data-interface to the computer (cf. 2.5). The PLL on the clock generation board is ideal to generate a fixed frequency output. A better tunable system is achieved by the use of direct-digital-synthesis (DDS). We are using devices of the type *AD9858*. They require an external clock at 1 GHz provided by a clock generation board as described above. The typical frequency output ranges from a few kHz up to 400 MHz with a resolution of 0.23 Hz. The frequencies can be set over an SPI or a parallel interface. The microcontroller of the clock generation board is used to control the DDS over SPI. The parallel interface can be accessed with an FPGA, allowing frequencies to be changed with higher timing accuracy. The DDS outputs are used for a wide range of applications, such as RF-evaporation on the Rubidium gas, as frequency source to drive AOMs or offset locks, and as RF source for the ion trap.

2.2 Computer Control of the BEC setup

The successful and reproducible creation of a BEC depends a lot on accurate timing of all the magnetic and light fields. Magnetic fields are driven by power supplies where the electric current is controlled by an analog signal. Fast switching of the fields is achieved by using MOSFETs which are controlled by TTL signals. Laser fields are frequency and intensity controlled by analog signals and switched with TTL signals. For instance, the length of light pulses used in absorption imaging need to be controlled to better than 1 μs in order not to limit the measurement accuracy. Thus the basic requirement to control a BEC cycle are some accurately timed analog and digital outputs.

In our setup we use one *Viewpoint Systems DIO-64* providing 64 channels of digital output and two *National Instruments PCI-6733* providing 8 analog outputs each. All three cards are placed in the same computer and clocked with the 10 MHz atomic clock signal. Both the *DIO-64* and the *PCI-6733* have a local buffer which works in a load and execute scheme. In a preparation step the required ramps and timing edges are loaded into the buffers, and upon a synchronized start trigger all the cards run trough the whole buffer. At the end, the buffers get ready to be loaded again and the cycle can restart. The advantage of this type of setup is that all outputs stay synchronized throughout the cycle without the need of additional triggering.

The software *Experiment Wizard* which we are using to set up and control the BEC cycle has been developed by Thilo Stöferle for experiments with ultracold gases at ETH Zurich [89]. The software uses a graphical user interface to map the buffer contents onto a time based matrix, providing an intuitive visualisation of the BEC cycle. Variables can be used to define specific features of the experimental sequence, like for example the time of flight before an absorption image of the falling atoms is taken. Changing one such variable for every consecutive cycle generates a series of measurements. A separate part of the *Experiment Wizard* software, the *Camera Control*, handles data acquisition from several CCD cameras and performs fits to the data using physical models. Fit results and experimental parameters are then written into comma-separated-value (csv) files, which can later be used for data analysis with any standard spreadsheet software.

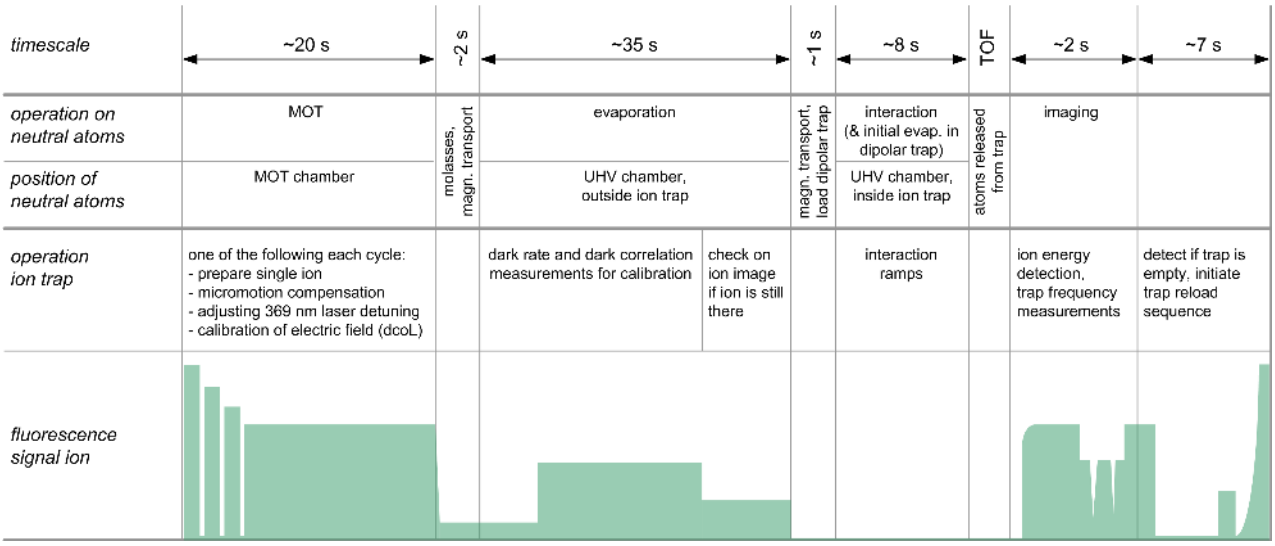

Figure 2.3: Diagram of a typical experimental cycle, showing the basic stages. The operations which include the ion trap will be described in chapter 3. Synchronization between the neutral atom preparation and the ion trap system is handled by the DECADS software.

A diagram of our experimental cycle is shown in Fig. 2.3. Most of the operations on the neutral atoms are controlled by the *Experiment Wizard* (except for some hardware, like the DDS used for the evaporation, which is not controlled by this software). The operation of the ion trap is controlled by a different software, which will be introduced in the following section.

2.3 Distributed Experiment Control and Data-Taking System (DECADS)

During the design phase of the ion trap and the attached control electronics we realized that a different type of control system is required for an ion trap experiment than for a BEC experiment. The ion can stay trapped for long times, but loss processes are often random. This makes it difficult to define a fixed cycle length. Also, upon detection of an ion loss a new ion loading sequence should be initiated, requiring some means of feedback within the software. These two points both oppose the buffer load and execute scheme. As the *Experiment Wizard* builds upon this technique, it was decided to develop a new experiment control software as a part of this thesis.

The new software design is shaped by three main targets. The first one addresses both the need for user interference with the running system and allows for software feedback loops. It is the requirement to design interfaces between hardware and software, which can be continuously accessed, specifically while the hardware is running. Even though not every type of hardware supports this mode of operation, the software is designed to support such continuous access as far as possible. Within the software, parallel code execution, which is required to control several hardware systems at the same time, is supported by multi-threading. The second target is to support the idea of connecting all hardware in the laboratory to one controlling system. The idea holds many promises, such as quick setup and easy reproducibility of experimental configurations, central data logging, simplified development of feedback loops, etc. The usual problem with complex control systems is, that integration of a new hardware becomes more difficult, the larger the control system has grown. Here this increase of complexity is prevented with modular hardware integration. It allows the development or maintenance work on single hardware parts without the need of shutting down and restarting the main software system, or worse, even recompiling the whole software. Code templates with extensive documentation have been prepared to simplify the task of integrating additional hardware. The third target is to keep detailed track of all what the system is doing. Traceability of all actions relevant to the experiment, performed via user interfaces or from automated routines, is essential to reconstruct past experiments or just to understand recorded data. As a consequence, several logging mechanisms are implemented in the software and enabled by default.

For the user, the software system consists of one main application, currently named *DECADS Console V2*, and the additional modules to interface with specific hardware, called HWDM. The main application and each HWDM can be installed independently. HWDMs run on the computer with the physical interface to the hardware (e.g. serial port, USB, PCI-card, ...) and get connected to the main application via a local network, using TCP-IP.

The software has been written in C++ with *Microsoft Visual Studio*, using MFC, and runs under Windows XP, Vista and 7. In the following, the main application and a few experiment specific hardware modules (HWDM) will be explained. A schematic overview of the software

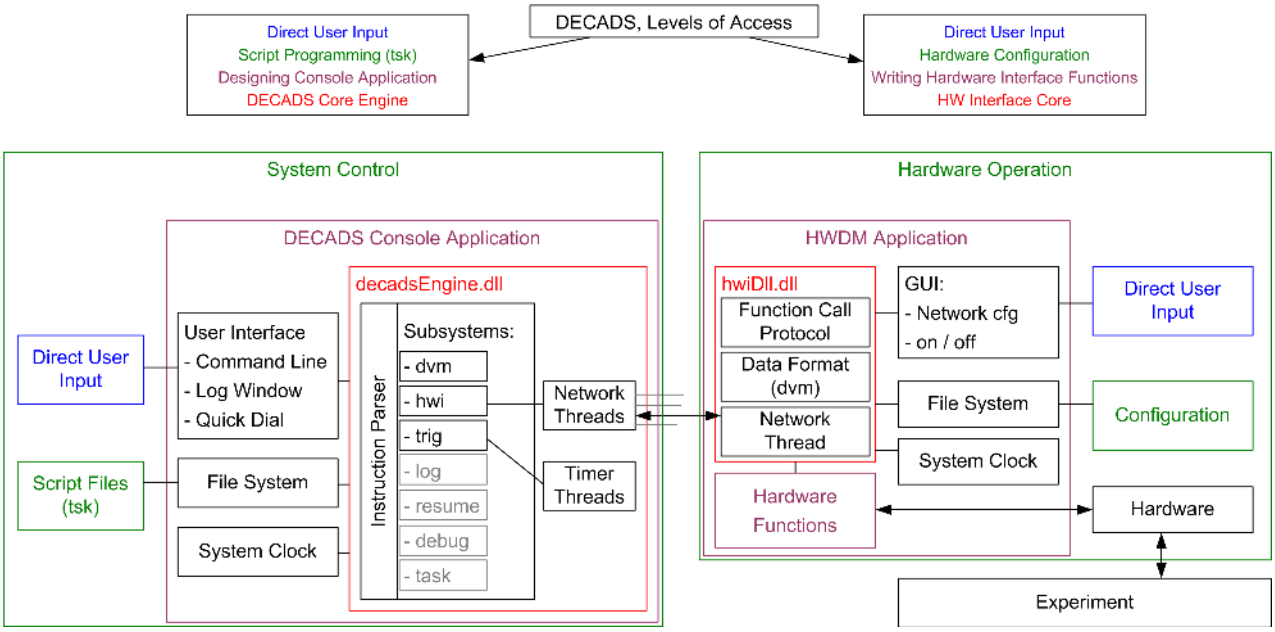

Figure 2.4: Schematic of the DECADS software concept. Hardware Modules (HWDM) are connected via Ethernet to the main control application (Console). Each HWDM can be taken offline without disturbing the rest of the system, which facilitates maintenance work and the process of adding new hardware. User access is structured in four levels. The top two levels (blue and green) correspond to the daily operation of the experimental setup. The two bottom levels (red), which require programming in C++, consist of the core level (the DLLs) and the interface level which, for the HWDM, provides a set of functions that connect the hardware with the DLLs and the user interface.

structure is shown in Fig. 2.4.

2.3.1 Console

The user interface of the main application works in a similar manner as a console application. There are command lines where the user enters text commands and a log window where the system displays recent commands and messages from the engine. Commands are sent to the main engine thread and get interpreted by a parser. The engine consists of several subsystems. One first subsystem, the data value management (dvm), is intended to store any parameters or measurement results relevant to the experiment. Values are stored with their standard error, a physical unit and are accessible by a name. A number of mathematical operations have been implemented in the dvm-subsystem, from simple additions or multiplications to multi-parameter fitting routines. With a Monte-Carlo error calculation technique, the dvm-subsystem functions as a numerical calculator, dealing with both physical units and error propagation. Another subsystem is responsible for data logging and saving these data in a readable form, such as a csv-file. The hardware interface subsystem (hwi) is used to connect the engine to the hardware modules (HWDM) over TCP-IP, and gives access to the full

hardware functionality made available by the HWDM. A software triggering system (trig) adds the necessary methods to implement automation. A list of commands can be set which get executed on a trigger call. These are triggered either by a timer, an incoming network call from the hwi subsystem, a value being updated in the dvm subsystem or after a successful comparison of two values. Multiple commands can be bunch-executed by using a batch-file. Automatic system reconfiguration after a software restart is supported by an autostart batch-file call and a resume function to retrieve parameters such as electric field compensation values.

In our experiment the software runs very stable, typically for more than a month without a restart. Its versatile structure has made it useful also to the other experiments in our research group. In the fermionic experiment for instance, the software is mostly used because new hardware can easily be integrated into the existing measurement cycle.

2.3.2 Camera iXon

To image a single or few ions we use a CCD camera of the type *Andor iXon DV-885*. The hardware interface module directly maps a couple of functions from the *Andor* application programming interface (API), such as setting the exposure time, the camera temperature or the electron multiplier (EM) gain. Acquired images are displayed and saved locally, including information on exposure time, CCD temperature and EM-gain.

The information of primary interest in an image of an ion crystal is the number of ions and their positions. A fitting function to retrieve these data is implemented in the HWDM, which will be described in the following.

The problem of finding the positions of ions on a CCD-image is analogous to the search for local maxima in a 2D array. Electronic noise, stray-light and photon shot-noise typically limit the quality of a single image and demand for a position search algorithm with little sensitivity to this noise. Some averaging technique over several pixels is required.

One very simple method, analogous to the calculation of the center of mass for a given density distribution, is to calculate the center of light. Doing this for a full image will approximate an ion's position if it is only one, but give some average between ion positions if there are more than one ion. Instead, calculating the center of light only in a small region, that encloses only one ion, will give the center position of this ion.

As this suggested method requires the prior knowledge of the approximate position to locally average around, it will be recursive. Starting from a random position, in every iteration step the position will seek its way towards the nearest local maximum. The new position is determined with the weighted average

$$\vec{s}_{i+1} = \frac{\sum_j \vec{r}_j v_j \exp\left(\frac{-(\vec{r}_j - \vec{s}_i)^2}{2\,w^2}\right)}{\sum_j v_j \exp\left(\frac{-(\vec{r}_j - \vec{s}_i)^2}{2\,w^2}\right)}\,, \tag{2.1}$$

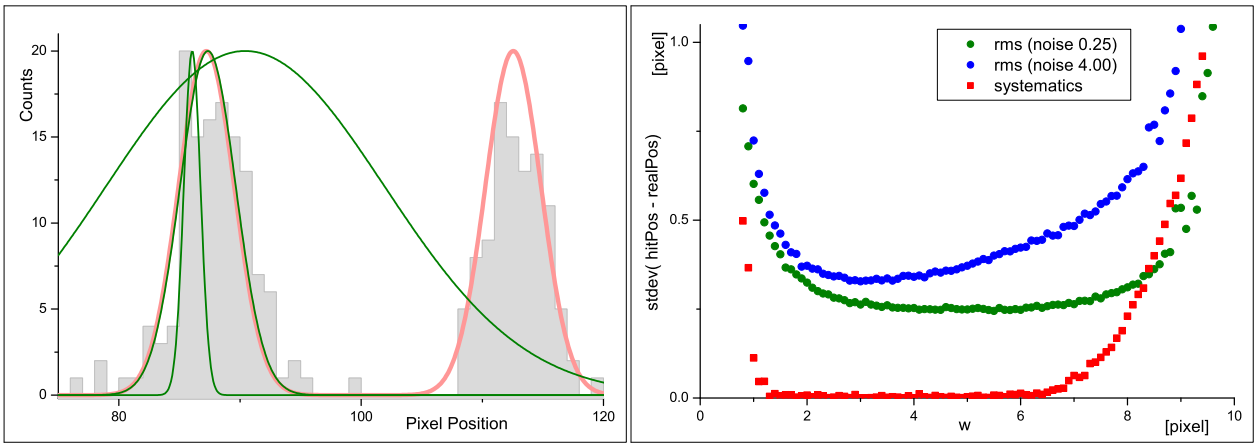

Figure 2.5: (a) A one-dimensional randomly generated Poissonian sample (grey), according to a preset distribution (red), is used to test the algorithm with 3 different w. The converged envelopes (green) are shown. For very small w single pixel noise deteriorates the fit and for very large w the neighbouring peak affects the fitted position. Fitting with w comparable to the real width of the signal gives the best result. (b) Expected errors on the fitted position are shown in dependence of the choice of w. The data is obtained by repeating the test shown in (a) 5000 times. The width of the preset distribution is 2.3. Systematic errors (red) occur for large w when the seeker's envelope overlaps with more than one signal and for small w due to single pixel noise. The RMS of the error is plotted for two different settings of background noise, in green, for a background noise level of 0.25 as in (a), and in blue for a background noise level of 4.0. The optimal w is typically found somewhat larger than the real signal width, depending on the background noise.

using the Gaussian width w to define the small region in which to calculate the center of light. Here $\vec{r}_j$ denotes the position of pixel j and v_j its value. The sum can be taken over all pixels j of the image. It is however sufficient to sum on pixels within a range of $4\,w$ around $\vec{s}_i$, due to the fast decay of the Gaussian profile. A convergence criterion of the form $|\vec{s}_{i+1} - \vec{s}_i| < \epsilon$ is used to stop iterating once the local maximum is found with sufficient accuracy. For $\epsilon = 10^{-5}\,w$ a seeker's position $\vec{s}_i$ typically converges after only 20 iterations.

The parameter w is chosen similarly as the waist of a typical image of an ion or slightly larger. Using a w smaller makes the determination of the ion position sensitive to fluctuations within the center of the ion image peak. w smaller than the size of a pixel should be avoided as single pixel noise will otherwise dominate the algorithm's behaviour. Choosing w larger than the size of the signal increases the influence of background noise. And if the seeker's Gaussian envelope starts overlapping with a second ion, systematic errors on the fitted position are expected, or worse, the two signals become indistinguishable, see Fig. 2.5.

To find all the local maxima within a defined region of interest, a grid of initial seeker positions is set up. A reasonable choice for the grid spacing is $2\,w$, as local maxima closer together than this will not be distinguished anyway.

Once all the seekers have converged a selection is made to identify the ones corresponding

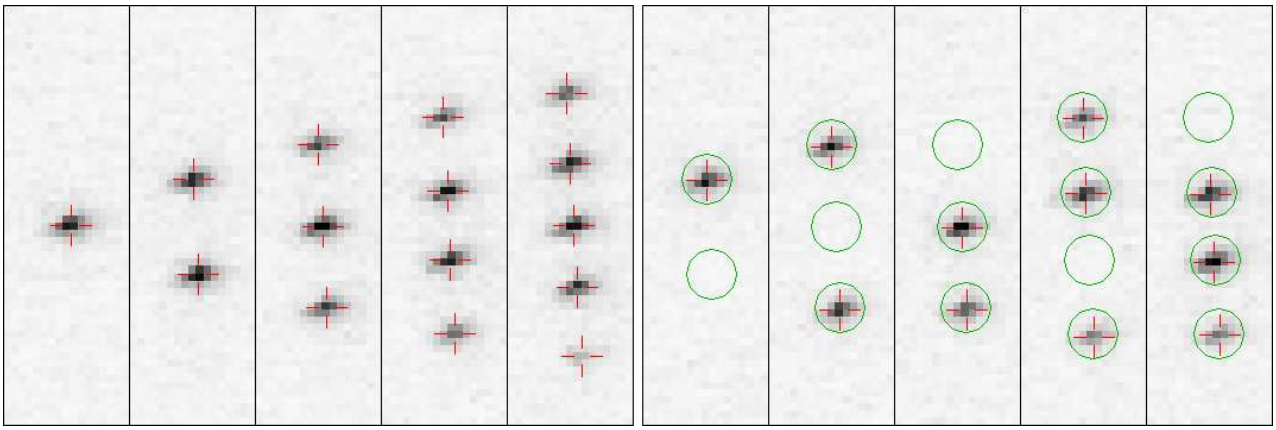

Figure 2.6: Ion fluorescence signals on CCD-images taken directly after loading the ion trap (left) for 1 to 5 ions. The red crosses mark the detected hits. Matching memorized patterns to the found hits (right) identifies dark ions, as they are occupying a non-fluorescing site in the Coulomb-crystal. The green circles indicate the pattern which the software automatically determines as the best fit to the data.

to real ion signatures. First, the seekers having converged to the same point are treated as one, using a minimum spacing requirement in units of w. Next, the weight of each signal is calculated.

$$W = \frac{\sum_j v_j \exp\left(\frac{-(\vec{r}_j - \vec{s}_i)^2}{2\,w^2}\right)}{\sum_j \exp\left(\frac{-(\vec{r}_j - \vec{s}_i)^2}{2\,w^2}\right)} \tag{2.2}$$

The seeker is identified as a hit if the weight W exceeds a multiple of the image's background noise. Then the highest weight W_{max} is searched for and all hits with a weight W less than a predefined fraction of W_{max} are discarded. The identified hits are then usually sorted along the trap axis for ease of data access. Typical experimental data with the detected ion signals are shown in Fig. 2.6.

The presented algorithm is accurate to the limit given by image noise. It works reliably and fits well even under changing conditions of noise or signal size. It is very fast compared to alternative multi-parameter fit routines and allows recognition of the number of ions to be efficiently used within feedback loops, to control the number of ions in the trap.

An additional feature is implemented to detect the presence of dark ions. Having at least one bright ion left in the trap, it is displaced by its Coulomb interaction with the dark ions. The algorithm remembers positional patterns of Coulomb crystals of up to 5 ions. After detection of the ion positions, these are matched to the memorized patterns by minimizing the positional displacement.

Learning the patterns could be done once initially, but to account for slow positional drifts the learning process is implemented as a floating average with exponential weighting. Only images with no dark ions should be used to set up the patterns. Therefore the pattern learning process is applied to the first image taken directly after loading the previously emptied ion trap.

Additionally a rejection mechanism is implemented to only accept images where positional displacements are within some predefined limit.

To identify the pattern which best fits some found ion positions, the RMS of position mismatches for all possible mappings are calculated, and the mapping with the smallest RMS is selected. Images from experiments with dark ions present are shown in Fig. 2.6, with the matched patterns indicated by green circles.

From the repeated learning process, the expected RMS value is known and can be compared to the RMS of the fit. Assuming normally distributed positional mismatches, the probability for a correct pattern recognition is calculated and logged for later usage in data analysis. This probability is typically close to 1, except when there is only a single bright ion in the centre. The patterns for 1, 3 and 5 ions are then equally good fits, one is mapped randomly due to the present noise and the resulting probability is on the order of 0.4.

2.3.3 TDC8HP

The HWDM module for the time-to-digital converter (TDC) *RoentDek TDC8HP* handles the photon arrival times, which are detected with the photomultiplier tube (PMT) *Hamamatsu H7360-01*. The TDC has eight input channels with a resolution of 25 ps. One channel receives the signal from the PMT. Two other channels are used for triggering. The TDC runs in a continuous mode, typically for several months. The raw data stream from the TDC8HP card is stored on a local hard disk, to ensure full traceability of any data evaluation based upon these raw data. The storage amounts to several GB per day, making frequent data transfers to a server necessary. A first step in the data analysis is to filter out double counted events. The PMT provides a pulse-pair resolution of 18 ns. Therefore, the software is set to discard any event which has a separation smaller than 18 ns to its predecessor. The counted photons are continuously binned, typically in 100 ms wide bins, and the histogram is saved in csv files and displayed on a screen. This immediate display of the photon count rate is the fastest channel of information from the ion trap to the experimenter and is often used for example for alignment of laser beams to the ion. Different binnings can be requested through the software interface, externally triggered if required.

One important function, which is mostly used for micromotion compensation, is the calculation of correlation between photon arrival times and a certain frequency ω. The function evaluates all n photon arrival times t_j within a requested time interval of length Δt. The frequency ω is resolved with a bandwidth of $1/\Delta t$, implying that, to resolve a correlation the frequency must be known with a precision better than the bandwidth. The function returns the correlation information by means of two coefficients. To calculate these, we first define the photon signal function

$$f(t) = \frac{1}{n} \sum_{j=1}^{n} \delta(t - t_j) \; . \tag{2.3}$$

The Fourier transform at the frequency of interest

$$\hat{f}(\omega) = \int_{-\infty}^{\infty} f(t)\exp(-i\omega t)\mathrm{d}t = \frac{1}{n}\sum_{j=1}^{n}\exp(-i\omega t_j) \tag{2.4}$$

is then simply separated into its real and imaginary part, which define the correlation coefficients

$$c_c(\omega) = \frac{1}{n}\sum_{j=1}^{n}\cos(\omega t_j) = \mathrm{Re}(\hat{f}(\omega)) \tag{2.5a}$$

$$c_s(\omega) = \frac{1}{n}\sum_{j=1}^{n}\sin(\omega t_j) = -\mathrm{Im}(\hat{f}(\omega))\ . \tag{2.5b}$$

The expected error on these coefficients is determined by photon shot noise, which is $1/\sqrt{n}$ on $|\hat{f}(\omega)|$, or $1/\sqrt{2n}$ on $c_c(\omega)$ and $c_s(\omega)$. The definition of the correlation coefficients is related to the modulation index, which is the amplitude of the count rate modulation divided by the average count rate, which corresponds to $|2\hat{f}(\omega)|$.

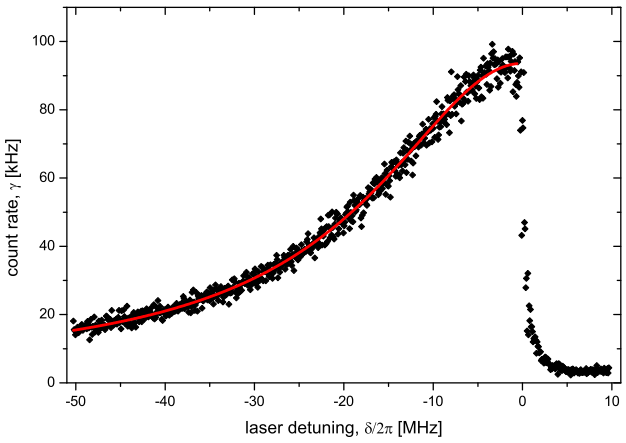

Figure 2.7: Ion fluorescence (black) binned in 10 ms wide bins while the excitation frequency is scanned over 60 MHz within 8 s. The red line represents the single-sided Lorentzian fit with parameters $I/I_{sat} = 2.9$ and a counting efficiency of $\epsilon_{PMT} = 0.00193$.

A further function, implemented into the HWDM module for the TDC8HP, is to fit a Lorentzian profile to the photon count rate. The motivation is to automatically adjust the laser frequency to a given distance from the resonance frequency of the ion. Though all the lasers are frequency locked in our system, some drifts of several MHz can still be observed, mainly related to air pressure changes in the transfer cavity. To compensate for these drifts, the function described here is used to evaluate direct spectroscopy on the single ion. The acquisition procedure is the following. First a trigger signal is sent to the TDC and the laser frequency is slowly swept from red detuned to blue detuned. After completion of the sweep, the photon counter data from the time of the sweep is binned and each bin labeled with the detuning frequency δ. A dataset of this type is shown in Fig. 2.7. The Lorentzian shape is single-sided because when the laser is blue detuned, the ion heats up

and fluorescence decreases. On the red detuned side the photon count rate is expected to be

$$\gamma(\delta) = \frac{\epsilon_{PMT} \cdot \Gamma/2 \cdot I/I_{sat}}{1 + (2\delta/\Gamma)^2 + I/I_{sat}} \quad . \tag{2.6}$$

The fitting procedure first estimates the position of the resonance by searching for the steep drop of fluorescence, then adapts the counting efficiency ϵ_{PMT} and the laser intensity I/I_{sat}. Next, the three parameters are adjusted to minimize the sum of squared errors within the red detuned side. A fit of this type is also displayed in Fig. 2.7. As the variance of the recorded count rate is known from the expected shot noise, the reduced chi-square is easily calculated and returned with the other fitting results to the main application. Before adjusting the laser detuning for following measurements to the newly determined resonance, the reduced chi-square value is used to check if the measurement was successful and accurate. The fit results of ϵ_{PMT} are useful to check and monitor the alignment of the photon counting system, and the saturation parameter I/I_{sat} is important to understand the micromotion correlation (see section 3.2) and for measuring the temperature of the ion (see section 3.4). The model of Eqn. (2.6) assumes a pure two-level system and neglects any additional broadening, such as from non degenerate Zeeman levels in the presence of a magnetic field [90]. This additional effect is estimated to be very low in our measurements, as they are usually performed during the MOT loading phase while the magnetic field at the position of the ion is below 1 G.

This measurement relies however on a successful compensation of micromotion (see chapter 3.2), as large micromotion amplitudes introduce sidebands on the spectroscopic signal.

2.4 Ion Trap (Drive) Electronics

In this section, the electrical circuit which generates the electric trapping voltage of the form $V_0 \sin(\Omega_T t)$ will be explained.

2.4.1 Circuit Design

One of the main challenges in designing ion trap electronics is the effective generation of the high voltage radio frequency (RF) signal and its delivery to the trap electrodes. Some general conclusions on the type of electrical circuit required, can be made due to very basic constraints. The power dissipation in the vacuum has to be kept low to avoid excessive heating, so all ohmic resistances have to be minimized. At the same time the impedance of the trap has to be high in order to achieve high voltages without using immensely high currents. For a standard 50 Ω impedance as an example, with 250 V of voltage amplitude the needed RF-power would be 1 kW. In the case of our ion trap the impedance is mainly given by a capacitance defined by the geometry of the electrodes and the dielectric properties of the used materials. For typical RF frequencies this impedance is on the order of 1 kΩ, which still necessitates a power of 50 W

to achieve the high voltage. A resonant circuit further reduces the required RF power, making it possible to operate the ion trap with decent RF amplifiers.

For our setup the resonating circuit had to be designed such that the resonance frequency Ω_T fits within some given limits. The RF evaporation ramp for the evaporative cooling of the neutral atoms runs from around 25 MHz down to less than 1 MHz. The ion trap's driving frequency Ω_T has to be outside this range, otherwise producing a BEC will become impossible as atoms would be lost from the magnetic trap before they can be cooled. Having the resonance well below 1 MHz was not an option as it would limit the trapping frequency ω_r of the ion. So Ω_T needs to be higher than $2\pi{\cdot}25$ MHz, but not too high as every increase of Ω_T also lowers the resulting confinement of the pseudopotential.

For electric DC-field compensation we apply voltage offsets to each trap electrode individually. Therefore no additional compensation electrodes are required which facilitates fitting the ion trap in the rather limited space of the BEC vacuum chamber. This implies however, that the potentials of the trap electrodes cannot be interconnected directly. They are RF coupled with transformers instead to ensure phase stability between them.

The RF voltage can be applied to the electrodes of the ion trap in two different configurations, creating the same electric quadrupole potential in the trapping region. Either, two (opposing) electrodes are connected to the RF voltage and the other two to ground, or, the other two are connected to an RF voltage with opposite sign. The latter requires more electronics but gives twice the voltage amplitude between the trap electrodes and, due to its symmetry, holds promise of a lower RF emission and higher Q of the resonating circuit. It also allows to employ the same design of DC offset coupling for all four electrodes.

As main amplifiers we use two dual package RF power MOSFETs (*ARF473*) with a common source. They are specified for outputs of up to 300 W and 13 dB gain per pair. Using a DDS with 0 dBm output as a frequency source, a preamplifier is needed to increase the input signal for the power MOSFETs. The gain of the MOSFETs is adjusted by changing the gate-source offset voltage. As each of the four MOSFETs has a slightly different threshold voltage (see Fig. 2.10), we use four computer controlled analog channels to set gate-source offset voltages individually. Due to the size of the MOSFET, the gate has a rather large capacitance. A transformer matches the resulting low impedance to the 50 Ω input and distributes power to the four MOSFETs.

A schematic of the RF drive for two electrodes is shown in Fig. 2.8. The supply voltage is DC-coupled to the source of the MOSFET, while AC-coupling connects the RF-output to step-up transformers. These increase the RF-voltage for the trap electrodes and are required to match the impedance of the ion trap to the amplifier's output. The two electrodes shown are driven in phase enforced by transformer T7. Up to now, the port COM is not connected and the phase difference between opposing trap electrodes is estimated to be less than 0.001 (for the determination of this number see section 3.2). Compensating this small phase difference could be achieved in two different ways. Connecting the port COM to ground allows to

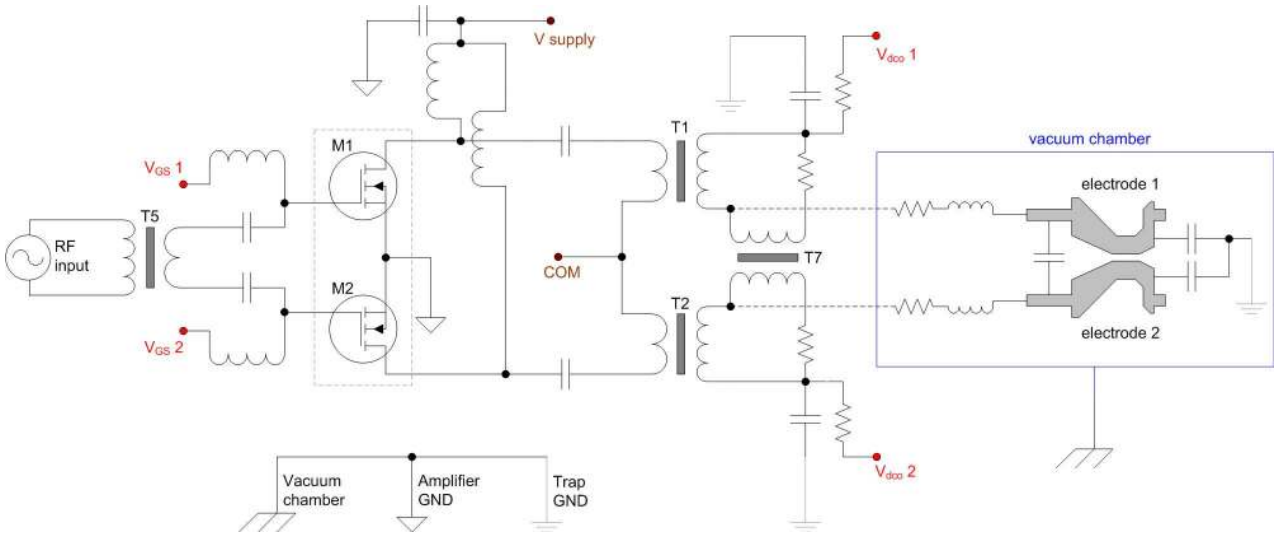

Figure 2.8: Schematic of RF drive electronics. Left of the amplifier MOSFETs (M1 and M2) is the RF input with impedance matching (T5) connected to the MOSFET gates. The MOSFET source is connected to the supply voltage through a low pass filter and to the RF output side. T1 and T2 are transforming high current into high voltage. T7 is used to balance the phase between the electrode's RF-voltages and also to tune the resonance of the circuit. The connection to the trap electrodes is modelled to be resistive and inductive, the trap itself as a capacitance between the electrodes. The schematic only shows two RF channels with the same phase. In the hardware, this circuit is implemented twice to power all four electrodes. A full electric circuit model needs to account for capacitive and inductive coupling between all four electrodes and the additional end-caps.

unbalance the RF powers between T1 and T2 by changing the separate gate offsets. The first way to compensate small phase differences makes use of the induced phase shift of T7 when transmitting power from the stronger side to the weaker. The other way is to remove T7 and drive each RF voltage amplification line with a separate DDS channel. Phase offsets can then be programmed to the DDS directly. Also, removing T7 should increase the RF voltage output and allow for full tunability of voltage amplitudes for each electrode individually.

2.4.2 Hardware

The ion trap driving circuit is mounted on a double-sided printed circuit board (PCB). Fig. 2.9 shows a picture of the fully equipped PCB. The power MOSFETs are located in the centre, under the copper blocks, which are used to cool them. On the left side is the RF input with impedance matching circuit and another MOSFET which is currently not used. The high power section is situated on the right side of the PCB. Between the MOSFETs and the ring core transformers is the high current section and to the right side of the transformers, the high voltage section. The high current and high voltage sections look almost identical on the back side of the PCB (not visible in the picture). The upright ring core transformers in the high voltage section correspond to T7 of Fig. 2.8. The central part in the high power section is the

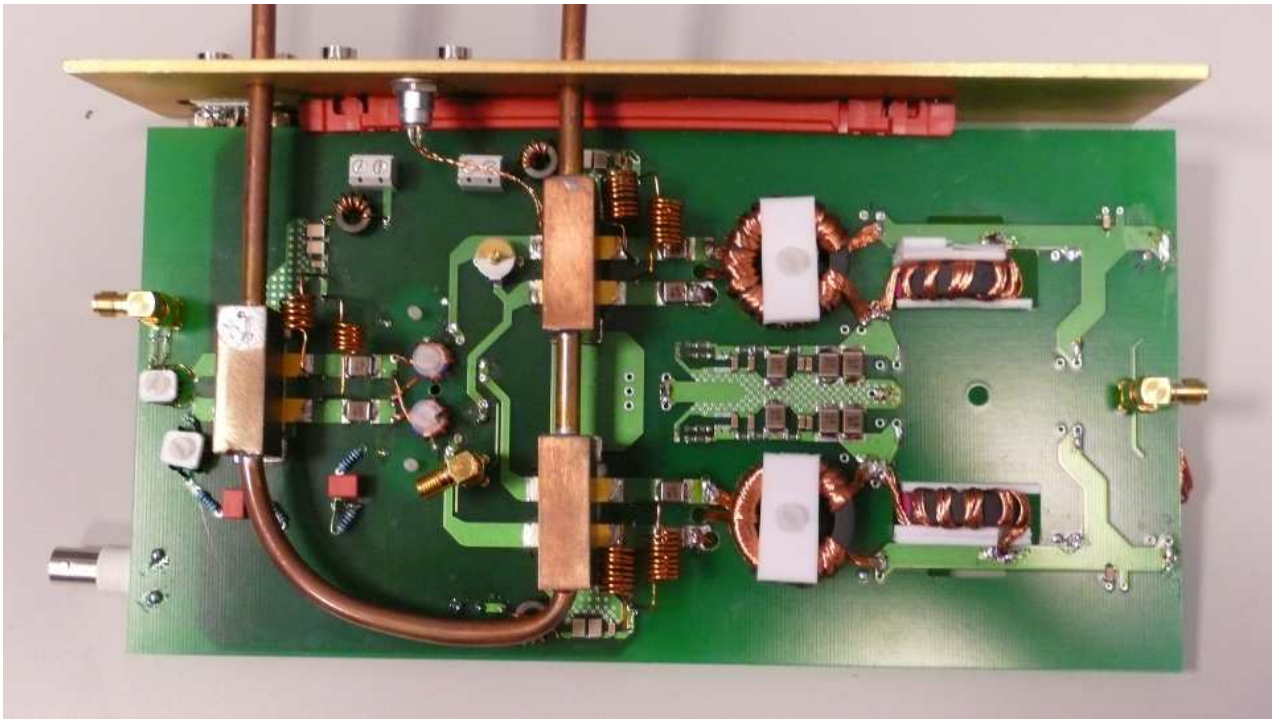

Figure 2.9: Assembled RF drive PCB. The main amplifier MOSFETs are below the water cooled copper blocks in the center of the image. On the left side is the RF input, on the right side the RF-output. On the back side of the PCB there is an identical RF-output stage. On the very right edge of the board, four contacts (two visible) are placed to connect the circuit to the trap electrodes.

trap ground with capacitive coupling, and the connection to the computer controlled electrode offset voltages via several low-pass filters. The PCB, and especially the high power side, has been designed with as much symmetry between the four channels as possible. The ring core transformers are the elements which create the strongest imbalance as they are wound by hand. The ring cores are of the type *Amidon FT114-67* and have an inductance of 25 nH per square winding. The windings are made from Litz-wire with 120 strands, T1 and T2 have 1:16 primary to secondary windings and T7 has 6:6. The MOSFETs require water cooling, as they can easily dissipate up to 100 W. A stable water temperature is helpful as the gain behaviour of the MOSFETs change with temperature. Today, the water cooling is provided by a small chiller situated in our lab, with temperature fluctuations of less than 0.1 K. Before 2010, the house cooling water was used and temperature fluctuations of several degrees regularly caused the trap drive to fail. A temperature interlock has been designed to prevent damaging the MOSFETs in such events. The temperature sensor can be seen in Fig. 2.9 on the left side of the upper copper block. The interlock will disconnect the supply voltage from the drive when the temperature exceeds a certain limit, and has to be manually reenabled thereafter.

To monitor the drive output, two measurements are continuously taken and logged with the DECADS software once every 2 s, cf. Fig. 2.14. An analog-to-digital converter reads the

supply current drawn by the drive. The current value is used in an additional, software based interlock loop, also disabling the drive by ramping down the gate voltages, in the case of failure. The increased current detection is faster and the soft switch off procedure is less abrupt than disconnecting the supply voltage, and gives a better protection to the MOSFETs therefore. Also, as the software is aware of this type of failure, it can shut down other systems (such as trap reloading) and enable an acoustic alarm. The second observable which is continuously measured is RF power from a pick-up wire. The pickup is integrated on the drive PCB and can be seen on the very right end of the board. It is connected through an SMA cable to a 50 Ω terminated RF power sensor board. This board has been custom designed and data are read-out with the help of the microcontroller described in section 2.1. RF powers can be measured over a range of 90 dB with less than 0.025 dB RMS noise. This allows to see very small fluctuations in the power output of the drive. In the previous case with the house cooling water and its temperature fluctuation, an active feedback loop has been successfully implemented in the software, adjusting the gain of the drive to keep the measured RF power stable. However, today this feature is not required anymore due to the stable water temperature and the pickup power can be used as a reliable indicator of the drive stability.

2.4.3 Characterization

A first set of parameters, which have to be determined before enabling the drive, are the MOSFET gate threshold voltages. The datasheet of the *ARF473* only states the threshold to be between 3 V and 5 V, but no typical value is given. The threshold is measured without using any RF, just by applying a supply voltage to the drain of the MOSFET and measuring the DC drain-source current I_{DS} for different values of the gate-source voltage V_{GS}. Such a measurement for all four MOSFETs is displayed in Fig. 2.10. The main observable difference between the four measured curves are shifts along V_{GS}. A balanced calibration is obtained by adding an individual compensation value for the gate-source voltage of each MOSFET channel in the software. Note that the presented measurement can be repeated at a later time to detect (or rule out) MOSFET ageing effects.

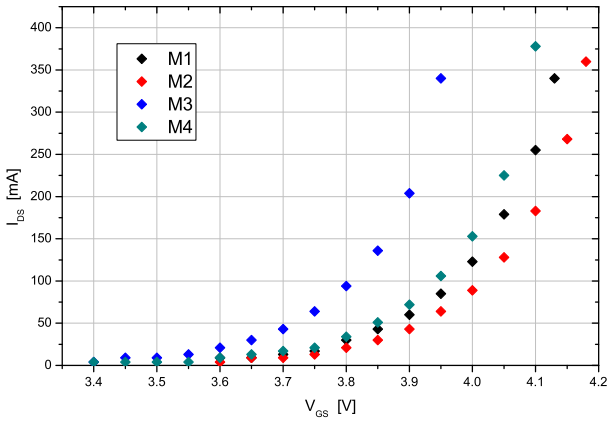

Figure 2.10: Measured MOSFET conductance for a supply voltage of $V_{DS} = 75$ V. The drain-source current I_{DS} is measured for different values of the gate-source voltage V_{GS} for each MOSFET individually (different colors). Due to variation in threshold values, the measured curves appear shifted along V_{GS}.

Also, this measurement can be performed on the drive disconnected from the ion trap, as effects from the resonant circuit are not required.

When connected to the RF input and the ion trap, the resonance of the trap drive circuit can be searched for. The procedure is to set V_{GS} to some small value, switch the DDS output to a random frequency Ω_T, wait for a short time and measure the RF power from the pickup. Measurements of this type for different V_{GS} are shown in Fig. 2.11. At higher V_{GS} and hence higher power dissipation of the MOSFETs, thermalization times get longer as the supply current drawn also changes for different frequencies. However, the position of the resonance shifts only slightly for different drive powers. Once the resonant Ω_T is known, V_{GS} is increased to the value for trap operation (3.92 V in our case), and a final small adjustment is made to Ω_T to optimize the ratio between measured pickup power and the total power dissipated by the drive.

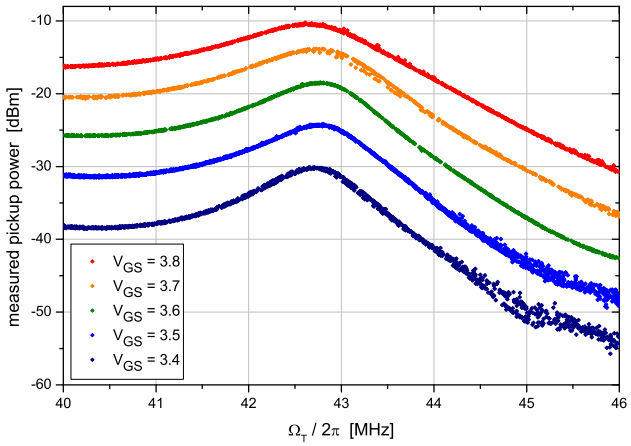

Figure 2.11: The RF-resonance of the trap driving electronics is found by varying Ω_T while monitoring the drive pickup power. The shape and position of the resonance change slightly for different powers.

To get an estimate of the RF voltage amplitude V_0 on the trap electrodes a calibration of the pickup signal is required. Measuring V_0 is however difficult. The most direct approach is to connect the electrodes to an oscilloscope. As the ion trap is not accessible inside the vacuum chamber, the probes have to be connected to the electrical feedthrough instead. The voltage drop from the feedthrough to the trap electrodes is therefore creating a bias towards an overestimation of V_0. Also, connecting the probes to the resonant circuit will alter it in a non predictable way. Fig. 2.12 shows a measurement of the voltage amplitude V_0 compared to the detected pickup power. An extrapolating fit towards higher pickup values is displayed which uses an offset as the only free parameter, the slope is fixed to the expected 20 dB for each voltage increase by a factor 10. An indirect but more accurate approach to calibrate the pickup power is to use measured ion trap frequencies to calculate V_0. This procedure is explained in section 3.3. The calculated voltages V_0 are more than a factor 2 below the extrapolating fit. This is most probably due to the before-mentioned disturbance of the resonant circuit and the neglected losses on the RF transmission from the feedthrough to the trap electrodes. The former is confirmed by comparing the ratio between measured pickup power and the total by the drive dissipated power for the two sets of data. In the case of directly probing V_0 with an oscilloscope this ratio is not a constant and it is more than 300

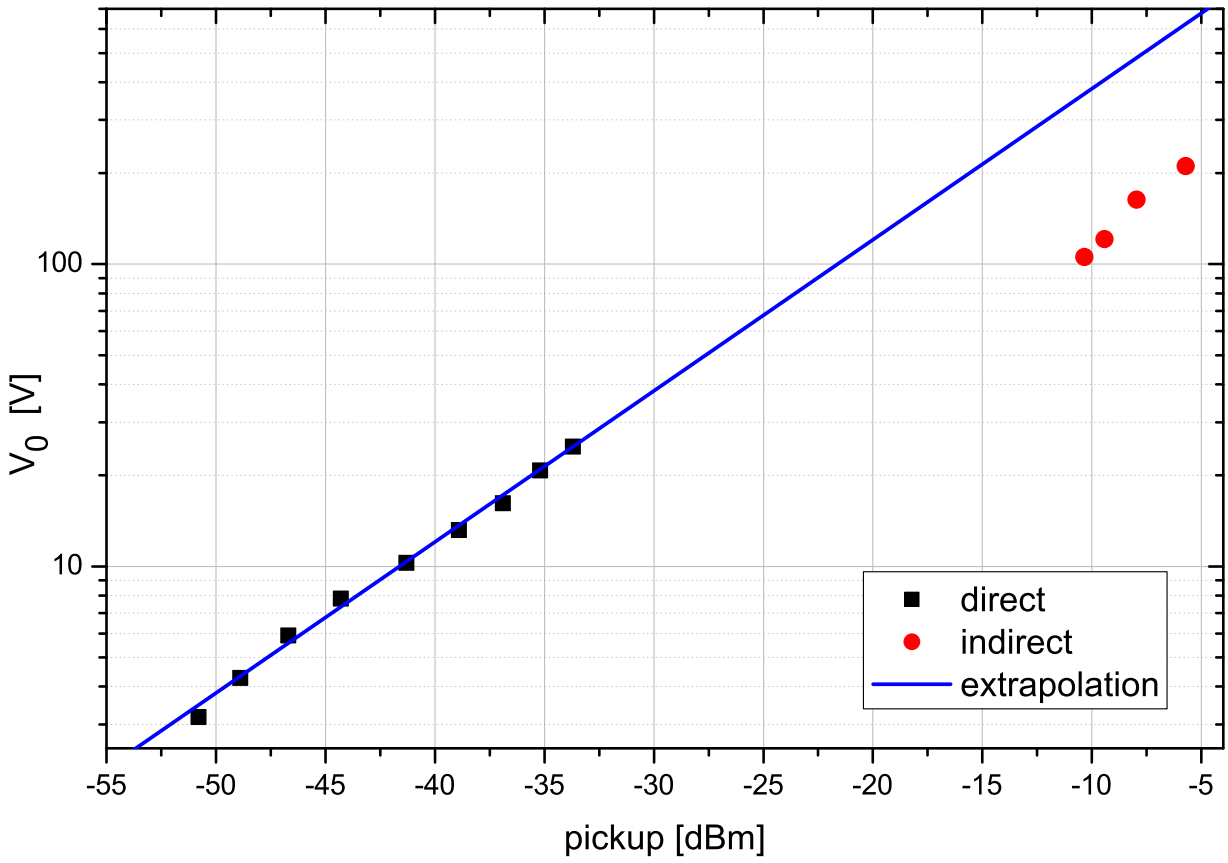

Figure 2.12: Two different measurements are compared to calibrate the RF-pickup signal. The direct measurement (black) of the RF voltage amplitude V_0 is obtained by connecting an oscilloscope to the electrodes. The indirect determination of V_0 (red) uses the measured ion trap frequencies and the geometric efficiency of the quadrupole field. The extrapolation of the direct calibration does not fit with the more accurate indirect calibration. The slope is assumed 20 dB per factor of 10 in voltage.

times smaller than the ratio obtained during the trap frequency measurement.

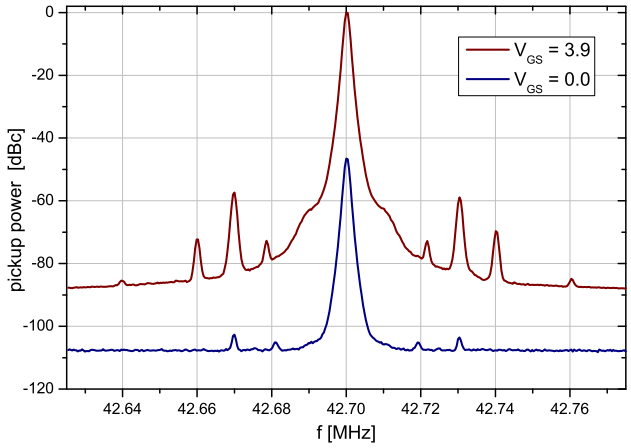

Figure 2.13: The spectrum of the RF-signal is measured with an *Agilent E4407B* Spectrum Analyzer. The settings are RBW = 1 kHz and VBW = 100 Hz. The spectrum is measured once with the enabled drive (red) and with the disabled drive (blue). The noise level and the narrow sidebands are well suppressed.

The pickup signal can also be used to determine the RF-signal width and noise, and to detect possible sidebands. For this measurement the pickup is directly connected to a spectrum analyzer, a sample spectrum obtained is shown in Fig. 2.13. The noise background is more than 80 dBc suppressed 35 kHz away from the carrier at $\Omega_T = 2\pi \cdot 42.7\,\text{MHz}$. Sidebands are seen at 21.5 kHz, 30.25 kHz and 40.1 kHz, all are suppressed by about 60 dBc or more, and narrower than 100 Hz. Except for the sideband at 40.1 kHz they are detected even when the drive is disabled, which means they stem from the noise picked up before the preamplifier or from the DDS which is specified with a noise background of 60 dBc. The sideband at 40.1 kHz might be introduced by the power supply used to provide the 75 V of supply voltage for the drive. As all these sidebands are strongly suppressed and narrow, no strong heating effect on a trapped ion is expected.

Stable power output from the RF drive requires the MOSFETs to be at a constant temperature, because the gate thresholds decrease with increasing temperature. The initial thermalization time after enabling the drive is on the order of 30 s, depicted in Fig. 2.14. Disabling the drive for short times, used for example to intentionally empty the ion trap, does not have a significant effect on the MOSFET temperature and the output power recovers instantly.

2.5 Interlock System and Temperature Recording

In order to optimize the statistics from the collision measurements between the single ion and the ultracold neutral atoms, we have maximized the time of data-taking by running the experiment in a continuous mode, 24 hours per day and 7 days a week. This also resulted in less drifts, as the whole setup achieves a better thermal equilibrium. To prevent the system from being excessively damaged in unexpected events, an interlock system has been designed. It consists of a reliable hardware part and a flexible software part.

The hardware part controls all the high current power supplies, the optical dipole trap laser and a valve in the main supply pipe of the cooling water. If an error occurs, all these systems are disabled. The hardware continuously monitors the temperature of the magnetic coils, senses water on the laboratory floor and the experiment tables to detect cooling water leaks,

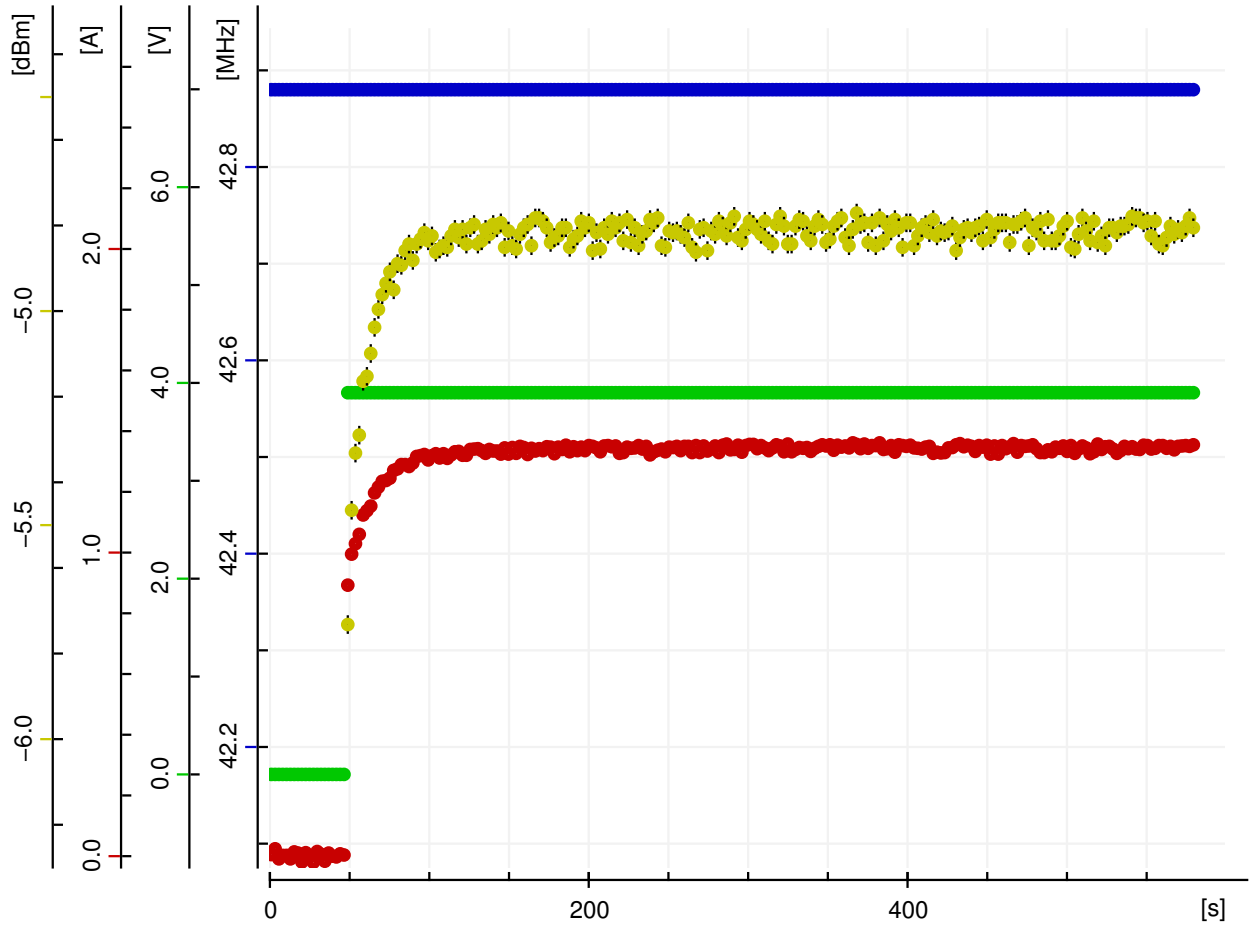

Figure 2.14: Graphical output from the software to monitor the trap drive. The drive power pickup signal (yellow) and the supply current (red) are measured values. The average gate-source voltage (green) and the drive frequency (blue) are output parameters. In the data shown, the drive is enabled at $t \approx 50\,\mathrm{s}$ and runs stable about 30 s later when the MOSFETs reach thermal equilibrium.

checks for sufficient cooling water flow and detects interruptions of the mains supply voltage. In combination, the interlock system is able to prevent flooding and critical overheating of the experiment setup. When the system has detected an error, it needs to be re-enabled manually.

A software interlock cannot provide the same degree of safety, as it relies on error free operation of the software. However, it comes with the advantage, that the critical values, which can lead to a shut-down of the experiment, are continuously recorded and can be inspected to find the cause of the shut-down. Currently, our software interlock only monitors the magnetic coils temperature, redundantly with the hardware part. An additional switch off signal is provided from the software to the hardware part of the interlock system, therefore combining the advantages of error reproducibility and the higher safety of the hardware system.

Beside emergency switch off, temperature recordings from various points in the experiment have proven to be a useful data source for analyzing the system's thermal behaviour, or to

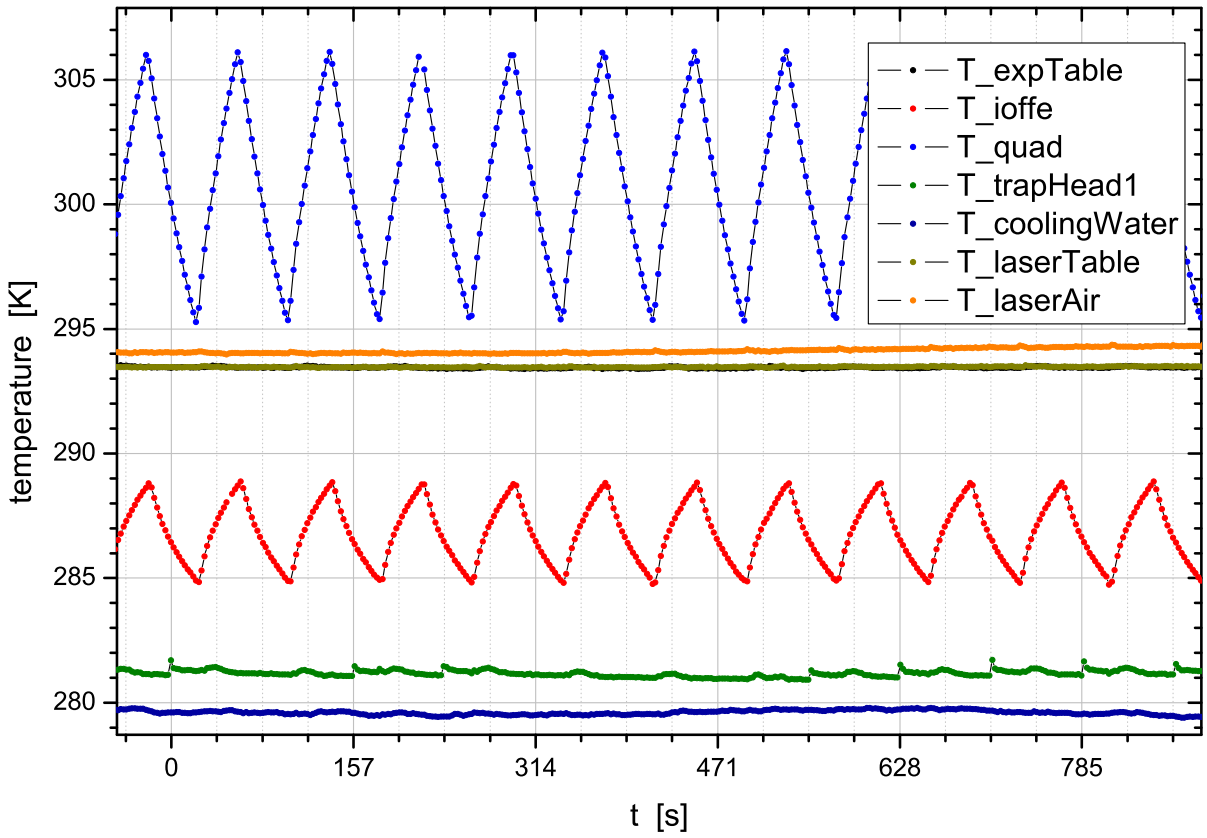

Figure 2.15: Temperature recordings from seven different locations of the experimental setup. The readings from the magnetic coils (blue for one of the quadrupole coils and red for the Ioffe coil) show the strong temperature increase during the time they are enabled within every cycle of $\sim 87.5\,\mathrm{s}$ in length. Some uncorrelated fluctuations and drifts can be observed on the cooling water temperature (dark blue) and the experiment tables and air (yellow, black and orange, the black data is mostly hidden behind the yellow). The temperature of the ion trap head (green) experiences a small temperature increase at the beginning of those cycles where the oven is fired. It can be seen in the presented data at $t \in \{0, 157, 235.5, 549.5, \ldots\}$.

search for correlations between temperature variations and effects measured with the ion or the atoms. A printed circuit board to measure temperature on four channels has been designed, which connects to the previously described microcontroller on the clock generation board (see section 2.1). The circuit is compatible with standard PT100 temperature probes and a four wire connection is used to minimize transmission line errors. A high resolution analog-to-digital converter reads the resistance of the probe, which is converted into the corresponding temperature by the software. The observed RMS-noise on the recorded temperature values is below 10 mK. The sensors are slightly sensitive to strong microwave and RF-fields present in our setup, however the observed offsets are reproducible and below 200 mK.

We have currently seven temperature sensors in use for the continuous data recording. Two sensors on the magnetic coils keep track of the strong temperature increase during the part

of the experimental cycle, when the magnetic coils are enabled, see Fig. 2.15. The magnetic coils, even though they are water cooled, are the strongest heating elements directly affecting the experiments. The average temperature of the coils within one experimental cycle is a good measure to see if the system runs thermally stable. After a change of the currents for the magnetic coils the thermalization typically takes about 30 min. The sensors on the experiment and the laser table mainly monitor the stability of our air-conditioning. They help diagnosing problems with lasers not running stable. The stability of the cooling water temperature is essential for good experimental conditions as it is used to cool, among other parts of the setup, the ion trap and the ion trap drive. The one temperature sensor operating within the vacuum chamber is glued to the ion trap head, directly next to the Yb-oven (cf. Fig. 1.11). It registers a temperature increase of a few 100 mK whenever the Yb-oven is fired, a convenient way to check if the oven is working.

Chapter 3

Methods

In this chapter, the methods of system preparation, calibration and data retrieval will be introduced. Preparing the ion trap involves loading a single ion, compensating the micromotion and characterizing the ion trap geometry. To determine the temperature of the ion, we use the fluorescence light during Doppler cooling as a signal. The calibration of electric fields is crucial to ensure a fixed position of the ion. The alignment between the ion an the neutral atom cloud is achieved by displacing the trap centre for the neutral atoms relative to the ion trap. The independent control over the two is discussed. The neutral atoms are absorption-imaged after a few milliseconds time-of-flight, providing information on density, temperature and structure, and the trap for the neutral atoms is characterized by its harmonic frequencies.

3.1 Single Ion Loading

Different from most other experiments with trapped ions, where ions typically stay trapped for very long times, in collision experiments with cold atoms the loss of an ion tends to occur more frequently. Ion losses are even required by some types of measurements, predominantly when investigating inelastic collisions. Our fast and automatic trap reload procedure has therefore allowed us to acquire data in an affordable amount of time. In this section, the procedure of automatically preparing one single ion in the trap will be explained.

To control the number of ions we use three basic procedures, the loading of the trap, partially unloading the trap and fully emptying the trap. The latter is achieved by simply switching the trap drive off for a short time on the order of 100 ms. The trap is typically emptied before reloading, in order to get rid of any dark ions, which could be Yb ions in the F state or ionized Rb atoms. The time of loading of the trap is fixed to the end of the experimental cycle when the power supply is available for the Yb oven as at that time, it is not used for driving magnetic coils.

Just before the oven is fired, the ion cooling laser at 370 nm is red detuned by approximately $-20\,\Gamma$, and its intensity is increased for higher ionization efficiency. The oven is heated by the current pulse and emits neutral Yb atoms, as seen in Fig. 1.12a. As they pass the centre

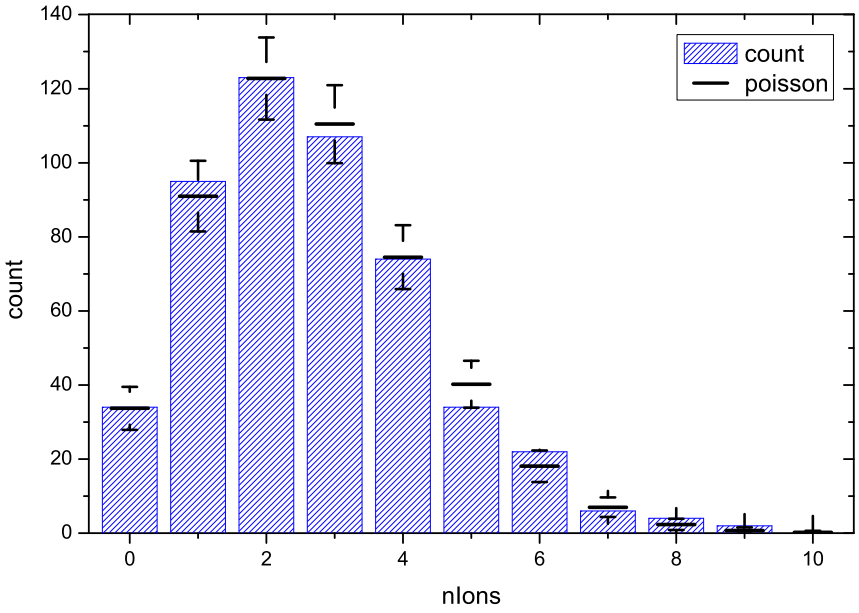

Figure 3.1: The loading statistics is obtained by registering the number of ions directly after loading the previously empty trap. The shown data (blue bars) consist of 501 repetitions, taken within three days with an average number of ions loaded of 2.7. The calculated Poissonian distribution is plotted for comparison with error bars indicating the variation expected from shot-noise.

of the trap, a fraction of these atoms are ionized in a two-step process with the two lasers at 398 nm and 370 nm. After the oven has cooled down, the ion cooling laser frequency is ramped slowly up to a detuning of $-0.5\,\Gamma$ at our normal operating laser intensity ($I/I_{sat} \approx 2.5$). At this point the trapped ions are cold and can be detected by the fluorescence rate and with the CCD-camera. The number of ions is quickly identified by using the algorithm described in section 2.3.2 and it follows a Poissonian distribution, shown in Fig. 3.1. The average loading efficiency, given by the mean of the distribution, depends on a number of factors. It is most sensitive to the power of the laser at 370 nm, which lets us conclude that this is currently the most limiting factor. Also, the axial confinement of the ion trap can have a significant effect. Probably due to static charges, the trapping region can shrink and hence the capture of the initially hot ions becomes inefficient. Therefore, raising the axial confinement typically increases the loading efficiency. Changing the end temperature of the oven by altering the current also directly affects the mean number of ions loaded, independently of the other factors. The optimal loading efficiency to prepare a single ion is found for an average between 2 and 3 initial ions, as this already reduces the chance of not loading any ion to some acceptable value, while at the same time avoids to load too many ions.

Following the detection of the number of ions loaded, the control system decides to partially unload the trap if more than one ion remains. To this end, the axial confinement is lowered to a critical value, such that a trap loss becomes probable. The confinement is ramped back to its

normal value and the number of ions is measured again. The procedure is repeated iteratively until only a single ion remains. A typical sequence of trap loading and three consecutive partial unloads is illustrated in Fig. 3.2. The number of possible iterations of the partial unloading is limited to about six, by the available time within the experimental cycle and the image acquisition time needed to detect the ions.

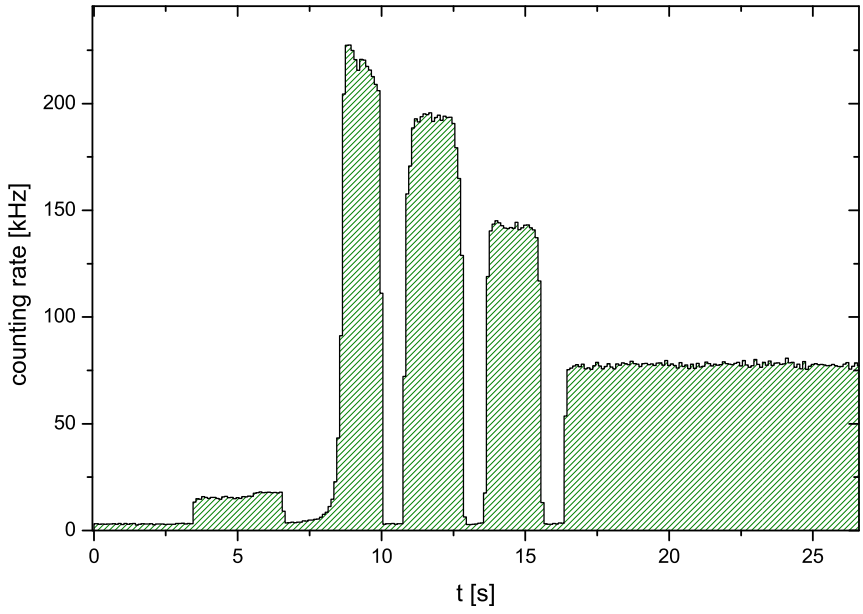

Figure 3.2: The fluorescence count rate at 370 nm is recorded during a trap load and partial unload sequence. The photons are binned in intervals of 100 ms length. The sequence starts by detecting an empty trap. During the oven firing at $t \approx 5\,\mathrm{s}$, the frequency of the UV light is red detuned and its intensity is increased to ionize more efficiently, seen by the increased stray light. Then the intensity is reset to lower power and the detuning is ramped to $-\Gamma/2$. Once the ions are cold and brightly fluorescing, the number of ions is detected. A partial unload follows, during which the fluorescence reduces significantly as the ions move out of the centre of the trap. The ion number detection and partial unloads are repeated until there is only one ion left. In the presented example the initial number of ions is four, then reduces with each partial unload by one, to end with a single ion at $t = 17\,\mathrm{s}$.

Unfortunately, the optimal choice for the critical value of the axial confinement to partially unload the trap is not a constant. Due to the accumulation of static charges that value drifts with time. Therefore, the critical value needs to be adjusted dynamically. Each partial unload sequence provides some information of that critical value. The procedure can either be successful, not effective, which means the confinement has not been lowered enough, or over-effective, which means the confinement has been lowered too much and all ions have been lost. Ideally the procedure operates on the boundary between successful and not effective, as loosing all ions results in the one experimental cycle being lost for the data acquisition of the main experiment, while being not effective just means that the partial unload has to be repeated a few times more. The feedback loop on the critical confinement value increases or

lowers its value depending on the effectiveness of the last iteration: After a success the value is slightly increased. This ensures to move towards the boundary between being successful and ineffective. After an ineffective iteration the value is lowered by a slightly bigger amount. And in the rare case of an over-effective iteration, the value is increased by a large amount. The simplicity of this method allows to manually overwrite the low confinement value without disturbing the automatic feedback. The effectiveness of the method has proved high over extended measurement times and it works reliably. A sample is presented in Fig. 3.3. It is based on the same dataset used for Fig. 3.1. In 372 events, more than a single ion has been loaded initially. In 88% of these events, the partial unloading procedure has been successful in preparing the single ion. In 9% all ions have been lost and in 3% more than one ion has been left after six iterations. Including the probability of loading a single ion directly from the start, the overall efficiency of reloading and preparing exactly one ion is 84%.

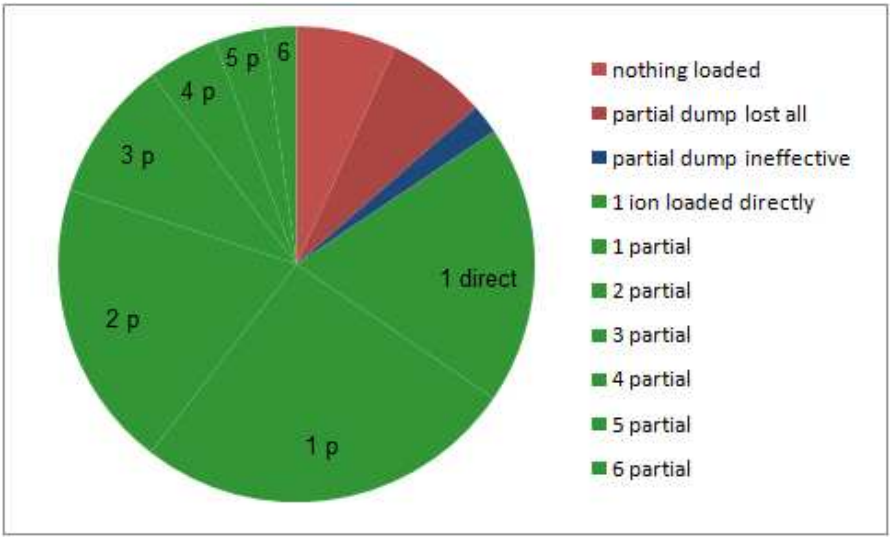

Figure 3.3: Depicted is the occurrence of possible outcomes from a trap reload procedure. In 14% no ion is available, half because no ion has been loaded and half because it has been accidentally unloaded. In 2% of the cases more than one ion stays trapped after a series of inefficient unloading sequences. In the other 84%, a single ion is successfully prepared, 65% of which after applying at least one partial unload procedure. The data shown correspond to those of Fig. 3.1.

3.2 Micromotion Compensation

The level to which excess micromotion can be reduced plays a crucial role in experiments with trapped ions and cold neutral atoms. This is because energy from the RF-driving field mixes via the micromotion with the energies of ion and neutral atoms through collisions, which will be described in more detail in chapter 4 and 5. Therefore, compensating the excess micromotion is the way to reach lower collision energies, improve the localization of the ion within the ultracold gas, and to progress towards experiments observing quantum effects.

3.2.1 Excess Micromotion Contributions

In the linear RF-Paul trap the intrinsic micromotion is given by

$$\vec{v}_{mm,int} = \sqrt{2}\,\omega_p \begin{pmatrix} r_{sec,x}(t) \\ -r_{sec,y}(t) \\ 0 \end{pmatrix} \cos(\Omega_T\, t)\ , \tag{3.1}$$

which forms the pseudopotential necessary to trap the ion. Additionally, excess micromotion can be defined in a generic way,

$$\vec{v}_{mm,exc} = \sqrt{2}\,\omega_p \left[\begin{pmatrix} c_x \\ c_y \\ c_z \end{pmatrix} \cos(\Omega_T\, t) + \begin{pmatrix} s_x \\ s_y \\ s_z \end{pmatrix} \sin(\Omega_T\, t) \right]\ , \tag{3.2}$$

including terms for all three spatial dimensions, and for being in or out of phase with the main driving field. In the experiment consequently, the six parameters have to be measured and appropriate corrections need to be applied to the system in order to minimize the six parameters. Usually, the strongest contribution to excess micromotion, and also the easiest to compensate, is represented by the parameters c_x and c_y. They correspond to a displacement of the minimum of the ion trapping potential relative to the centre of the RF-quadrupole field. The displacement can be caused by static electric offset fields and is accordingly compensated by adjusting the controllable offset fields $\vec{E}_{dcoV}$ and $\vec{E}_{dcoH}$. The contributions s_x and s_y relate to small phase shifts between the RF-voltages on diagonally opposing electrodes [91]. Lets assume a phase shift $\delta \ll 1$, then the voltage between the electrodes is proportional to $\delta \cos(\Omega_T\, t)$. At the position of the ion, this leads to a homogeneous electric RF-field, which is $\pi/2$ out of phase from the trap driving field. Compensating this type of micromotion should be done by individually adjusting the phases of the RF-voltages for each electrode. (In our apparatus, the electronics to do so is ready, however, with the low measured s_x and s_y there has been no necessity to use it so far.) The excess micromotion contributions along the trap symmetry axis, c_z and s_z, can be a result of RF pickup on the end-cap electrodes or a consequence from

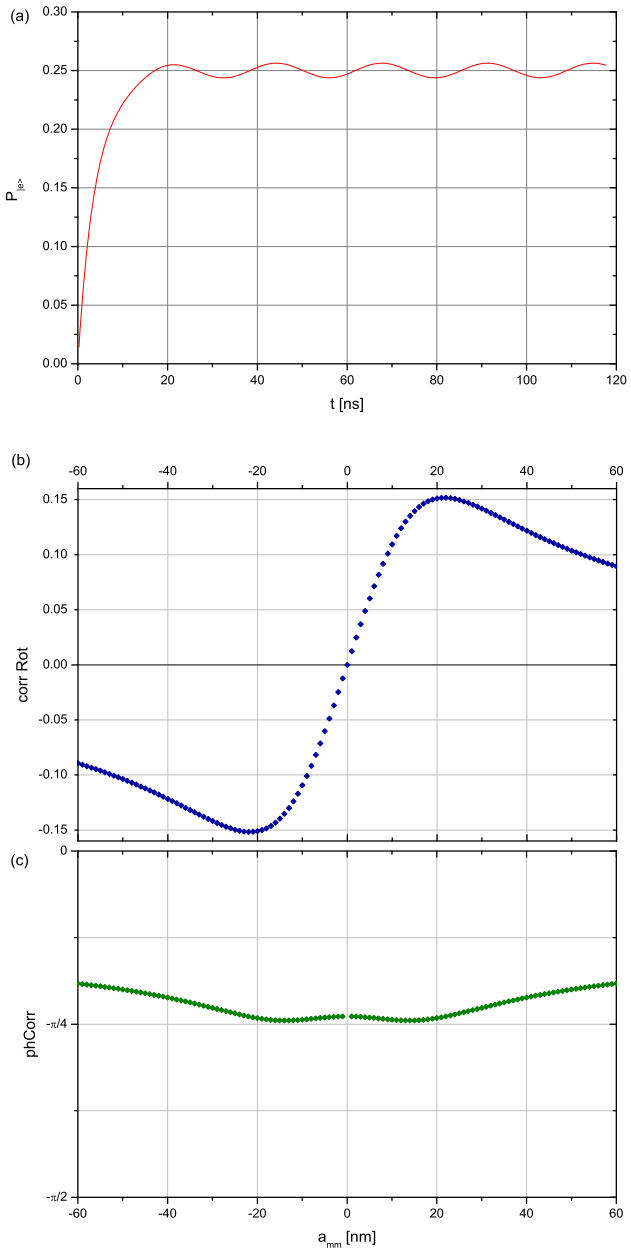

Figure 3.4: (a) The evolution of the excited state $P_{|e\rangle}$ (red) is shown for the first five periods of the driving RF, for $a_{mm} = 1\,\mathrm{nm}$. (b) The amplitude (blue) and (c) relative phase (green) of the converged modulation on $P_{|e\rangle}$ are plotted against a_{mm}. The laser settings are $I/I_{sat} = 2.0$ and $\delta = -0.5\,\Gamma$.

a geometrical asymmetry in the alignment of the ion trap electrodes. Compensation might be achieved by feeding an additional RF-voltage to the end-caps.

3.2.2 Photon Correlation Model

In our system, we use a photon correlation technique [92, 91] to measure the six parameters of the excess micromotion. It builds on the simple idea that the photon scattering rate of the ion is modulated through the Doppler shift. Hence, if the velocity of the ion varies as in Eqn. (3.2), the scattered light intensity is expected to be modulated at the frequency Ω_T. For perfect micromotion compensation this modulation is expected to vanish. The Doppler shift is only effective if the micromotion velocity comprises a component along the laser exciting the ion ($\vec{v}_{mm,e} \cdot \vec{k}_{Laser} \neq 0$). Therefore, in order to probe all the six micromotion parameters, at least three different laser beams are required, which do not lie in a single plane. Ideally, each beam can then be used to measure the micromotion along one main axis. However, due to experimental constraints on optical access, this is only approximately realized for the vertical beam, while two beams in the horizontal plane measure both some different linear combinations of micromotion along the remaining two main axes.

A quantitative approximation of the photon scattering rate, dependent on the momentary velocity of the ion, can be obtained from solving rate equations for a two-level system. The probability $P_{|e\rangle}$ to find the ion in its excited state can be modelled with the

differential equation

$$\frac{\mathrm{d}}{\mathrm{d}t}P_{|e\rangle} = -\Gamma\, P_{|e\rangle} + \frac{\Gamma\,(\Omega/2)^2}{\delta_{eff}(t)^2 + (\Gamma/2)^2}\,(1 - 2\,P_{|e\rangle}) \tag{3.3}$$

with

$$\delta_{eff}(t) = \delta - (\vec{v}_{mm,e} \cdot \vec{k}_{Laser})\,\cos(\Omega_T\, t)\ , \tag{3.4}$$

where Γ is the natural linewidth of the cooling transition, Ω the Rabi frequency and δ the detuning of the cooling laser frequency from the ion's resonance. This model neglects coherence between the excited and the ground state of the ion. It is used here as an approximation to see how the micromotion connects to the photon correlation and is strictly valid only for $\Gamma \ll \Omega_T$. A numerical integration of Eqn. (3.3) provides information on the light modulation at the frequency Ω_T, see Fig. 3.4a. After a time a few Γ^{-1} long, the numerical solution for $P_{|e\rangle}$ converges to a constant mean plus a modulation of a certain amplitude and with a relative phase to the driving field. They can be evaluated using a similar method as the calculation of correlations described by Eqn. (2.5). Fig. 3.4b and c show how the amplitude and the phase of the correlation change, when the amplitude of the micromotion is increased. Close to the compensated case ($|a_{mm}| \lesssim 10\,\mathrm{nm}$), the phase can be approximated by a constant and the amplitude as being proportional to a_{mm}. In this linear regime, the slope of the correlation amplitude and the constant phase both depend on laser detuning and intensity, shown in Fig. 3.5. Stable laser parameters thus facilitate the determination of micromotion.

3.2.3 Averaging Effects

Averaging effects play an important role when deducing the excess micromotion parameters from the experimentally measured photon correlation. Eqn. (3.4) models only the simplified case where there is no secular motion involved ($\vec{r}_{sec} = 0$, in Eqn. (3.1)). However, the real $\vec{r}_{sec}$ fluctuates corresponding to a finite temperature of the ion on a timescale given by the inverse ion trapping frequency. If the photon correlation is measured on a sample much longer than this timescale, then correlations originating from the intrinsic micromotion average to zero and do not affect the measurement. This statement is true in the linear approximation of the RF field and for homogeneous illumination of the area the ion is in. For an asymmetric light intensity profile over the region the ion is distributed in, non-zero correlations can be expected even with an optimally compensated trap. In the experiment, the Gaussian laser beam profiles should therefore be carefully centred on the ion to prevent systematic errors in micromotion determination. Note that the averaging mechanism is a special virtue of the photon correlation measurement. Other techniques, such as micromotion sideband detection can be limited by the thermal noise.

The effect of electric offset fields, which fluctuate on a timescale shorter than the correlation measurement length, will also be concealed by the averaging mechanism. We have considered

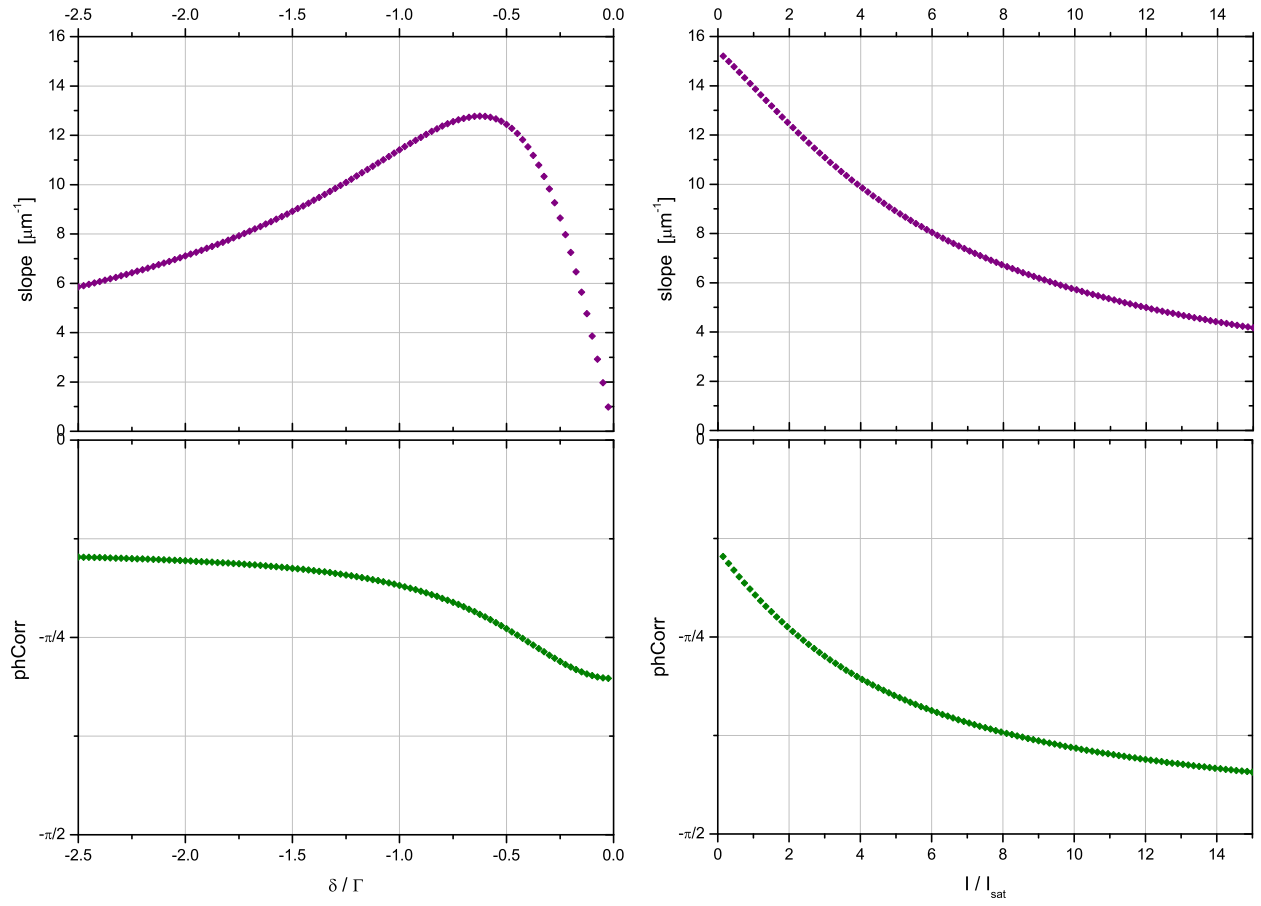

Figure 3.5: Numerically calculated slope (purple) of the correlation signal and its phase (green) relative to the driving RF. On the left side the dependence on laser detuning is shown for an intensity of $I/I_{sat} = 2.0$, on the right side the dependence on laser intensity for a detuning of $\delta = -0.5\,\Gamma$.

the possibility of electric offset fields changing with the mains frequency of 50 Hz. Such well defined, single frequency modulations of electric fields would leave a correlation signal at sideband frequencies $\Omega_T \pm 50\,\mathrm{Hz}$. However, no such sidebands have been observed.

3.2.4 Systematic Corrections

The setup described by Fig. 2.2 together with the function (2.5) is used to retrieve the phase and amplitude of the photon correlation from the scattered light. Before attributing this correlation to the ion fluorescence light, two points need to be considered to prevent systematic errors. Firstly, technical noise can introduce additional, false correlations. Secondly, ion fluorescence light is typically seen on top of a background rate, which reduces the measured relative amplitude of the correlation.

Evaluating Eqn. (2.5) on uncorrelated stray light yields a non-zero correlation $c_{c,dark}$ and $c_{s,dark}$. It stems from electronic RF pickup on the signal between the photon counter and the

time to digital converter. This correlation is constant for a certain ion drive setting and it is independent of the photon counting rate. It is measured during each experimental cycle on stray light, while the ion is kept dark by turning off the repump light. The phase of the dark correlation is constant as long as all the electronics keep being phase-locked, which usually is the case for periods extending over weeks. The dark correlation acts as an offset on any measured correlation, meaning that for no micromotion one expects to measure the same correlation on ion fluorescence light. In data evaluation this is accounted for by subtracting the dark correlation from any measured result of Eqn. (2.5).

Background photon counts result mainly from laser light scattered from the vacuum chamber windows and the ion trap. Background rates γ_{dark} therefore differ for the three laser beams and are measured on each beam separately. As the laser intensities are actively stabilized (with a proportional-integral-derivative (PID) control loop feedback system), γ_{dark} do not change over time. Correlation amplitudes on signals consisting of both fluorescence and background light are reduced by the ratio of the full photon counting rate γ_{full} and the rate of photons originating from ion fluorescence. Multiplication by this ratio rescales correlations to the value expected from pure fluorescence light.

Combined, the two corrections for dark correlation and background light are considered in

$$c_{c,real} = \frac{\gamma_{full}}{\gamma_{full} - \gamma_{dark}}(c_c - c_{c,dark}) \ , \tag{3.5}$$

for the cosine part of the correlation, and the analogous applies for the sine part $c_{s,real}$.

3.2.5 Correlation Measurement

To determine the best compensated values of the electric offset fields $\vec{E}_{dcoV}$ and $\vec{E}_{dcoH}$, we repeatedly measure the correlation (Eqn. (2.5)) within 8 s for various offset fields. The field values are chosen randomly in a small region around the optimal position to stay within the linear regime of Fig. 3.4b. When measuring with the vertical laser beam, we change the horizontal electric offset field $\vec{E}_{dcoH}$, and vice versa, due to the alignment of the RF-quadrupole field. A sample of such obtained correlation values, corrected using Eqn. (3.5), are plotted in Fig. 3.6. The correlation coefficients in the complex plane $(c_{c,real}, c_{s,real})$ are scattered mainly along one phase direction. However, a line fitted through these points does not exactly cross the origin as could naively be expected. This is also reflected in the absolute value of the correlation $(\sqrt{c_{c,real}^2 + c_{s_r eal}^2})$, which is minimal for the optimal offset field, but non-zero. The phase of the correlation can be calculated for each measurement $(\phi_c = \arctan(c_{s,real}/c_{c,real}))$ and asymptotically approximates a constant value for larger offset fields. This asymptotic phase corresponds to the numerically calculated correlation phase plus a technical offset. It can be determined from the measured data. Rotating the correlation coefficients in the complex plane with the asymptotic phase separates the correlation into a component c_{rot}, which maximally depends on the offset field, and its orthogonal complement c_{orth}, which is independent of the

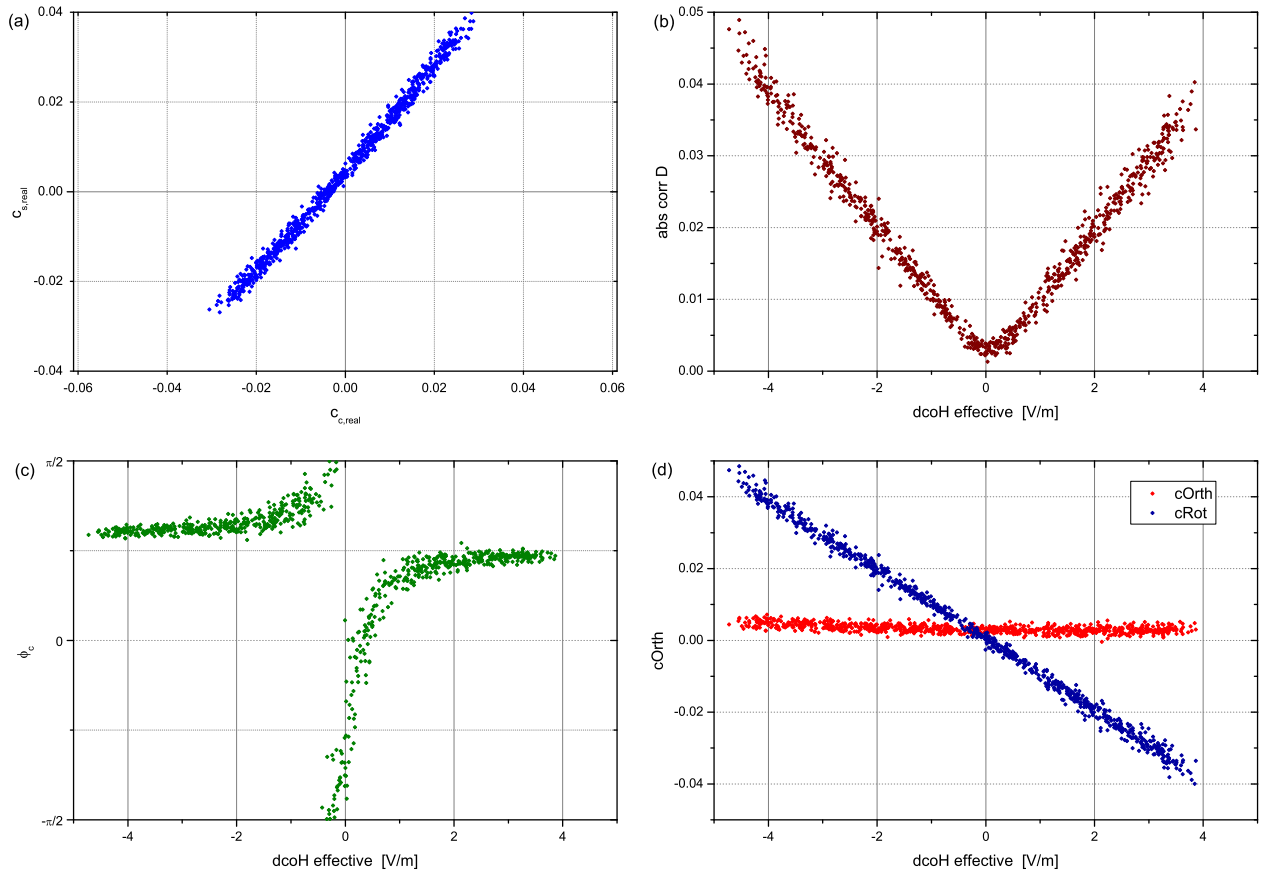

Figure 3.6: Measured fluorescence correlation with the driving RF for various offset field settings $\vec{E}_{dcoH}$. Every data point corresponds to the correlation evaluated on a data sample of 8 s length. In (a) the correlation is plotted in the complex plane. (b) shows the amplitude and (c) the phase of each measured correlation vs the effective offset field, which is the difference between $\vec{E}_{dcoH}$ and its optimally compensated value. (d) shows c_{rot} (blue), the component of correlation along the asymptotic phase ($\sim \pi/4$), and its orthogonal complement c_{orth} (red).

offset field. These two components are directly linked to the micromotion parameters in phase (c_{rot}), or out or phase (c_{orth}) with the driving RF respectively. The optimal value for the electric offset field is found for $c_{rot} = 0$, while c_{orth} characterizes the RF-phase shift between opposing electrode voltages.

3.2.6 Continuous Compensation Method

For long experimental runs, usually extending over several days, we want the micromotion to be controlled at all time. Within such time-scales, external offset fields drift significantly. Therefore, the correlation measurement and the compensation with $\vec{E}_{dcoV}$ and $\vec{E}_{dcoH}$ need to be conducted continuously. We do this in the following automized way. Photon counter data is taken for random electric offset fields within a small region around the optimal value during the MOT loading phase within each experimental cycle. The asymptotic phase is determined

with a weighted floating average with exponential decay. Each measured correlation point is therefore weighted with its amplitude, because points in Fig. 3.6a further away from the origin contain more information on the asymptotic phase than points close to the origin. The correlation coefficients $c_{c,real}$ and $c_{s,real}$ are stored in two cyclic lists with their error initially set by photon shot noise. These errors are thereafter increased by a certain percentage whenever a new entry is added to the list. This accounts for the fact that data from far in the past can only be mapped to the present situation with increased uncertainty. Then a new list with c_{rot} is calculated from the two cyclic lists and the current asymptotic phase. And finally, a weighted linear fit is used on c_{rot} vs $\vec{E}_{dcoH}$ to find the optimally compensated value for $\vec{E}_{dcoH}$. Fig. 3.7a shows c_{rot} and c_{orth} vs $\vec{E}_{dcoH}$ of micromotion measured over a period of four days. The optimally compensated value for $\vec{E}_{dcoH}$ drifted by 4 V/m, which is displayed in Fig. 3.7b. A single measurement of 8 s length yields a compensation accuracy of about 0.3 V/m, when used in an a posteriori analysis. These data can be used to evaluate the accuracy of our continuous compensation method described above, which is on the order of 0.1 V/m.

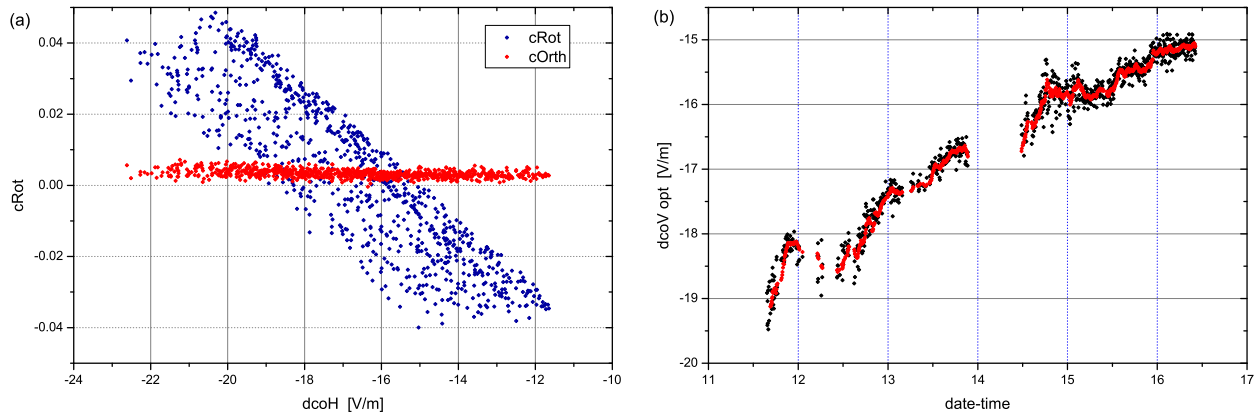

Figure 3.7: (a) displays the same data as in Fig. 3.6d but plotted against the real $\vec{E}_{dcoH}$. Due to drifts during the four days of data acquisition the c_{rot} (blue) are not on a single line anymore. c_{orth} (red) remains qualitatively unchanged. The drifts are shown in (b), where the optimal value for $\vec{E}_{dcoH}$ is calculated from a single measurement (black) or by the automized optimization procedure (red).

3.2.7 Additional Forces Affecting Micromotion

The micromotion compensation is mainly performed to produce optimal conditions during interactions between the ion and the neutral atoms. The correlation is however measured in a different environment than the interaction with the neutral atoms. Magnetic coils run with different currents, optical dipole traps for the neutral atoms might be switched on and there is no cooling laser light for the ion. All these changes can introduce additional forces on the ion, they displace the ion and make corrections to the compensation fields necessary.

Optical dipole forces from any laser are all very small, corresponding to electric fields of less than 0.001 V/m, and can be neglected. The spontaneous force of the cooling laser however corresponds to a field of 0.4 V/m and needs to be considered when approaching that level of compensation. Additional electric fields from voltage gradients across two closely located magnetic coils are more difficult to quantify. Reasonable numbers are a voltage drop of 1 V over a coil separation of 5 cm, yielding a field of 20 V/m. However, the stainless steel vacuum chamber and the electrodes of the ion trap should strongly shield this field from the ion.

3.3 Ion Trap Frequency Measurement

Two different methods have been used to characterize the trap frequencies in our setup. The first method uses the positions of ions in a Coulomb crystal. For two trapped ions, for example, the separation d_{is} is linked to the longitudinal trapping frequency ω_z with $\frac{Q^2}{4\pi\epsilon_0 d_{is}^2} = m_i\omega_z^2 d_{is}/2$. In the case of many ions aligned in a zig-zag shaped Coulomb crystal, information on the radial trapping frequency is contained in the displacement of ions away from the trap symmetry axis. The biggest error source in this way of determining trapping frequencies lies in the calibration of the imaging magnification, which links real ion separations such as d_{is} to the ion positions seen on the CCD image. The second method to measure trapping frequencies uses resonant excitation of the three oscillation modes. It gives more accurate results and will be explained later in this section. The combination of the two methods is used to fully characterize the harmonic trapping potential. While the resonant excitation gives accurate values of the trapping frequencies, the image of Coulomb crystals provides information of the orientation of the trapping axis. Also, the best calibration of the imaging magnification is achieved by combining the measured separation d_{is} with the spectroscopically determined ω_z.

The motion of the ion can be excited by applying a modulated electric field [61]. When the modulation frequency coincides with an ion trapping frequency, the energy of the ion is resonantly enhanced and due to Doppler shift, and the ion moving out of the laser beam and the field of view of the PMT, the fluorescence signal will decrease. The problem with this method is that the ion is easily lost as its energy exceeds the trap depth. This is because the only damping force, the laser cooling, becomes ineffective as the energy of the ion increases.

Instead, we are using the spontaneous light force to excite the ion [61]. To this end, the light is modulated by quickly switching it on and off with an AOM triggered by a DDS[1]. The switching frequency is typically swept over a frequency range where all the trapping frequencies are expected within. The advantage of using the spontaneous light force to resonantly excite the ion's motion is that the excitation force decreases with the fluorescence as the energy of the ion increases. This automatically limits the energy an ion can acquire and trap losses due to the ion trap frequency measurement have not been observed.

A typical fluorescence signal recorded while the cooling light is modulated is shown in

[1] This method has been implemented together with Lothar Ratschbacher [88].

Fig. 3.8. The modulation frequency is swept from 35 kHz to 195 kHz. Three clear dips can be seen at the trapping frequencies. The dips at 135 kHz and 169 kHz correspond to radial excitations, the third dip appears at $\omega_z = 2\pi\,50\,\text{kHz}$. It is significantly broader than the other two and the width changes if the excitation frequency is scanned downwards instead. This behaviour is well described by a Duffing-oscillator [93]. The required trap anharmonicity is very likely to occur along the trap symmetry axis, as the DC-electric field created by voltages applied to the end-caps is shielded by the RF-electrodes and because the excited ion trajectory extends over more than 100 μm. The broadening has to be taken into account carefully when evaluating ω_z from the fluorescence data. Additional care has to be taken to account for the asymmetric broadening, as the anharmonicity is not constant. We have observed it changing when other electric offset fields drift.

We model our trap geometry with a potential consisting of three terms. The weakest trapping axis is assumed to be fixed to the trap symmetry axis. The first term considered is the pseudopotential generated by the RF-quadrupole and is of the form $U_{RF} = \frac{m}{2}\omega_p^2(x^2 + y^2)$. The second term describes the longitudinal confinement induced by the end-cap voltages, but including an asymmetry in the radial deconfinement, $U_{DC} = \frac{m}{2}\left(\omega_z^2 z^2 - \omega_h^2 x^2 - \omega_v^2 y^2\right)$, with $\omega_z^2 - \omega_h^2 - \omega_v^2 = 0$ to fulfill $\Delta U_{DC} = 0$. The third contribution describes a DC-offset on the quadrupole field ($dcoQ$) with the same orientation as the RF-field, which can be tuned by applying additional DC-voltages to the RF-electrodes. Its potential is of the form $U_{dcoQ} = c_{geom,Q}\,Q(dcoQ - dcoQ_0)\cdot(2xy)$. The offset $dcoQ_0$ and the asymmetry in U_{DC} are a result of static charges on electrode surfaces or ceramics and they drift in time. $c_{geom,Q}$ is the geometric efficiency of the quadrupole field.

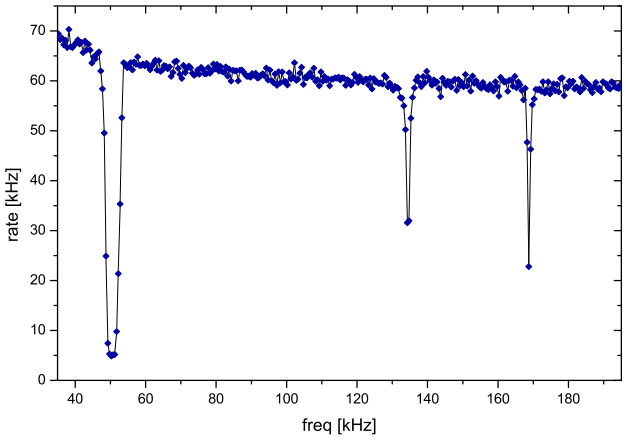

Figure 3.8: Ion fluorescence signal while the laser is modulated with a sweeping frequency. A dip appears whenever the modulation frequency coincides with a trapping frequency. The shown data is an average of five realizations, each one acquired within 4.8 s.

A series of measurements of the three trapping frequencies for various $dcoQ$ determines the full harmonic trap geometry. To this end, the data shown in Fig. 3.9 are fitted with the frequencies resulting from the model above. The fitting parameters are ω_p, ω_z, ω_h, $dcoQ_0$ and $c_{geom,Q}$. At the point of minimal splitting between the radial trapping frequencies, $dcoQ = dcoQ_0$, the lower trapping frequency is associated to the horizontal axis. This is found by looking at a Coulomb crystal in that trap configuration. The camera images along the vertical axis and the zig-zag shape is most pronounced at $dcoQ = dcoQ_0$. If the lower

radial trapping frequency were in the vertical direction, the zig-zag shape would be aligned along the line of sight and not be visible on the camera. The data presented in Fig. 3.9 yield $\omega_p = 2\pi\,157\,\mathrm{kHz}$ and $\omega_z = 2\pi\,49\,\mathrm{kHz}$, which both depend on the RF-power and the end-cap voltages. Offset fields from localized static charges at the time of the measurement are taken into account with $\omega_h = 2\pi\,25\,\mathrm{kHz}$ and $dcoQ_0 = 282\,\mathrm{kV/m^2}$. The fitting result for the geometric prefactor $c_{geom,Q} = 0.64$[2] is a constant. Together with ω_p it can be used to calculate $V_0 = 230\,\mathrm{V}$, the actual RF-voltage amplitude between the trap electrodes.

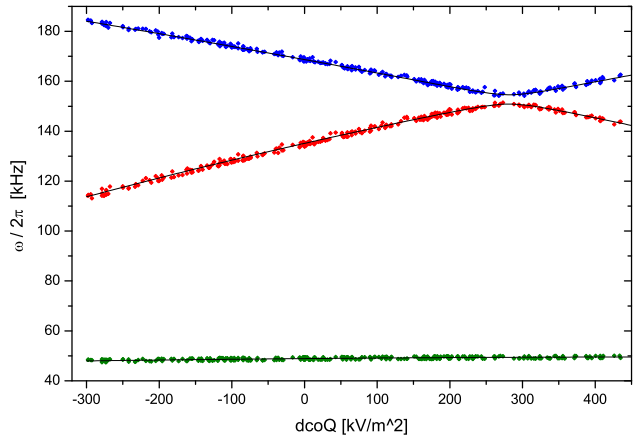

Figure 3.9: Ion trap frequencies for various *dcoQ*. The two radial frequencies (blue and red) and the axial frequency (green) are fitted with a three component potential model (black lines).

3.4 Ion Temperature Measurement

To determine the motional energy of an ion we measure the change of its fluorescence rate due to the Doppler shift. The higher the ion's average velocity, the lower is the expected fluorescence. The motional energy of the ion will be affected by the scattered photons and typically reach Doppler temperature within $\sim 1\,\mathrm{ms}$. For an initially hot ion the observed increase of fluorescence rate reflects the dynamics of Doppler cooling. This increase in fluorescence, and how to attribute an ion temperature to it, is described in [95]. The technique has originally been employed to determine heating rates of ion traps [96]. We use it to measure the mean ion energy after the ion has interacted with the ultracold atoms. The method and the data evaluation procedure are described in the following.

The measurement of the fluorescence is typically taken directly after the release of the neutral atoms from their trap, to be insensitive to the intrinsic ion trap heating. The intensity of the fluorescence laser at 370 nm is always regulated with a PID-controller. However, after quickly switching the light on it takes about 15 ms for it to stabilize. Therefore, the fluorescence laser is switched on 20 ms before the repumper at 935 nm. The repumper is enabled quickly with the means of an AOM, using the same trigger signal to notify the TDC about the start of the measurement. The registered fluorescence photons are subsequently binned with a $5\,\mu\mathrm{s}$ spacing. The sensitivity of the measurement can be increased by setting the detuning of the fluorescence laser closer to the resonance. As this will render Doppler cooling less efficient,

[2] This number for $c_{geom,Q}$ should be compared with 0.82 from the finite element electric field calculation [94]. The discrepancy might be caused by differences in the trap dimensions between the finite element model and the real trap setup.

allowing the ion to remain longer at an increased energy, the signal of decreased fluorescence can be detected for a longer time. However, the sensitivity to the accurate setting of the laser detuning increases as well. The automatic adjustment of the detuning, described in section 2.3.3, is therefore crucial for consistent data acquisition. In our setup, the ideal value for the detuning, maximizing the measurements sensitivity while keeping the systematic error low, is found at $-\Gamma/4$.

The theoretical model [95] describing the fluorescence, treats the motion of the ion in a one dimensional harmonic oscillator and neglects micromotion. Stochastic heating by photon recoil is also ignored, as it only becomes relevant near the cooling limit where the change to the observed fluorescence rate is insignificant. A first assumption relating to the experimental parameters is that the excited state population is always close to its equilibrium value

$$P_{|e\rangle}(v_z) = \frac{I/(2I_{sat})}{1 + I/I_{sat} + (2(\delta_L - k_z v_z)/\Gamma)^2} \,. \tag{3.6}$$

This is well justified if v_z changes slowly compared to the excited state decay rate Γ. In our setup this condition is fulfilled as the trapping frequencies are at least two orders of magnitude below Γ. The spontaneous force $F_z(v_z) = \hbar k_z \Gamma P_{|e\rangle}(v_z)$ leads to the cooling rate $v_z F_z$, which is averaged over one oscillation cycle. Here, to justify the average, a small change in the energy of the ion during one oscillation period is required. There is one order of magnitude between the timescale for Doppler cooling and the trap oscillation period in our experiments. Given a set of laser detuning, saturation parameter and initial ion energy, the evolution of this energy in time is calculated by numerically integrating the cooling rate. The evolution of the fluorescence rate follows directly. As only few photons are detected within the relevant time of $\sim 1\,\mathrm{ms}$ in a single measurement, it needs to be repeated many times before the averaged fluorescence rate yields conclusive information on the initial energy. This averaged fluorescence rate is predicted by assuming a thermal distribution of initial energies. Although we know from simulations (see chapter 5), that the distribution of ion energies after interacting with the cold neutral atoms can be non-thermal, the thermal assumption still gives a valid link between the averaged fluorescence rate and the mean ion energy.

The repeatedly measured and averaged fluorescence rate is fitted by the model with a least square method, shown in Fig. 3.10a. To this end, expected fluorescence rate curves are previously calculated for a number of different mean ion energies. The three curves with the smallest sum of squared differences to the measured data are then selected and a polynomial of second order is used to interpolate the sum of squared differences over the energy range of the selection. The best fit for the mean energy of the data is found at the minimum of the interpolating polynomial. This fitting procedure uses the energy as the only free parameter and requires prior knowledge of the photon counting efficiency ϵ_{PMT} of the detection system, or a normalization of the fluorescence rate on its converged value.

The fluctuation on the measured fluorescence rate is limited by photon shot noise. A

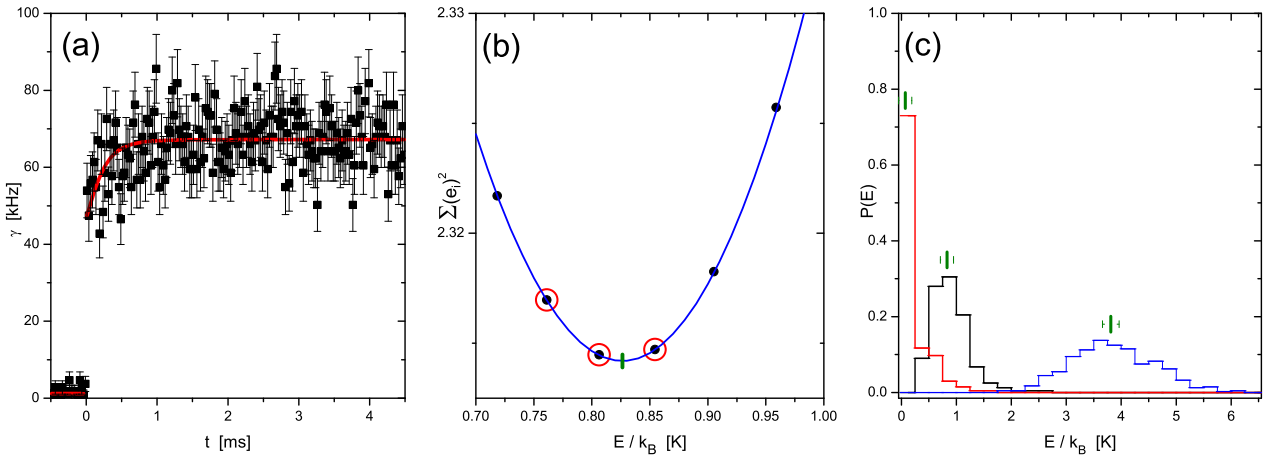

Figure 3.10: (a) depicts a typical sample of averaged fluorescence count rate during Doppler cooling. The red line is a fit using the model from [95]. The sum of squared differences for six assumed initial mean energies are plotted in (b). The three lowest values (red circles) are interpolated with a polynomial of second order (blue line) and its minimum (green marker) is considered the best estimate for the initial mean energy of the ion. (c) shows the probability distribution to measure some initial energy for three different experimental configurations. The probability distribution is generated using a bootstrapping method. The resulting energy from the red measurement is compatible with zero. The green markers depict the fit result and the error calculated from linearly propagating the photon shot noise. This error is much smaller than the width of the probability distribution because it neglects the effect of the small number of measurements over which the fluorescence rate is averaged. This number is 40 in the presented data. Other measurements with averaging over more than 200 repetitions show better agreement between the linear error estimate and the width of the probability distribution.

formula describing how to propagate this noise onto the fitted mean energy $\bar{E}$ is given in [95]

$$1/\sigma(\bar{E})^2 = \sum_i \left(\frac{\partial n_i}{\partial \bar{E}}\right)^2 /\sigma_i^2 \ , \tag{3.7}$$

with n_i being the predicted number of photons counted and σ_i the shot noise in the bin at time i. The formula is well justified if a variation on any n_i within a range of σ_i creates a linear response on $\bar{E}$. This condition is not strictly fulfilled, especially for small $\bar{E}$ close to the detection limit. Additional errors are caused by small sample sizes of the thermal average and are not included in (3.7). For measurements with averages over less than ~ 100 realizations an underestimation of the error is therefore expected. By using a bootstrapping method [97] both the effects of insufficient sample size and nonlinear error response can be investigated, shown in Fig. 3.10c.

The initial simplifications of the model, the treatment in only one dimension and neglecting the micromotion, lead to an additional overestimation of $\bar{E}$. Modeling the system in three dimensions involves many more experimental parameters which need to be accurately known.

The orientation of the three main trap axis relative to the cooling laser beam and the exact trapping frequencies are relevant. As the single laser essentially cools the ion merely along one dimension, the cooling efficiency is limited by the rate of motional energy transfer from the other two dimensions. This transfer rate can be small, for instance for two near degenerate radial trap frequencies, resulting in a lower measured fluorescence rate for an extended time. Hence the one dimensional model overestimates the mean energy. In conclusion, the absolute value of the fitted energy has to be interpreted with care. However, to detect relative energy differences, the method provides reliable results.

3.5 Calibration of Electric Offset Fields

The simplest approach to estimate the electric fields which are generated by the electrodes is to just take the ratio of applied voltage difference and electrode distance. This is how we defined the technical parameters for the three DC-offset fields, $\vec{E}_{dcoH}$ for the horizontal, $\vec{E}_{dcoV}$ for the vertical and $\vec{E}_{dcoL}$ for the longitudinal trap axis. The DC-offset quadrupole field, using the same geometric configuration as the RF-trapping field, is attributed to the technical parameter *dcoQ* in a similar way, as half the voltage difference between electrode pairs divided by the square of the distance from the electrodes to the trap centre. The real physical values of these electric fields all differ from the above technical definition by some constant factor, defined by the trap electrodes' geometry. In principal all the geometric factors can be obtained from finite element field simulations. By this method the geometric attenuation for $\vec{E}_{dcoH}$ and $\vec{E}_{dcoV}$ is expected to be 0.71 [94]. This number is mainly used in the calculation of the real amplitude of excess micromotion for any setting of $\vec{E}_{dcoH}$ and $\vec{E}_{dcoV}$. However, the error in calculating the physical fields is rather large and systematic, relating mainly to simplifications made in the simulation model and to inaccuracies in the manufacturing process of the real ion trap. The remaining two fields are calibrated by measuring the effect they have on a trapped ion. The calibration of *dcoQ* is done by measuring trap frequencies, explained in section 3.3. The physical value of $\vec{E}_{dcoL}$ is measured by observing a single ion's displacement with the CCD-camera. The magnification of the camera, or the corresponding size of one pixel can be determined by the distance of ions in a Coulomb crystal, if the longitudinal trap frequency is known. The resulting geometric attenuation of the technical field $\vec{E}_{dcoL}$ is 0.01245(27). The error here is dominated by the measurement of the ion displacement to an accuracy of 0.2 pixels and can be improved, if required, by repeating the measurement many times. The geometric factor is rather small due to the strong shielding of the longitudinal field by the radial electrodes.

Other than $\vec{E}_{dcoH}$ and $\vec{E}_{dcoV}$, which are tuned to minimize excess micromotion, $\vec{E}_{dcoL}$ can be set to a range of different values, changing the position of the ion but without affecting its micromotion or confinement. Still, a stable position of the ion is required to reproducibly overlap it with the neutral atoms during prolonged measurements. Static charges, which

slowly accumulate on insulating parts of the setup therefore make electric field compensation a necessity, also on the $\vec{E}_{dcoL}$ value. We define the best compensated value of $\vec{E}_{dcoL}$ as the field where the position of the ion is unchanged when symmetrically lowering the longitudinal confinement. The automatic alignment sequence requires four position measurements of the single ion obtained from four CCD images. During their acquisition, two different $\vec{E}_{dcoL}$ settings and two different settings for the longitudinal confinement are applied in the four possible combinations. For the same value of $\vec{E}_{dcoL}$, the change in the confinement leads to a displacement of the ion. This displacement is a linear function of $\vec{E}_{dcoL}$. The two measured displacements for the different values of $\vec{E}_{dcoL}$ are connected with a line and the compensated value of $\vec{E}_{dcoL}$ is found where this line intersects with the displacement equal to zero. There are other methods to adjust $\vec{E}_{dcoL}$, such as optimizing the position of the ion on the camera, however the above described solution proved to be the most stable procedure.

3.6 Measuring Properties of the Neutral Cloud

As a very general statement, information retrieval in a single experimental cycle can be much more efficient from the neutral atoms than from a single ion, simply due to the larger number of atoms. As an example, the measurement of the mean energy of an ion requires a large number of repetitions of the same experiment, and the same is true when measuring an ion loss probability as only one bit of information, loss or no loss, can be retrieved per repetition. In contrast, the neutral atoms can provide information on the cloud temperature, its position, density, and structure in a single experimental repetition. In our setup, all this information is acquired through the standard technique of absorption imaging. Here follows a short explanation of the imaging technique and a description of how we obtain physical measures from the images.

Absorption imaging is essentially a measurement of column density. Resonant or near resonant light is sent in a collimated beam onto the atoms which scatter the light and create a shadow in the beam. The shadow is then imaged with a telescope onto a CCD-camera. Each pixel of the camera measures the attenuation $q(x, y)$ of the imaging light for a specific point in the atom cloud. The attenuation is given by

$$q(x, y) = \exp\left(-\sigma(\omega_L) \int_{-\infty}^{\infty} \rho(x, y, z) \mathrm{d}z\right) , \tag{3.8}$$

with $\rho(x, y, z)$ being the atom density and $\sigma(\omega_L)$ the optical absorption cross-section for the laser frequency ω_L. The integral is referred to as the column density and $\sigma(\omega_L)$ times the column density as the optical density.

The attenuation $q(x, y)$ is typically determined with the help of two additional images, one taken completely in the dark to account for technical offsets, and another one with the same amount of light as the actual measurement, but without atoms to account for non-uniform

illumination. The ratio between the measured light intensity in the image with atoms and the bright image without atoms corresponds to $q(x, y)$. The column density can then be calculated by inverting Eqn. (3.8) with the knowledge of $\sigma(\omega_L)$. For a two-level system $\sigma(\omega_L)$ is given by

$$\sigma(\omega_L) = \frac{\hbar\omega_L}{I_{sat}} \frac{\Gamma/2}{1 + I/I_{sat} + (2\Delta/\Gamma)^2} , \tag{3.9}$$

and can be tuned by changing the light intensity I or the detuning Δ. Due to the CCD-camera's intensity resolution, photon shot-noise, and additional technical noise, the accuracy of the measurement of $q(x, y)$ is limited. The best signal to noise on the column density is achieved for optical densities around one. For measuring the high densities of a typical ultracold cloud of ^{87}Rb a large detuning Δ needs to be chosen.

Uncertainties and fluctuations on the value of the laser detuning introduce systematic errors in the determination of the atom column density. To minimize these errors, an accurate calibration of the laser parameters is required. The laser frequency can be tuned with an AOM, driven by the signal of a DDS which ensures high reproducibility. For the calibration, a series of images of identical atomic clouds is taken at different laser detunings, and a Lorentzian fit to the optical density retrieves the laser parameters I/I_{sat} and Δ.

In situ imaging of the neutral atom cloud is useful for alignment purposes, as the position of the cloud is easily detected (see also next section and Fig. 3.12b). However, due to the imaging resolution being limited by diffraction, only little information about the structure of the density distribution can be obtained. In most experiments we image the atoms after a ballistic expansion of a few milliseconds. These time-of-flight images are most useful to determine the cloud's initial energy, because the position of an atom after ballistic expansion depends on its initial momentum. In a thermal ensemble the momentum is normally distributed, so the measured column density in time-of-flight image can be fitted with a Gaussian, with its width relating to the temperature of the trapped gas. The number of atoms is obtained by integrating the density over the full image or from the amplitude of the fitted Gaussian.

For the investigation of the atom-ion interaction in our system, the neutral atom number and temperature measurements have proved of value. When conducting measurements with a thermal neutral cloud, the typically observed standard deviations are on the order of 15% on the number of atoms and 6% on the temperature respectively. These numbers can however vary significantly and depend on the chosen experimental parameters.

When imaging a partially condensed cloud in time-of-flight, the condensate fraction can be distinguished from the thermal part by its slower and anisotropic expansion. Applying a bi-modal fit, consisting of a Gaussian representing the thermal, and a Thomas-Fermi profile for the condensate part, yields the additional measure of the condensate fraction or the number of condensed atoms respectively. Fig. 3.11 shows the measured column densities for three different condensate fractions.

To characterize the magnetic or the optical dipole trap for the neutral atoms, the mea-

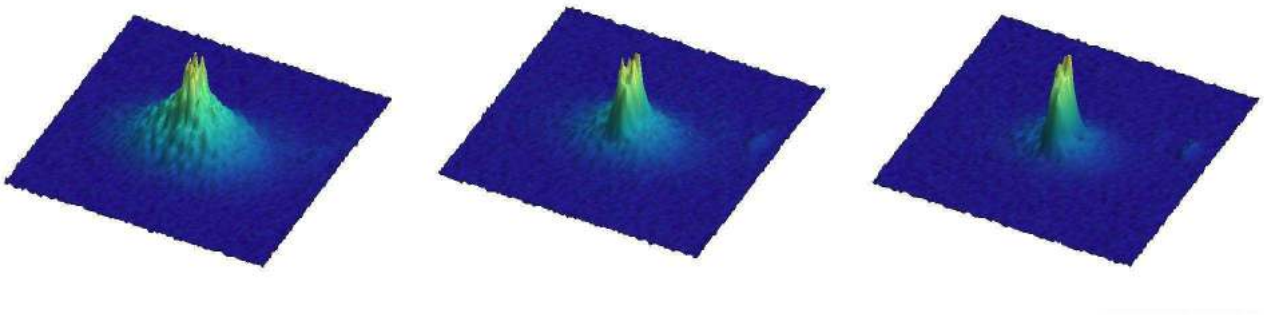

Figure 3.11: The formation of some of our first Bose-Einstein Condensates on April 15th 2008. From left to right, as evaporation time is prolonged, the thermal contribution diminishes and the sharp condensate peak becomes more accentuated. Note the elongation of the condensate which is perpendicular to the elongation of the thermal part. After longer time of flight the thermal part tends to assume a spherically symmetric shape whereas the BEC fraction's elongation gets more pronounced.

surement of trap frequencies makes use of the detected position of the cloud in time-of-flight. The gas is set in motion by first displacing it from the trap centre with a magnetic offset field, to then rapidly turn off the field, setting the atoms into an oscillatory motion. After a preset time the trapping confinement is switched off to start the ballistic expansion. The oscillation period, and hence the trapping frequency, is obtained from a harmonic fit to the cloud's position for different times of oscillation. Two measurements of such type are displayed in Fig. 3.12a.

3.7 Independence of Neutral and Ion Confinement Potentials

One of the motivations to combine trapped ions with ultracold neutral atomic gases is that they are subject to different external forces, allowing to control the two independently. Basically, the ions are trapped by electric fields and the neutral atoms by magnetic fields or dipole laser traps. This section discusses the limitations of that independence.

Considering the effects of the magnetic fields on the ion, the ratio between the cyclotron frequency QB/m and the ion trapping frequency ω is the relevant scale $r_B = \frac{QB}{m\omega}$. For typical trapping frequencies of several tens of kHz and magnetic fields of a few Gauss the scale r_B is below 10^{-3}. For example, a static magnetic field will perturb the trajectory of the trapped ion by means of the Lorentz force. If the ion initially oscillates along a single radial axis, then after one oscillation period this axis is rotated by an angle approximately expressed by r_B. A different effect relates to switching magnetic fields on or off. The induced electric field, given

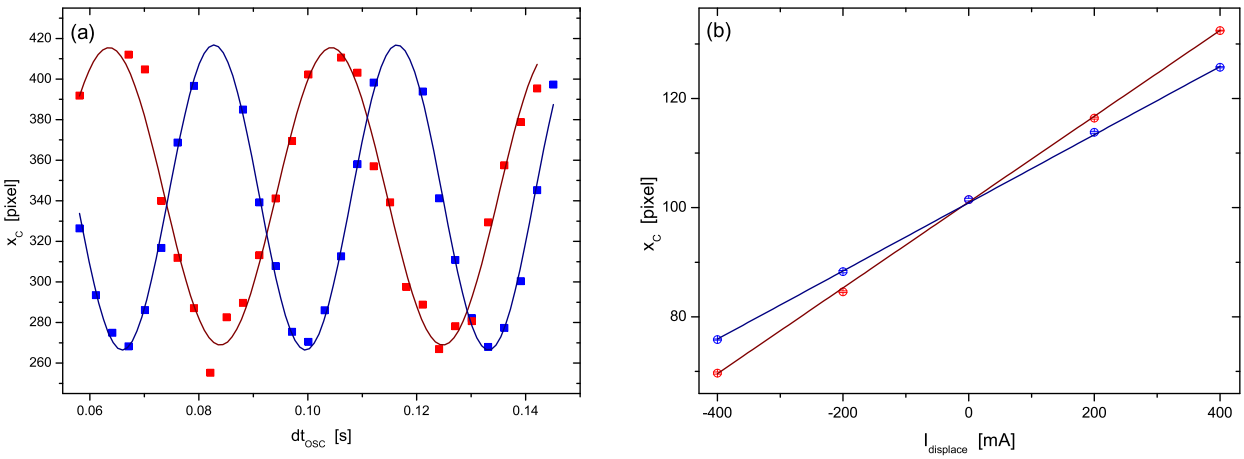

Figure 3.12: (a) Oscillations of the neutral atom cloud in the identical magnetic trap, but once with electric RF-quadrupole field enabled (red) and once disabled (blue). The deconfinement reduces the trap frequency from 29.7 Hz to 24.5 Hz (b) The centre x_c of the magnetically trapped neutral cloud is displaced by a magnetic offset field driven by a current $I_{displace}$. The displacement is larger when the RF-quadrupole field is enabled due to its deconfining effect. There is no additional displacement when the neutral atoms are centred on the RF-quadrupole field ($I_{displace} = 0$).

by the Maxwell-Faraday equation $\nabla \times E = \frac{\partial B}{\partial t}$, can change the energy of the ion. In the case where the ion orbits on a circular trajectory around the direction of the magnetic field B, turning off the magnetic field leads to a relative change in the ion's energy of r_B. The energy is increased or decreased depending on the direction of the orbit. As the circular orbit is the extreme case, where induction gives the strongest effect, the relative change in energy is limited by r_B ($\Delta E/E \leq r_B$). In our experiments these magnetic effects on the ion can be neglected because r_B is small.

Through the Zeeman effect, the magnetic trap creates the same potential on a $^{174}Yb^+$, $J = 1/2$, $m_J = 1/2$ ion as on a ^{87}Rb, $F = 2$, $m_F = 2$ atom. Due to the much stronger electric confinement of the ion, this can again be neglected. The trapping potential for the ion experiences a relative change of less than 10^{-6}. Very similarly, the optical dipole trap for the neutral atoms affects the ion as well, but only adds a negligible amount to the electric ion trapping potential.

The neutral atoms, on the other hand, experience the electric fields in a significant way and a few effects have been quantified. The DC-polarizability of ^{87}Rb, given by the coefficient [85] $\alpha_0 = h \cdot 0.0794(16)\,\mathrm{Hz}/(\mathrm{V/cm}^2)$, leads to an induced dipole when the atom is subjected to an electric field E. The dipole interacts with the field itself, creating the induced dipole potential $U_{id} = -\frac{\alpha_0}{2}|E|^2$. The ^{87}Rb atom is attracted to electric field maxima. Note that this is the same effect responsible for the attractive interaction between the ion and the neutral atom (cf. section 4.1). Here, the interaction with the ion trapping field is considered. The linear RF-quadrupole field has its minima along the symmetry axis of the ion trap, leading to a radial

deconfinement for the neutral atoms. The magnitude of this deconfinement is calculated by averaging $|E|^2$ over one RF period and yields

$$U_{dec} = -\frac{\alpha_0 \, {c_{geom,Q}}^2 \, {V_0}^2}{4R^2} \, r^2 = -\frac{m_{Rb}}{2}\omega_{dec}^2 r^2 \; . \tag{3.10}$$

The deconfinement lowers the trapping frequency of the neutral atoms in the magnetic or the optical dipole trap by ω_{dec}, in quadrature. For typical operating parameters of our ion trap, ω_{dec} is on the order of $2\pi\,15\,\mathrm{Hz}$. Fig. 3.12a shows a measurement of the trap frequency in the magnetic trap and how it reduces when the RF-field of the ion trap is enabled. The deconfinement is independent of the alignment between the RF-electric field and the neutral trap. The minimum of the combined potential however is shifted away from the centre of the neutral trap depending on the alignment. This shift can be measured by displacing the centre of the magnetic trap with an additional magnetic field. Enabling the RF-electric field leads to an additional displacement if the trap centres are not aligned, shown in Fig. 3.12b. Although this measurement is not very precise, it can be helpful as a first step of alignment or to map the electric field without a trapped ion.

The deconfinement also leads to an increased expansion of the neutral atom cloud in time of flight which should be considered for an accurate determination of the atoms' temperature. In the absorption image, the width of the cloud is expected to be increased by $\sim 5\%$ in the radial direction.

3.8 Alignment of the Neutral Atoms with the Single Ion

The independent control over the ion trap and the neutral atom trap introduces the tunable parameter of the relative position between the two systems. The virtue of the additional control comes at the cost that it needs to be calibrated, meaning the two systems need to be aligned.

The initial alignment is easily achieved by orienting the atoms relative to the ion trap electrodes, which can be seen on the CCD-images. Then one starts to search for an atom loss signal caused by the ion, which can subsequently be maximized by adjusting the neutral trap position. Another plan has been to align the optical dipole trap laser to the ion first, and a dipole trap laser has therefore been built at a wavelength identical to the Yb^+ repump transition at 935 nm. However, due to scarce laser power and other means of alignment, the dipole laser has now been replaced by a commercial system at a wavelength of 1064 nm.

The alignment on the atom loss signal works for atoms trapped in both the magnetic or the optical dipole trap. This is because there are always collisions between the ion and neutral atoms with energy transfers higher than the neutral trap depth. The atom loss rate can be assumed to be proportional to the local neutral atom density at the position of the ion. More about the collision effect will be discussed in the next two chapters.

Coarse alignment is achieved with a several micro-Kelvin warm neutral cloud in the magnetic trap. To refine the alignment, the atoms can first be cooled, then loaded into the optical dipole trap and the most precise alignment is achieved by measuring the losses on a BEC, because the spatial extend of the density distribution is the smallest. The magnetic trap centre is shifted by applying magnetic offset fields (used also for the measurement in Fig. 3.12b). The field values are controlled from the computer and are very reproducible. The position of the optical trap can be aligned by two different means. First, the lens focusing the dipole laser to the atoms is mounted on a translation stage with positioning accuracy of $\sim 1\,\mu$m. It has to be adjusted manually and suffers from hysteresis effects, impeding the alignment process. The second and more recently implemented means to reposition the optical trap are piezo-actuated mirrors, which are computer controlled and are operated in a way to minimize hysteresis effects. It is planned for the near future to fully automize the alignment process by using these piezo mirrors in combination with software feedback from the measured number of neutral atoms.

Instead of repositioning the neutral atoms, one could also shift the centre of the ion trap by applying an electric offset field, which works well with $\vec{E}_{dcoL}$ along the longitudinal axis of the ion trap. In the radial direction, the rapid increase of excess micromotion additionally affects the system and is undesired for most of the measurements. However, due to the high reproducibility of changing the radial offset fields, they can be used to check the alignment which potentially suffers from hysteresis effects. Also, this check of alignment can be repeated before and after an alignment sensitive measurement. Two such alignment checks are displayed in Fig. 3.13. They show a relative drift between the optical dipole trap and the ion trap of $\sim 8\,\mu$m within 4 days in the vertical direction, while the observed drift in the horizontal direction is smaller than $2\,\mu$m.

Drifts will ultimately limit the achievable alignment accuracy. Taking the data from Fig. 3.13a as a reference, this achievable accuracy can be derived. We assume the neutral density distribution to be constant and known. The most information about the relative position is obtained by measuring the atom number at the displacement of the steepest slope, which yields approximately a relative change of 10% over a distance of $0.5\,\mu$m. The relative standard deviation on the measured signal is about 20%. This gives a sensitivity of $1\,\mu\text{m}/\sqrt{N_m}$, with N_m being the number of measurements on that axis of displacement. Conducting four measurements on each axis within six hours would compensate for the expected drift of $0.5\,\mu$m. This should leave enough measurement time in between for the main experiment. Increasing the number of alignment measurements improves the accuracy only slightly, in the extreme case of doing only alignment measurements continuously, an alignment accuracy approaching $0.2\,\mu$m could be expected. More effectively, the accuracy could be improved by using a neutral density distribution with a steeper slope. It is expected that the sensitivity could be improved by a factor of four to $0.25\,\mu\text{m}/\sqrt{N_m}$, which could push the achievable alignment accuracy to below $0.2\,\mu$m with only four measurements within six hours.

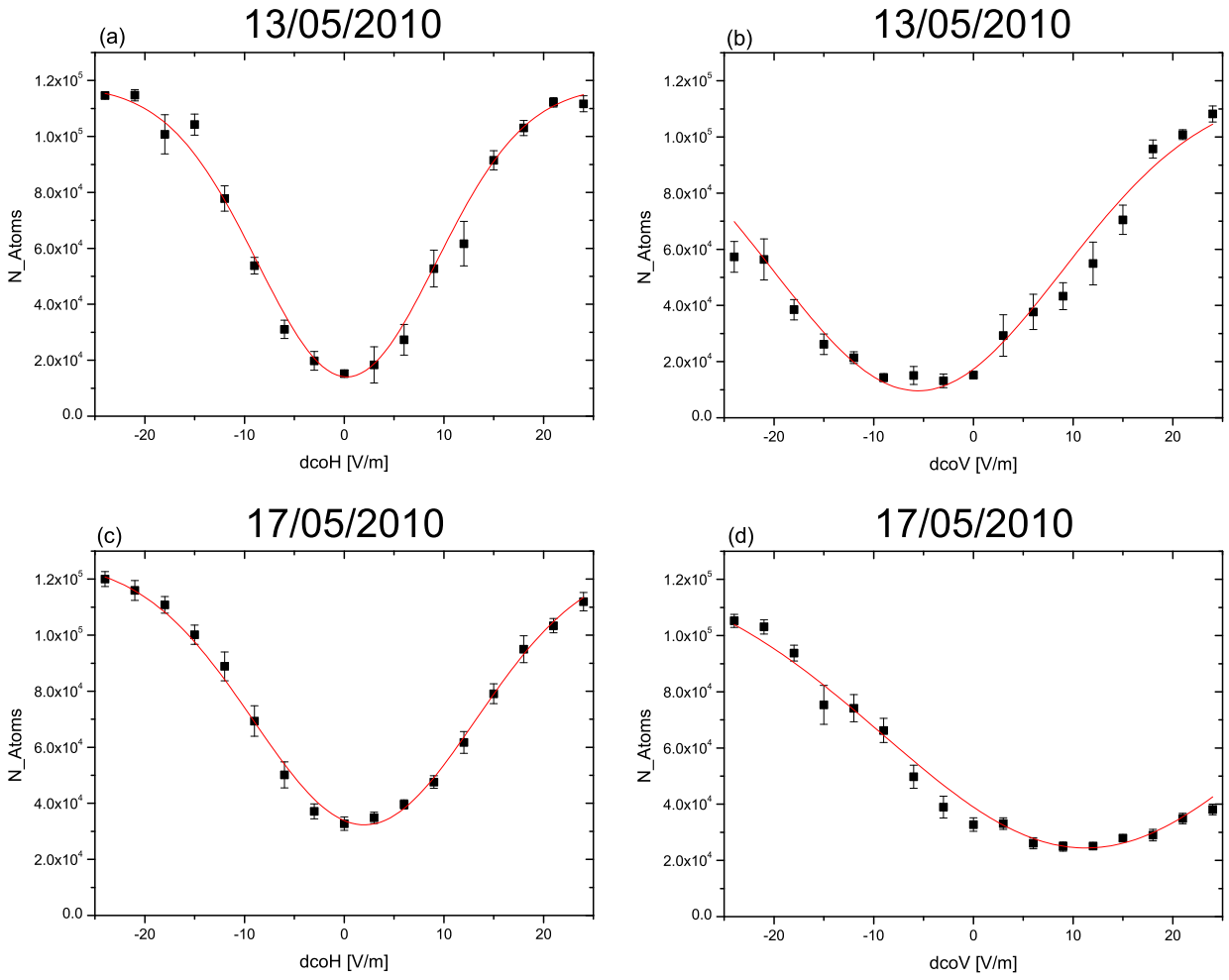

Figure 3.13: The alignment is checked by measuring the neutral atom number affected by a single ion. The position of the ion is displaced with electric offset fields along either the horizontal ($\vec{E}_{dcoH}$) or the vertical direction ($\vec{E}_{dcoV}$). The measurement is repeated four days later to detect drifts of the alignment. The displacement in space is 0.5 μm per V/m offset field. Each shown data-point is an average of about 10 repetitions. The red lines are Gaussian fits, which are used to determine the centre of the neutral cloud.

Chapter 4

Experiments

In this chapter the experimental results from the measurements of the trapped Yb ion, interacting with the ultracold, neutral Rb atoms will be discussed. The first section briefly introduces a model for the interaction potential. A more detailed theoretical description of the interaction process will be given in chapter 5. The next two sections describe the experiments of a single ion immersed in a Bose-Einstein condensate. These experiments have also been reported in [27]. The remaining three sections discuss the experiments we reported about in [28], which investigate the role of micromotion and inelastic collisions.

The following people have additionally been involved in preparing the measurements and during the data acquisition process: Stefan Palzer in the measurements with the Bose-Einstein condensate, Lothar Ratschbacher in the measurements investigating the inelastic processes and Carlo Sias in all the experiments.

4.1 Interaction Potential and Collision Cross-Section

The interaction energy between an ion and a neutral atom is dominated by the induced dipole effect, analogous to the one described in section 3.7. The electric Coulomb field of the ion's charge ($|\vec{E}| = Q/(4\pi\epsilon_0 R^2)$) induces a dipole moment $\alpha_0|\vec{E}|$ in the neutral atom. Q is the charge of the ion, R the distance between the ion and the neutral atom, and α_0 the polarizability of the neutral atom. The induced dipole moment interacts with the Coulomb field itself. The resulting interaction potential is given by

$$V(R) = -\frac{C_4}{2\,R^4}\ , \tag{4.1}$$

with $C_4 = \alpha_0 Q^2/(4\pi\epsilon_0)^2$. This potential is long-ranged with a characteristic length scale of $r^* = \sqrt{\mu C_4/\hbar^2}$. In our system of ^{87}Rb and ^{174}Yb$^+$ it is $r^* = 307\,\mathrm{nm}$ and the s-wave scattering regime ($E \lesssim \frac{\hbar^2}{2\mu r^{*2}}$) is only at submicro-Kelvin temperatures [45, 51].

A classically defined cross-section, first introduced by Langevin in 1905 [47], predicts an energy independent collision rate. It considers only scattering from an assumed hard-core

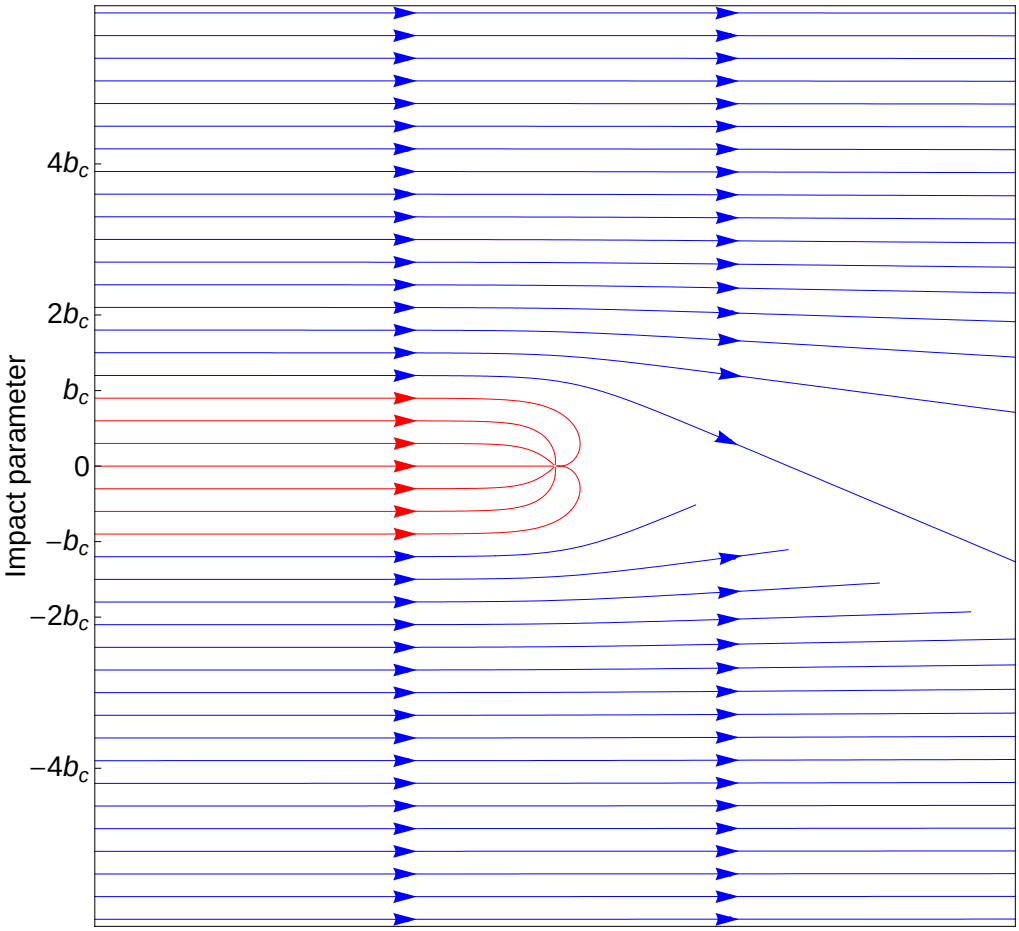

Figure 4.1: Classical trajectories in the C_4 potential [48]. The Langevin cross-section accounts for all trajectories with an impact parameter smaller than $b_c = (2C_4/E_c)^{1/4}$ (red), while forward scattering (blue) is neglected.

repulsion term, with resulting large deflection angles, which are important for the mobility of an ion in a neutral gas, see Fig. 4.1. Cooling of an ion in a cold neutral gas, as an example, should therefore be described by the Langevin cross section $\sigma_L = \pi\sqrt{2C_4/E_c}$, with E_c being the collision energy. The full classical cross-section, including forward scattering, diverges to infinity. The well defined classical cross-section σ_L only includes the close encounter collisions. Nevertheless, in most previous experiments at low collision energies the Langevin cross-section describes all the observed effects well.

In quantum mechanics, the full cross-section is well defined. For the case of many partial waves contributing, it is approximated by [52, 45]

$$\sigma(E_c) = \pi\left(1 + \frac{\pi^2}{16}\right)\left(\frac{\mu C_4^2}{\hbar^2}\right)^{1/3} E_c^{-1/3} \,. \tag{4.2}$$

The main formal difference to the Langevin cross-section is its different energy dependence. Also, it is larger than the Langevin cross-section, as it includes the scattering events with small

deflection angles (forward scattering). Their contribution increases towards higher collision energies E_c. Similar as in the classical description, in the quantum picture the contribution of close-encounter type collisions, where the colliding particles are reflected not by the centrifugal barrier but by the hard-core of the scattering potential, matches the Langevin cross-section σ_L.

The derivation of both these models for the collision cross-section will be treated in more detail in chapter 5. In the here following description of our experiments, we will encounter effects requiring either one, or the other cross-section model, depending on the relevance of forward scattering processes.

4.2 Sympathetic Cooling

The first observed signal indicating interactions between the single ion and the condensate was a loss of neutral atoms. This signal is easily distinguished from background losses, by looking at the difference in number of atoms in the condensate either with or without an ion in the trap. Loosing atoms from the trap means, they must acquire enough energy to escape. As the neutral atoms acquire this energy through collisions with the ion, cooling of the ion is expected. The experiment, in which we observed this sympathetic cooling, will be described in the following.

We prepare a Bose-Einstein-condensate of about 35000 ^{87}Rb atoms in the optical dipole trap of the 935 nm laser, with trapping frequencies of $2\pi\,\{51, 144, 135\}$ Hz and a trap depth of 1 μK. The atoms are in the $F = 2$, $m_F = 2$ hyperfine state and a small magnetic bias field of 1 G is kept on to prevent spin dephasing. A single ^{174}Yb ion is previously loaded, and displaced by 140 μm along the ion trap symmetry axis from the centre of the combined trap. It is displaced during the time from when the neutral atoms enter into the ion trap region to the start of the interaction time. This is necessary to ensure the ion is not precooled by the cold neutral atoms. A thermal fraction of the neutral atoms extends quite far along the horizontal beam of the optical dipole trap, and the ion is therefore also displaced in the radial direction by 15 μm.

To enable the interactions, the ion is moved quickly into the condensate. After a defined time of interaction, the optical trap is disabled and the neutral atoms are released into free fall. Then, the Doppler cooling light for the ion is enabled and the fluorescence recorded, to determine the mean energy of the ion as described in section 3.4. The measurement is repeated for more than 200 times for four different interaction times each. To get a reference value of the ion mean energy without interaction with the condensate, a fifth set of data is taken, where the ion is moved into the trap centre just after the neutral atoms have left. The obtained data are displayed in Fig. 4.2.

We observe a significant decrease of the ion mean energy within 60 ms of interaction. During the first 15 ms of interaction, where most of the ion energy is removed, only little atom

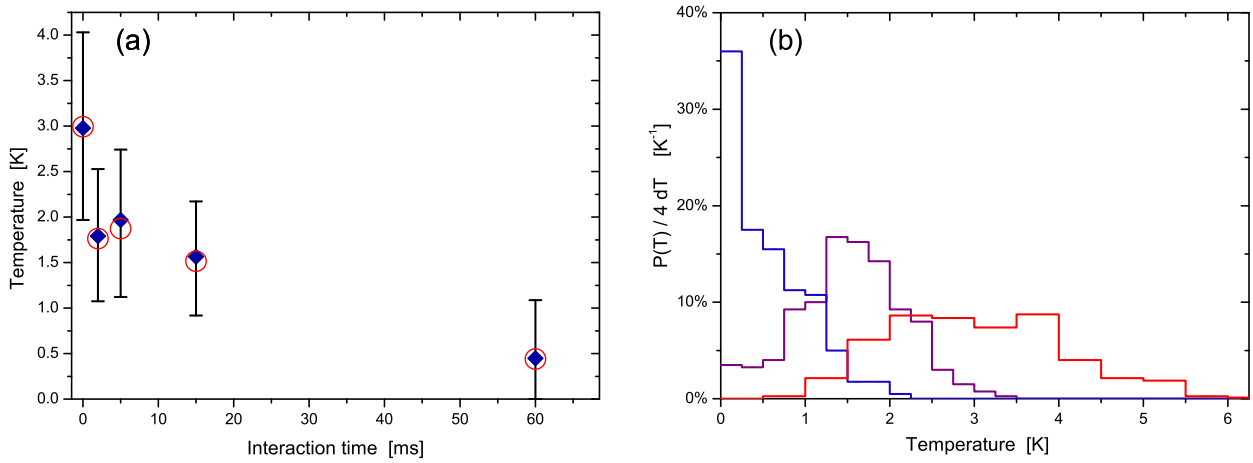

Figure 4.2: (a) displays the ion temperature after different interaction times with the BEC. Each temperature is obtained from a least-chi-square fit (red circles) to fluorescence data sampled over 200 realizations of the experiment each. A bootstrapping analysis provides the distribution of temperature fit results, expected from a sample of the available size, shown in (b) for the interaction times 60 ms (blue) and 15 ms (purple), and no interaction (red). In (a), the median value of the bootstrapping analysis is plotted (blue rhombi) and the percentiles P16 and P84 are used for the error bars, corresponding to a 1-sigma confidence interval.

losses are observed (cf. Fig. 4.3), meaning only few collisions are required to cool the ion. However, the time-scale of several 10 ms is significantly longer than expected for an estimated close-encounter collision rate. We attribute this to the small initial overlap between a 3 K hot ion's trajectory and the much smaller condensate. Initially, only one Langevin type collision is expected within every 2 ms. This explanation is supported by the observation of the low loss of neutral atoms during the cooling process, which will be discussed in the following section.

The fitted ion temperature after 60 ms of interaction is compatible to zero temperature with a likelihood of 25%. This number can be obtained by testing the fitting routine with randomly generated fluorescence counts for an ion with an assumed energy of zero, and with comparable fluorescence counting statistics as in the experimental data. Then, in 25% of the random cases, the fitting result is higher than the 0.44 K which we obtained in our measurement.

One technical limitation of this type of temperature measurement is related to the fact that the energy of the ion can only be determined once the ion is separated from the neutral atoms. The time delay between the end of the interaction time and the start of the fluorescence measurement of the ion energy, is on the order of 1 s. In this period, the ion energy can increase, meaning that the measured temperatures in Fig. 4.2 might be higher than the actual value while the ion is immersed in the condensate.

4.3 Atom Loss from the BEC

To understand the interaction processes between the ion and the neutral atoms, the collision cross-section provides a first important piece of information. For a general atom ion interaction, the cross-section is known from theory [52, 45] and it depends on the collision energy. Thus measuring the cross-section provides information about the collision energy. Atom loss from the BEC and the way how the number of atoms evolves with increasing interaction time allow some insight in the dynamics of the interacting system.

The experimental sequence here is identical to the one described in the previous section 4.2. Fig. 4.3 shows the measured number of condensed atoms, once from the same set of data as used in Fig. 4.2, and a second set of data obtained from a measurement where the ion is precooled before immersing it into the BEC. This precooling is achieved by displacing the ion less far from the cold neutral cloud during the last step of evaporative cooling. The ion then is already cold as it enters the BEC, which is confirmed by measuring the ion mean energy with the fluorescence method. This leads to a different atom loss dynamics, shown in Fig. 4.3.

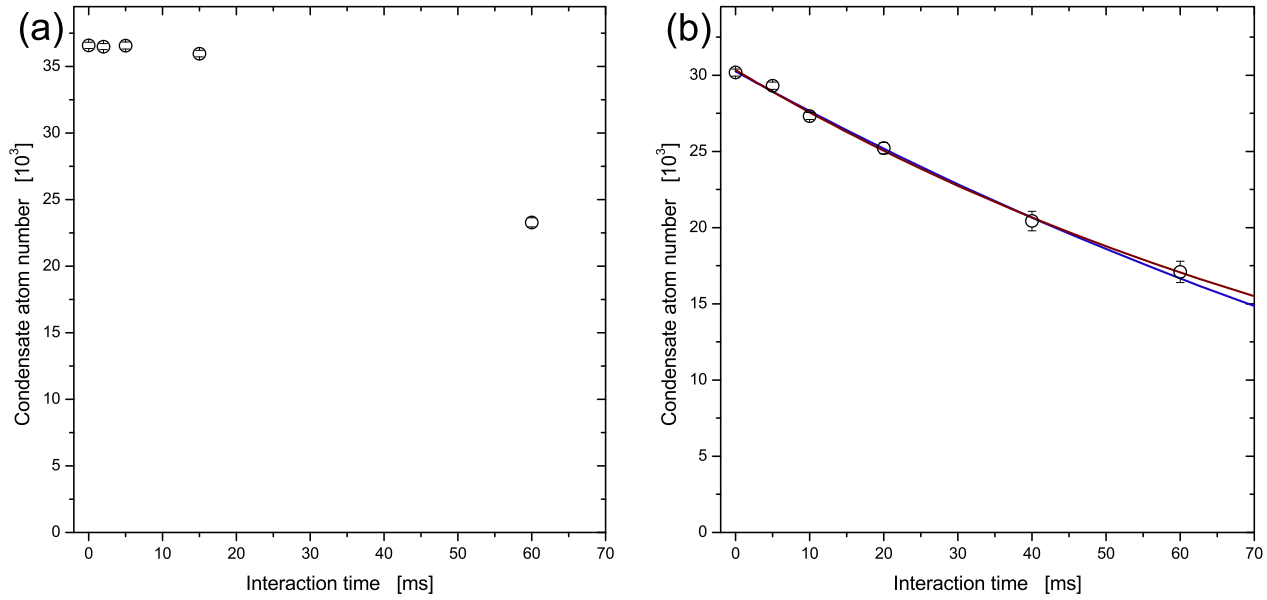

Figure 4.3: Collision induced atom loss from the condensate. In (a), the initially hot ion undergoes only few collisions since the ion trajectory extends over a region much larger than the condensate. After 15 ms, when the ion gets cold enough for its trajectory to better overlap with the neutral atom density distribution, more collisions occur, which is signaled by an increase of neutral atom loss. In (b), the initial ion energy is already low, resulting in a high scattering rate from the beginning of the interaction time. The data are fitted with the depletion model (blue) and the overlap model (red).

To link the obtained loss signals with a calculated cross-section, a model for the dynamics of the combined system is required. In this respect, the data with the precooled ion are

preferred, as the dynamics is simpler. This is because for data obtained with the initially hot ion, a model must include dynamics of both the ion energy and the condensate, while in the case of the precooled ion, the evolution of its energy can be neglected.

In the experiments with a condensate in the optical dipole trap we can attribute the loss rate to the collision rate. This approximation makes sense, because the transfered energy in most of the collisions is expected to be large compared to the neutral trap depth. As a consequence, those collisions lead to a neutral atom loss. Additionally, secondary collisions between the fast neutral atom on its way leaving the condensate, and a remaining cold atom only occur with a probability of less than 0.3, for the specific condensate parameters of this experiment.

From the data shown in Fig. 4.3b we find an initial loss rate of $\sim 250\,\mathrm{kHz}$. In the following, different models will be discussed to attribute this loss rate with a collision rate of the form

$$\gamma = n_{BEC}\,\sigma(E_c)\,v\ . \tag{4.3}$$

For the cross-section, the $E_c^{-1/3}$ energy dependent result from [45] (Eqn. (4.2)) will be used. The density n_{BEC} of the Bose-Einstein condensate can be calculated in the Thomas-Fermi approximation [98]. The remaining free parameters in Eqn. (4.3) are the velocity v together with the collision energy E_c.

From here, the most direct approach would be to use the thermal velocity of the ion for v and the temperature of the ion to calculate E_c. With the observed collision rate this approach results in an ion temperature of 45 nK. This result is inconsistent with the applied model in more than one point. First, that temperature is too low to cause any further loss of atoms from the condensate. Secondly, if the ion was that cold, it essentially would not move through the condensate anymore, meaning that the velocity of the ion is not a good choice to be used as v in Eqn. (4.3). A different model is required therefore.

If one assumes the ion to be rather well localized to some small region inside the condensate, and the collision rate to be high enough, local depletion of the condensate density is the consequence. In that case, the relevant velocity in Eqn. (4.3) is given by the flow of condensate atoms into the region occupied by the ion. The velocity is approximated by the speed of sound and the occupied volume is a convolution of the thermal width of the ion's trajectory with the energy dependent cross-section, Eqn. (4.2). The expected collision rate for different ion temperatures, for this depletion model, is shown in Fig. 4.4 in blue. Combined with the measured atom loss rate, this model yields a mean ion energy of $k_B \cdot 2\,\mathrm{mK}$. The prerequisite in the depletion model is that the time required for the condensate to refill the density hole is much longer than the time for the ion to deplete that region. For very low ion energies this condition is well fulfilled. At 2 mK however, the timescales are only a factor of 3 apart (80 μs for depletion and 240 μs for refilling), and at 8 mK the two timescales are identical. This means that already at 2 mK, depletion is not complete and the model overestimates the

collision rate, as not every atom moving into the ion region will collide immediately.

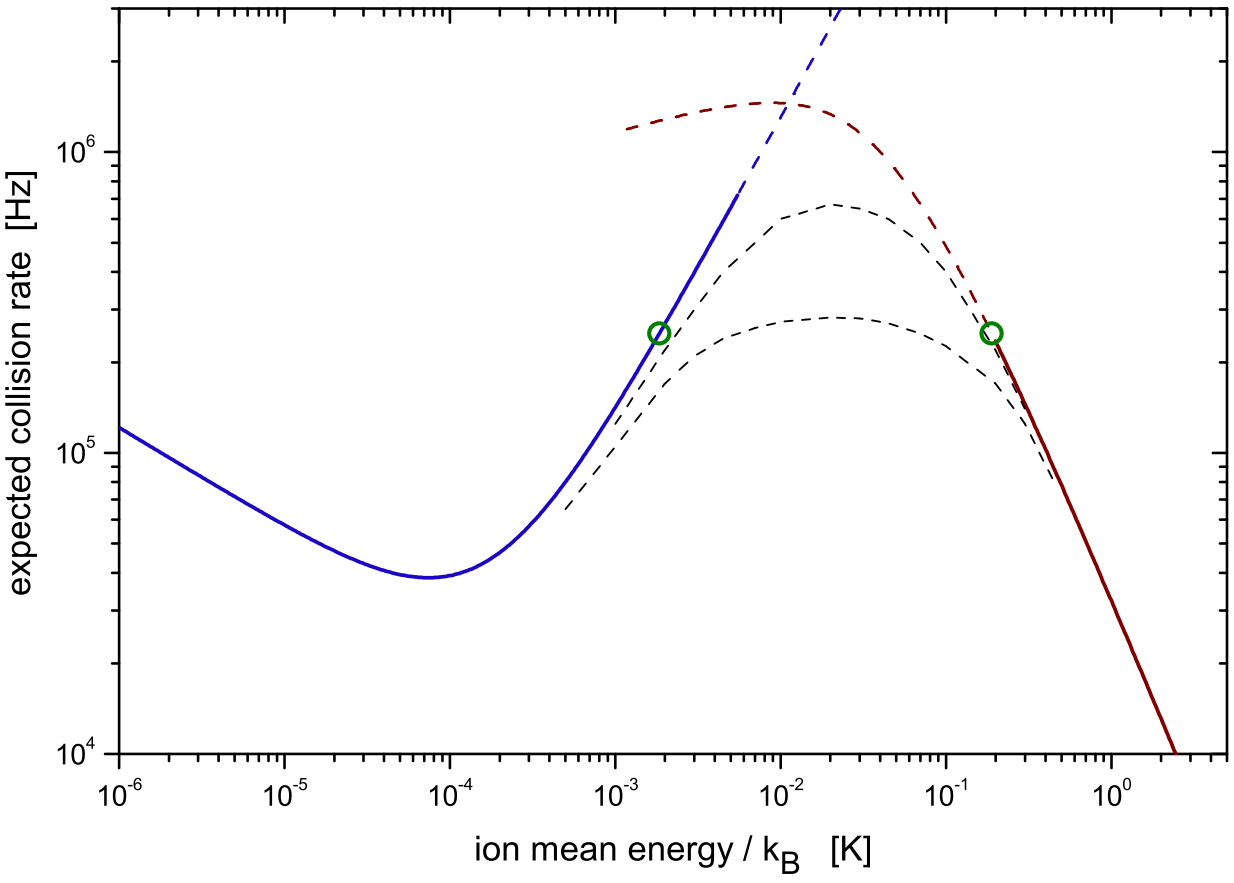

Figure 4.4: Shown are the expected collision rates from the depletion model (blue), valid for low ion energies, and the reduced overlap model (red), valid for high ion energies. The points where the experimentally observed loss rate intersects with the two models are marked with green circles. In the energy regime where the models loose their validity, the lines are dashed. In between, in the energy regime where only weak depletion is expected, the two black dashed lines mark two different guesses of possible collision rates. The real collision rate is expected to lie between them.

Another model has to be used if the energy of the ion is high enough, such that the typical ion trajectory extends over a larger region than the condensate density. In that case, the thermal velocity of the ion has to be used in Eqn. (4.3) for v. Additionally, the overlap between the condensate density and the ion trajectory enters as an attenuating factor into the collision rate. This overlap model does not include any depletion effects. It is therefore valid if the thermal width of the ion is much larger than the condensate. For our experiment, the two length scales are identical for an ion energy of $k_B \cdot 200\,\mathrm{mK}$. With this model, our observed loss rate could be explained with an overlap of 9% and an ion energy of $k_B \cdot 190\,\mathrm{mK}$. Again, at this energy the overlap model is only approximate and because of onsetting depletion effects, the model overestimates the collision rate.

Overall, there is a qualitative agreement between expected collision rates from Eqn. (4.2)

with our observed atom loss rate and the ion temperature measured (cf. section 4.2). However, neither the pure depletion, nor the overlap model are fully self consistent in the parameter range of our measurement, as both elements contribute to the observed rate. Concluding from this, the real temperature of the ion is expected to be larger than 2 mK but smaller than 190 mK.

So far the two models have only been discussed to describe an initial but constant collision rate. If one considers the dynamics of the system, i.e. how the number of atoms remaining in the condensate evolves, a mathematically different behaviour is found between the two models. For weak overlap an exponential decay of atom numbers is expected. Conversely, in the depletion model the loss rate scales with $n_{BEC}^{3/2}$ ($\sqrt{n_{BEC}}$ from the speed of sound) or, in terms of condensate atom number, like $N^{3/5}$. Thus, the differential equation $\dot{N}(t) = -N(t)^{3/5}/\tau$ describes the loss dynamics, and it is solved by $N(t) = \left(N_0^{2/5} - \frac{2}{5}t/\tau\right)^{5/2}$. Despite the different dynamics, the data in Fig. 4.3 do not allow a discrimination between the depletion and the overlap model. Both fits are shown and the reduced chi-square is only insignificantly lower for the exponential decay.

4.4 Effect of Excess Micromotion

In the previous section, the neutral atom loss rate indicates a mean ion energy which is clearly higher than the temperature of the neutral atoms. This requires a continuous source of energy coupled to the energy of the ion. One well known source of continuous energy intake is ion trap heating. However, the measured ion trap heating rate of ~ 100 mK/s can account for only 10% of the observed neutral atom loss rate at best. Another source of energy must be responsible therefore. In the following it will be assumed that excess micromotion is responsible for the continuous energy transfer from the RF-driving field onto the collision partners.

To motivate this process, lets first consider the classical trajectory of an initially cold ion, with some excess micromotion. Here, cold means that the secular velocity is zero. If this ion collides with an ultracold neutral atom, the relative collision velocity is given by the excess micromotion. In the simplified case of equal masses of the ion and the atom, and for full backward scattering, the colliding partners will just exchange their momentum and the ion will be at rest after the collision. Depending on the phase of the RF-driving field in the instant of the collision [74, 99, 100], the ion being at rest has the meaning of a secular velocity of the same magnitude as the micromotion velocity. Thus, the ion's secular energy and the atom's energy are both increased by the collision. Fig. 4.5 shows three possible ion trajectories for the initially cold ion, colliding with a neutral atom in the presence of excess micromotion.

This simplified picture is meant for illustration only, as it neglects many important system parameters, such as different masses of the ion and the neutral atom, the differential cross-section, and the initial secular energy of the ion. A detailed discussion of all these parameters will be given in chapter 5 by using a Monte-Carlo simulation. Here, we just state that excess micromotion prevents the ion from thermalizing with the ultracold neutral atoms. Also, one can guess that the ion's secular velocity after many collisions might be directly related to the velocity amplitude of the excess micromotion. Thus, we expect a quadratic dependence of the ion mean energy on an externally applied electric offset field. Our measurement of the ion mean energy for different electric offset fields is explained in the following.

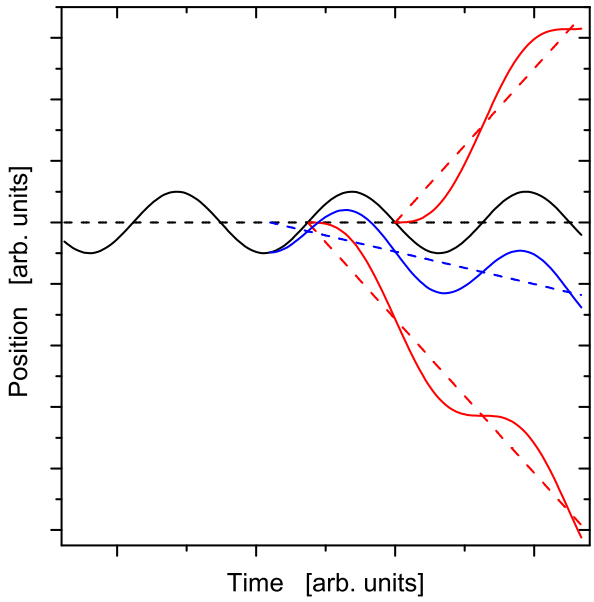

Figure 4.5: Trajectory in one dimension of an initially cold ion with excess micromotion. The unperturbed trajectory (black) contains a constant contribution (dashed line) from the secular motion plus the excess micromotion. The two red lines are example trajectories if the ion collides in the moment when its micromotion velocity is at its maximum. The blue line depicts another possible trajectory for a smaller but non-zero micromotion velocity at the time of the collision. The departure of the secular position (red and blue dashed lines) from the unperturbed case indicate the collision induced energy transfer from the RF-driving field to the collision partners.

Similar to the experiment when we first measured sympathetic cooling in section 4.2, we determine the ion's mean energy by observing the fluorescence rate during the Doppler cooling of the ion as described in section 3.4, after the ion has interacted with the ultracold atoms for a time long enough for its energy distribution to reach a steady state. With an energy resolution of $k_B \sim 500\,\mathrm{mK}$ our measurement aims at producing mean ion energies in the range up to $k_B \sim 10\,\mathrm{K}$ to achieve a reasonable signal to noise ratio. At such energies, the ion trajectory extends over $\sim 50\,\mu\mathrm{m}$, and the spatial overlap with a much smaller condensate would be extensively small. Instead, we use an ultracold thermal cloud of neutral atoms confined in the magnetic trap with trapping frequencies of $2\pi\{28, 28, 8\}\,\mathrm{Hz}$. This yields a typical width of the thermal cloud of $60\,\mu\mathrm{m}$ at $300\,\mathrm{nK}$. With $2 \cdot 10^6$ neutral atoms, the central density of $1.3 \cdot 10^{18}\,\mathrm{m}^{-3}$ is two orders of magnitude lower than in the previous condensate. To account for the resulting lower collision rate, we increase the interaction time to 8 s. During the interaction, an electric offset field in the range of $\pm 30\,\mathrm{V/m}$ is applied to increase the excess micromotion. As a side effect, the ion trap centre is displaced by $\pm 15\,\mu\mathrm{m}$,

which we compensate for by simultaneously displacing the magnetic trap centre through application of magnetic offset fields. After the interaction time, when the neutral atoms have been released from their trap, the electric offset field is changed back to the best compensated value, to achieve identical conditions for the ion energy detection with the fluorescence method.

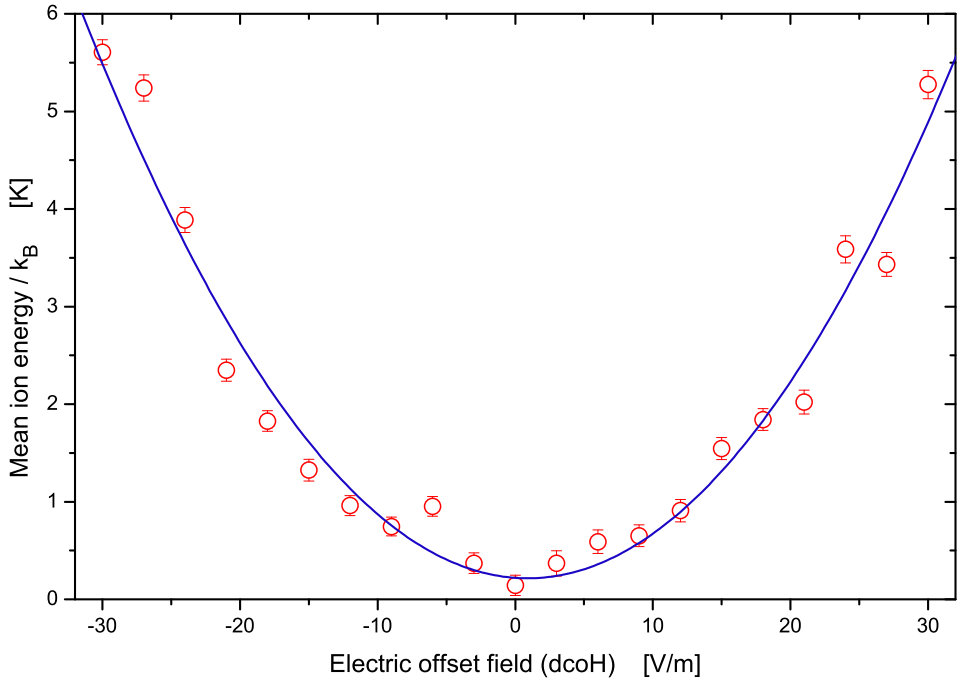

Figure 4.6: Measured mean ion energy for different settings of the excess micromotion after 8 s of interaction. Each data point is obtained from a least-chi-square fit to fluorescence data averaged over $\sim$ 40 realizations of the experiment each. The indicated error is calculated from propagating the photon shot-noise and neglects the sampling error from the energy distribution. The data are fitted with a polynomial of second order.

The measured ion energies are shown in Fig. 4.6. For each value of the electric offset field the measurement is repeated $\sim$ 40 times. As this number is too small to accurately represent the ion's energy distribution, the error is underestimated by a factor $\sim$ 3 (cf. Fig. 3.10). The mean ion energy is fitted with the expected quadratic dependence on the electric offset field with the function $a_2(\vec{E}_{dcoH} - \vec{E}_{dcoH,0})^2 + b_0$. The resulting fit parameters are $a_2 = k_B\, 5.52(15)\,\mathrm{mK/(V/m)^2}$, $\vec{E}_{dcoH,0} = 0.9(2)\,\mathrm{V/m}$, and $b_0 = k_B\, 0.27(29)\,\mathrm{K}$. a_2 should be compared with the ratio between the excess micromotion energy $E_{mm,e} = \frac{m_i}{2} v_{mm,e}^2$, $v_{mm,e}$ being the amplitude of the excess micromotion velocity, and the square of the applied electric offset field $\vec{E}_{dcoH}$. They are compatible considering a geometric attenuation of $\sim$ 0.9 between the technical parameter $\vec{E}_{dcoH}$ and the physical electric offset field. The non-zero $\vec{E}_{dcoH,0}$ indicates uncompensated drifts on $\vec{E}_{dcoH}$ during the measurement, or systematic differences between the period of micromotion compensation and the time of atom-ion interaction. The value of less than 1 V/m is however small. The energy offset b_0 is compatible with zero within the error.

It is expected slightly above zero, as there is excess micromotion along the ion trap symmetry axis of $\sim 3.5\,\mathrm{V/m}$ and micromotion with orthogonal phase, cf. section 3.2. Also, a small ion energy increase is expected within the time between the end of the interaction period and the begin of the energy measurement, as already mentioned in section 4.2. Moreover, the error distribution of the ion energy detection method is asymmetric for the very low energies, which technically also contributes to an increase of b_0.

Overall, this measurement confirms the expected quadratic dependence of the mean ion energy on the excess micromotion. A series of three experiments, each of the type as shown in Fig. 4.6, has been conducted and validate the reproducibility of the result.

Assuming the quadratic dependence of the mean ion energy on the excess micromotion to extrapolate into the energy regime below our detection resolution, we can now calculate the ion energy for the previous measurements from the known excess micromotion parameters. In the best compensated case the micromotion is dominated by the contribution along the trap symmetry axis. The extrapolation results in an ion energy of 70 mK, compatible with the observed neutral atom loss from the condensate (cf. Fig. 4.4).

4.5 Energy Dependent Elastic Scattering

As has been demonstrated in the previous section, tuning the excess micromotion allows us to control the mean ion energy and thus the mean collision energy between the ion and neutral atoms. This in return, allows a clear distinction between the Langevin and the quantum scattering model, since they depend differently on energy. During the same measurement as described in the previous section, we monitor the atom loss and temperature increase of the thermal cloud. We plot these values against the mean ion energy in Fig. 4.7, where the ion energy is now calculated with the interpolation of the fit shown in Fig. 4.6.

Both the neutral atom loss signal and the temperature increase show a clear energy dependence. Therefore, the observed effects can only be explained with the quantum model for the cross-section, but not with the Langevin model. Also, the observed atom loss rate is more than one order of magnitude larger than the expected Langevin collision rate, while amounting to about 60% of the expected full quantum scattering rate. The other 40% of collisions explain the observed temperature increase of the neutral atom cloud. Since many of those collisions involve a deflection with very small deflection angle, the transferred energy from the ion to the atom can be very small. If this energy is smaller than the magnetic trap depth, which is approximately $8\,\mu$K, then the atom remains trapped and the transferred energy thermalizes within the neutral cloud.

The obtained data can be modelled with good accuracy using a Monte-Carlo simulation[1]. The simulation will be described in detail in chapter 5, and a comparison with more experi-

[1]Here, the used simulation parameters to fit the data are $T_{a,0} = 289\,\mathrm{nK}$, $N_{a,0} = 1.79 \cdot 10^6$, $\omega_a = 2\pi \times 23\,\mathrm{Hz}$, $c_z = 2\,\mu\mathrm{m}$ and $E_{td,a} = k_B \cdot 7.1\,\mu\mathrm{K}$.

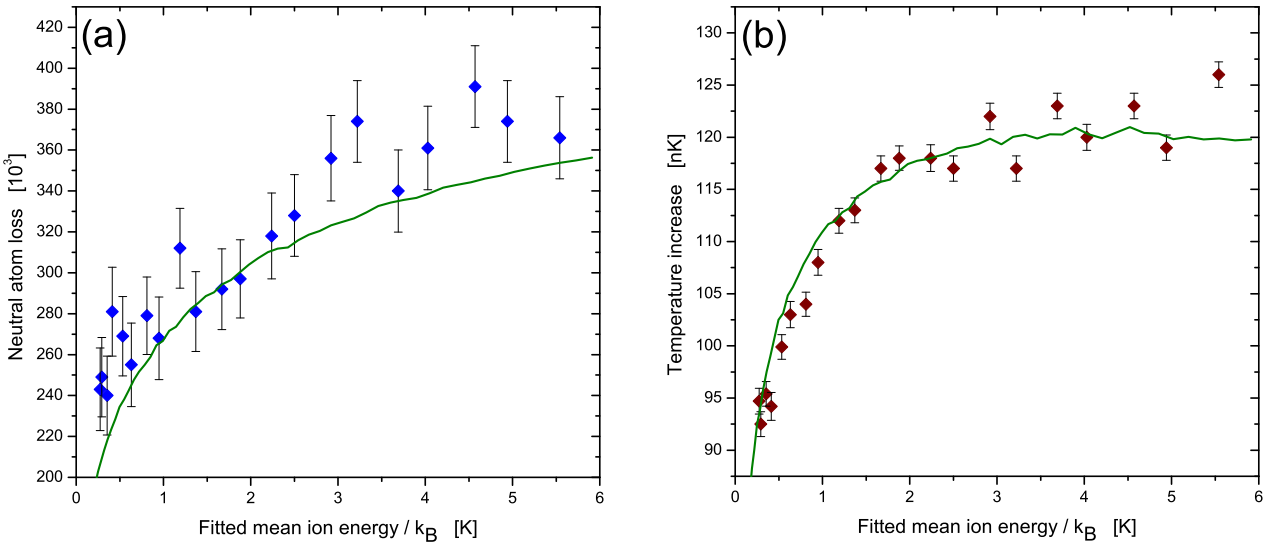

Figure 4.7: Observed neutral atom loss (a) and temperature increase (b) of a thermal ^{87}Rb cloud after 8 s of interaction with an $^{174}Yb^{+}$ ion. Each data point is the difference between averages of $\sim$ 40 repetitions of a set of measurements with and one without an ion present. The shown error bars indicate the standard error of the mean. The green line is a fit using the Monte-Carlo simulation which is described in chapter 5. The noise seen on the simulation data stems from the randomness of the collision process, the amount of displayed noise corresponds to the expected variation of a single measurement.

mental data of the same type as in Fig. 4.7 will be made in section 5.3.4.

In conclusion, the presented measurement observes effects described by the quantum scattering model, and yields collision rates which are clearly beyond of what the classical Langevin cross-section can account for. To our knowledge, no experiment has seen such a clear effect of the $E^{-1/3}$ energy dependence in the ion-neutral collision cross-section before. Our measurement has been made possible by the high sensitivity of the ultracold atoms to very small energy transfers.

4.6 Inelastic Collisions

In all the previously described measurements, it has been carefully checked that exactly one Yb ion is present before and after the interaction, with the detection methods described in section 2.3.2. Experimental iterations where the ion has been lost during the interaction have been discarded in the data analysis. Here, we now look at exactly that fraction of experimental iterations, where the ion is lost during the interaction.

In the first series of measurement, we interpret the absence of an ion fluorescence signal after the interaction time as an ion loss. This can be caused by different types of inelastic collisions. Elastic scattering should have a negligible contribution to ion loss in our system. With the ion-atom mass ratio of 2, and an estimated ion trap depth of 250 meV we expect an ion loss

probability of less than 10^{-12} per elastic collision, even for the highest used excess micromotion setting. The calculation of such loss probabilities will be explained in section 5.2.3. A small background loss rate of the ion, measured without any interaction with neutral atoms, of about one loss in 1000 s, needs to be subtracted from the observed ion loss rate during the interaction. It remains the inelastic collision rate, which lead to a loss of the fluorescence signal.

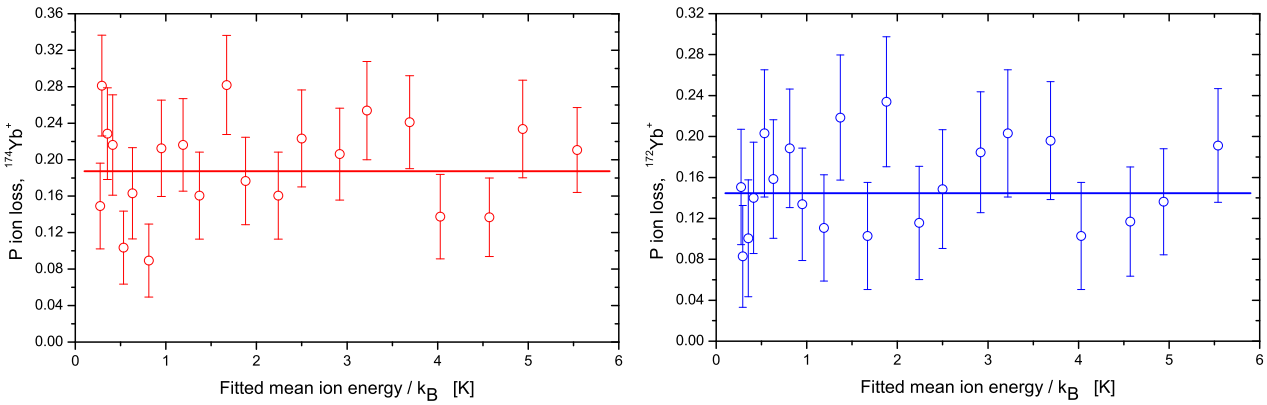

Figure 4.8: Observed ion loss probability for two different isotopes, ^{174}Yb on the left and ^{172}Yb on the right [28]. The ion loss is detected by a missing fluorescence signal after 8 s of interaction with a thermal cloud of ^{87}Rb. The background loss probability of the ion, present even without interaction with the neutral atoms, has already been subtracted from the data. The average loss probability is indicated with a line.

In the following, loss probabilities will be calculated with the maximum likelihood estimator $P_l = (N_l + 1)/(N_l + N_k + 2)$, with N_l (N_k) the number of measurements where the ion is lost (kept). The error on P_l is estimated by $\Delta P_l = \sqrt{\frac{(N_l+1)(N_k+1)}{(N_l+N_k+2)^2(N_l+N_k+3)}}$, which is the square root of the variance of the beta distribution.

First we investigate the energy dependence of the inelastic collision rate. The same set of measurements as in the previous two sections is used. We plot the ion loss probability against the fitted ion mean energy in Fig. 4.8. We observe no significant energy dependence of the inelastic collision rate. It is thus compatible with a Langevin type cross-section, proportional to the inverse of the collision velocity. Comparing the measured inelastic rate with the full Langevin cross-section, we find a suppression factor of 10^{-5}. This number indicates the probability for an inelastic process to happen within a close-encounter type collision. We have measured the inelastic collision rate for two different isotopes of the ion, ^{172}Yb and ^{174}Yb, and we find the same rate coefficient within the error.

To test the density dependence of the ion loss process we change the ion's position within the neutral cloud. Therefore, the magnetic trap for the neutral atoms is displaced by means of a magnetic offset field. In this way, the excess micromotion is unchanged and the ion is kept at the lowest possible energy where the extent of the ion's trajectory is the smallest. The observed ion loss rate reflects the local neutral density, as shown in Fig. 4.9. The neutral density

distribution can be calculated from the measured neutral atom number and temperature, together with the magnetic trapping frequency. The observed ion loss rate depends only linearly on the density, which indicates that the inelastic processes are caused by binary collisions. No hint for three-body effects is seen. The found rate constant for ion loss is $2.7(6)\,10^{-20}\,\mathrm{m}^{-3}$.

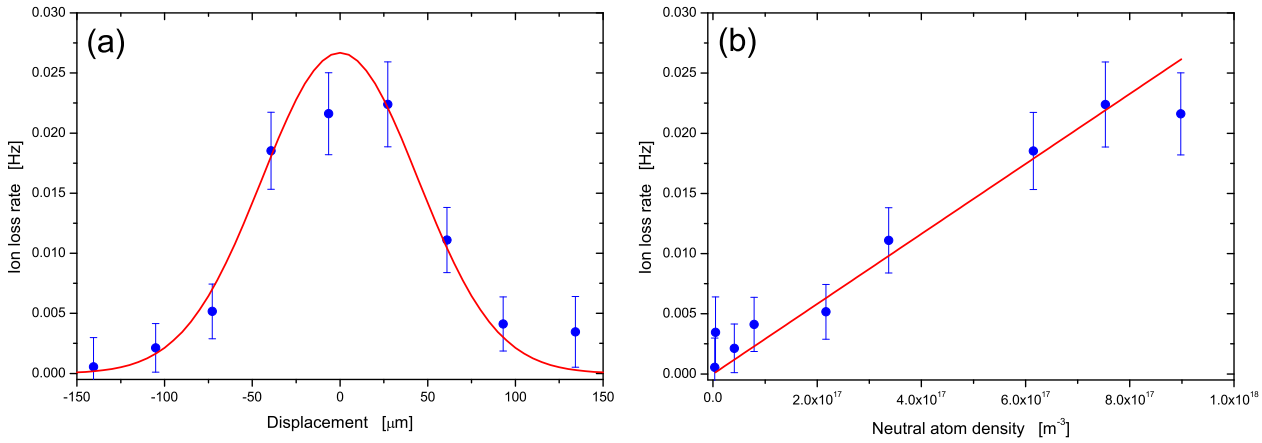

Figure 4.9: Density dependence of the ion loss probability [28]. The neutral cloud is displaced such that the ion is immersed at a point of decreased density. In (a) the ion loss rate is plotted against the displacement. The rescaled local density is shown in red. In (b) the loss rate is shown vs the neutral atom density. A proportional model fits the data well.

In addition to detecting the ion loss rate, we can distinguish if the internal energy transformed into kinetic energy, in the inelastic process, is larger or smaller than the ion trap depth of 250 meV. If it is smaller, the charged reaction product should still be trapped and cooled by elastic collisions with the neutral atoms. Further, the mass of a trapped reaction product can be determined by a trap frequency measurement if a second, bright ion with known mass is trapped at the same time [61, 63]. The Coulomb crystal of two ions forms a system of coupled harmonic oscillators with mass dependent Eigen-frequencies. Although the repelling Coulomb force is highly non-linear in the range required as oscillation amplitude to detect a decrease in fluorescence, the common mode can be seen, as the modulation on the inter-particle distance is not too large. To identify the inelastic reaction products with this method of mass spectrometry, we initially prepare the ion trap with two ^{174}Yb ions. After the interaction, we select the events where one bright ion remains, but displaced from the centre of the ion trap, indicating the presence of another dark ion (cf. Fig. 2.6). Then the trap frequency measurement, as described in section 3.3, is performed and the resonance frequency reveals the mass of the dark ion. Two fluorescence signals of this type are shown in Fig. 4.10a, one with a dark Yb ion, and one with a Rb ion.

The only reaction product detected yields the mass of a Rb ion, indicating a charge exchange process. The ionization energy of Rb differs by 2 eV from the ionization energy of

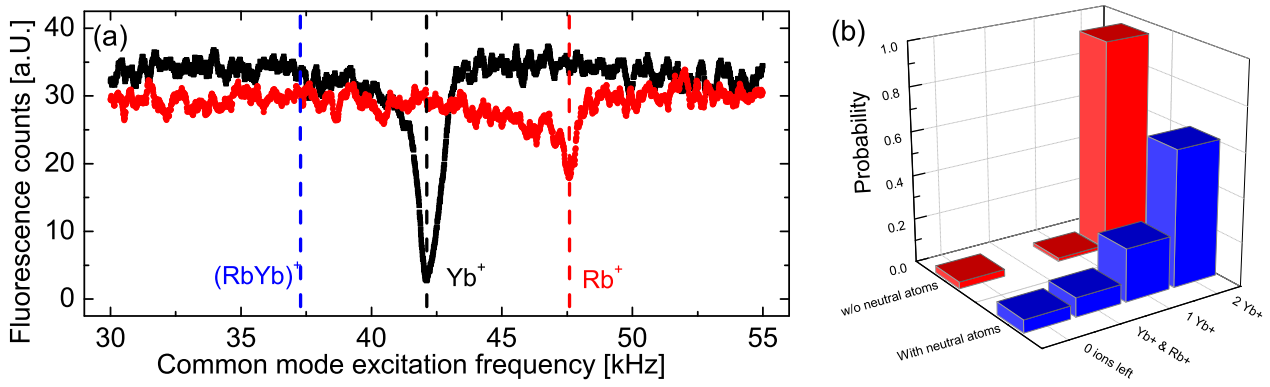

Figure 4.10: Detection of inelastic reaction products [28]. (a) shows two fluorescence signals from the mass spectrometry. One bright Yb ion is trapped next to a dark ion of unknown mass. The common mode frequency is measured by exciting the mode with modulated fluorescence laser intensity. The common mode excitation frequency reveals the mass of the unknown ion. (b) summarizes the observed outcomes (blue) from 486 experimental runs with initially two trapped Yb ions interacting with the neutral Rb atoms for 8 s. The result should be compared to the reference measurement (red) of 543 experimental runs with initially two trapped Yb ions but without any interaction with neutral Rb.

Yb. The charge exchange process which neutralizes the Yb and ionizes the Rb is exothermic. If the 2 eV of internal energy are transformed into kinetic energy of the reaction products, the Rb ion, which obtains 2/3 of the energy, cannot be trapped and is lost. The detection of a trapped Rb ion thus additionally indicates the charge exchange process being radiative, meaning a photon is emitted which takes up the released energy. By comparing the observed inelastic rates for which the Rb ion remains trapped against being lost, we can estimate the branching ratio of radiative to non-radiative charge exchange. The measured probabilities for the different outcomes of the experiment are shown in Fig. 4.10b. The non-radiative charge exchange process appears to be two times more likely than the radiative process.

Note that these experiments have all been conducted without any light present during the interaction time. Care needs to be taken to shield near resonant stray-light, to avoid photo-ionization of Rb atoms. As an indicator, the dataset from the measurement of Fig. 4.10b is filtered for events starting with a single Yb ion and ending with an additional Rb ion. No such event has been detected, ruling out the background process of photo-ionization.

Against our expectations, the mass spectrometry has not detected a single event of a $YbRb^+$ molecule. Either the rate for its creation is much smaller than for a charge exchange process, or any existing molecule is rapidly destroyed in a secondary process. One possible decay channel for such a molecule is the reaction $Rb + YbRb^+ \rightarrow Rb_2 + Yb^+$, in which case the Yb ion would act as a catalyst to form Rb_2.

Chapter 5

Kinetics of a Single Trapped Ion in an Ultracold Buffer Gas

This chapter reports about the results obtained from a Monte-Carlo simulation of the single ion colliding elastically with an ultracold buffer gas. It follows closely the content of [101][1], which has been written as a part of this thesis.

Beyond the experimental understanding of energy dependent scattering and its relation to excess micromotion, as described in the previous chapter, the simulation also explores parameters which are not easily tunable in the experiment. For instance, the influence of the ratio between the mass of the ion m_i and the mass of the neutral atom m_n, will be investigated in detail. For very heavy neutrals, runaway heating of the ion is expected [74], whereas very light neutrals enable efficient buffer gas cooling. In the mass ratio regime between the two extremes increased ion trap loss has been observed [102, 103]. The effect has been explained by non-thermal energy distributions of the ion obtained from Monte Carlo simulations [104]. Such numerical simulations are a well established tool to model a trapped ion interacting with a buffer gas [105, 106, 107]. They can account for energy dependent scattering rates, complex electric field geometries, and other experimental parameters, which are difficult to treat analytically. In previous calculations, buffer gases at ambient temperatures have been assumed, and the cooling of the ion has been limited to the buffer gas temperature. However, in our experiments with the ultracold neutral gas a new energy scale related to excess micromotion has become dominant, as has been observed in section 4.4.

The chapter is organized as follows: In section 5.1 the basic simulation procedure and the underlying physical model are described. The classical Langevin interaction model is applied in section 5.2 to derive the ion's energy statistics depending on the mass ratio, trap geometry, and scattering rate. In section 5.3 effects on the neutral atom cloud are explained as a result of the energy dependent differential cross-section and the non-uniform neutral density distribution. The numerical results are in good agreement with the experiments of chapter 4.

[1] Permission to reproduce has been granted by IOP Publishing Ltd.

5.1 Simulation Model

The time evolution of a trapped single ion colliding with ultracold atoms is modelled using a simulation consisting of an analytical and a numerical part. In the time between collisions, trajectories are analytically described using the pseudo-potential approximation, while elastic collisions are taken into account using Monte Carlo techniques. Reactive collisions, such as charge exchange, are not considered by the model.

5.1.1 Ion Trajectory

We consider a single ion confined by the RF-quadrupole potential of a linear Paul trap

$$\Phi_{RF} = V_0 \frac{x^2 - y^2}{2\,{R_T}^2} \sin(\Omega_T\, t) \; . \tag{5.1}$$

Here, V_0 is the RF-voltage amplitude applied with frequency Ω_T to electrodes at a distance R_T away from the trap symmetry axis. In addition, we consider a static quadrupole potential confining the ion along the trap symmetry axis with trapping frequency ω_z,

$$\Phi_{static} = \frac{m_i}{2\,Q}\,\omega_z^2 \left(z^2 - \frac{1}{2}(x^2 + y^2) \right) \; . \tag{5.2}$$

Q is the ion's charge. Mathieu equations describe the classical motion of an ion in the combined potential (see for example [75, 76]), using the parameters $a = 2\,\frac{\omega_z^2}{\Omega_T^2}$ and $q = \sqrt{8}\,\frac{\omega_p}{\Omega_T}$ with $\omega_p = \frac{Q}{\sqrt{2}\,m_i}\,\frac{V_0}{{R_T}^2\,\Omega_T}$. For $a < q^2/2 \ll 1$ the Floquet solution to first order in q yields

$$r_{ion,x} = A_x \sin(\omega_x\, t + \varphi_x) \left[1 + \frac{q}{2} \sin(\Omega_T\, t) \right] \tag{5.3a}$$

$$r_{ion,y} = A_y \sin(\omega_y\, t + \varphi_y) \left[1 - \frac{q}{2} \sin(\Omega_T\, t) \right] \; , \tag{5.3b}$$

which is usually referred to the pseudo-potential approximation. It consists of a rapidly oscillating micromotion term and the secular motion, which is harmonic with frequencies $\omega_{x,y} = \sqrt{\omega_p^2 - \frac{1}{2}\omega_z^2}$ and amplitudes $A_{x,y} = \frac{1}{\omega_{x,y}} \sqrt{\frac{2\,E_{x,y}}{m_i}}$. A full secular trajectory $\vec{r}_{sec}$ including the harmonic motion along the trap symmetry axis is described by three energies E_j and three phases φ_j, $j \in \{x, y, z\}$, with

$$r_{sec,j} = \frac{1}{\omega_j} \sqrt{\frac{2\,E_j}{m_i}} \sin(\omega_j\, t + \varphi_j) \; . \tag{5.4}$$

This formula, describing a three-dimensional harmonic oscillator, will be used throughout the following calculations to approximate the ion's position. The total secular energy $E_x + E_y + E_z$ will be referred to as the ion energy.

The motion of the ion is affected by collisions with the neutral atoms. We assume them

to be instantaneous, which implies that every collision is sensitive to the momentary relative velocity, including the micromotion[2]. Therefore, we consider a number of effects causing contributions to the micromotion. Firstly, the intrinsic micromotion described in Eqn. (5.3) is proportional to the distance of the ion from the centre of the RF-quadrupole field. Secondly, static offset electric fields displace the minimum of the ion trapping potential by a distance $(\Delta x, \Delta y)$ from the symmetry axis of Eqn. (5.1). Thirdly, RF pickup on end-cap electrodes can lead to micromotion along the trap symmetry axis. These contributions are summed in the expression

$$\vec{v}_{mm} = \sqrt{2}\,\omega_p \begin{pmatrix} r_{sec,x}(t) + \Delta x \\ -r_{sec,y}(t) - \Delta y \\ c_z \end{pmatrix} \cos(\Omega_T\, t)\ , \tag{5.5}$$

where c_z parameterizes the micromotion along the trap symmetry axis[3].

The ion velocity considered for collisions is

$$\vec{v}_{ion} = \vec{v}_{sec} + \vec{v}_{mm}\ , \tag{5.6}$$

with $\vec{v}_{sec} = \frac{\mathrm{d}}{\mathrm{d}t}\vec{r}_{sec}$. This $\vec{v}_{ion}$ is similar to the time derivative of Eqn. (5.3) but includes all the excess micromotion terms.

5.1.2 Collision Dynamics

The simulation uses classical trajectories for the motion of the ion. Therefore, its validity is restricted to ion energies well above the energy quanta of secular motion $\hbar\omega$. The temperature of the ultracold buffer gas is assumed to be well below this energy scale, and in the collision the neutral atom's initial energy is neglected. Due to conservation of energy and momentum, the elastic scattering process is defined by the scattering angles (θ, ϕ). The ion's velocity changes according to

$$\vec{v}_{ion,f} = (1-\beta)\,\vec{v}_{ion,i} + \beta\,\mathcal{R}\,\vec{v}_{ion,i}\ , \tag{5.7}$$

with $\vec{v}_{ion,i}$ ($\vec{v}_{ion,f}$) being the initial (final) velocity given by Eqn. (5.6) at the time of the collision, $\beta = \frac{m_n}{m_i+m_n}$ and $\mathcal{R}$ is the rotation matrix determined by θ and ϕ, with respect to the direction of $\vec{v}_{ion,i}$. From $\vec{v}_{sec,f}$ and $\vec{r}_{sec}$ a new set of φ_j and E_j can be determined, which describes the ion's trajectory after the collision.

To illustrate its impact on the motion of the ion, Eqn. (5.7) can be rewritten in terms of

[2]This assumption is valid for collision energies above $\hbar\,\Omega_T$.

[3]Not included in this expression are possible additional micromotion terms that are $\pi/2$ out of phase, therefore proportional to $\sin(\Omega_T\, t)$, which can arise, for example, from RF-phase mismatches on opposing electrodes. They are added to $\vec{v}_{mm}$ for simulations where specific experimental data is to be represented and the specific micromotion parameters are known.

the secular velocity, yielding

$$\vec{v}_{sec,f} = (1-\beta)\,\vec{v}_{sec,i} + \beta\,\mathcal{R}\,\vec{v}_{sec,i} + \beta\,(\mathcal{R}-\mathbf{1})\,\vec{v}_{mm}\ . \tag{5.8}$$

This expression shows how $\vec{v}_{mm}$ couples to the secular velocity in every collision. Note that $\vec{v}_{mm}$ is, by definition of Eqn. (5.5), the same before and after the collision since it only depends on the position $\vec{r}_{sec}$ and time t of the instantaneous collision.

5.1.3 Scattering Rate

The probability $\mathrm{d}P_c$ for the ion to collide with a neutral atom within a short time interval $\mathrm{d}t$ defines the scattering rate

$$\Gamma(t) = \frac{\mathrm{d}P_c}{\mathrm{d}t} = n(\vec{x})\,\sigma(E_c)\,v_{ion}(t)\ . \tag{5.9}$$

It is proportional to the neutral atom density $n(\vec{x})$ at the ion's position. The cross-section $\sigma(E_c)$ is usually a function of the collision energy E_c, which, neglecting the energy of the neutral atom, is given by $E_c = \beta\,\frac{m_i}{2}\,v_{ion}^2$.

The ion's position changes on a timescale of ω_j^{-1} while the velocity of the ion v_{ion} changes on a timescale of Ω_T^{-1}. In general, $\Gamma(t)$ will therefore be time dependent in a non-trivial way. The sampling method used to efficiently choose the time of collision is explained in Appendix A.

A technical description of the main simulation loop is given in Appendix B.

5.1.4 Inelastic Collisions

Inelastic processes like charge exchange, spin exchange or molecule formation have been predicted to occur in the hybrid system [52, 45, 53, 24, 54]. In experiments [55, 27, 28, 30], charge exchange, which is typically signaled by the loss of the ion, has been observed at rates many orders of magnitude lower than the elastic collision rate, in the non-resonant case. Spin exchange collisions can occur with rates comparable to elastic scattering [24], and energy from internal states can be transferred to the external degrees of freedom. In a spin-stretched configuration, however, spin exchange is suppressed.

In our simulation, we can include inelastic effects by introducing additional, competing rates, defined as in Eqn. (5.9), but with inelastic cross-sections $\sigma_i(E_c)$ instead. The effect of any inelastic event on the hybrid system depends primarily on the question whether the original ion still exists after the process. If this is not the case, the simulation can be stopped at the first occurrence. If the ion continues to exist, the amount of energy released or absorbed by the internal states of the colliding particles needs to be considered in a modified version of Eqn. (5.7). In either case, our simulation is able to predict the rate at which inelastic events occur, given the inelastic cross-section $\sigma_i(E_c)$. On the other hand, the simulation can be used,

if a rate is measured experimentally, to determine $\sigma_i(E_c)$.

In the following sections we consider elastic processes only, assuming inelastic processes either to happen very rarely, in line with the experiments [27, 28, 30], or to involve only small amounts of internal energy, which do not significantly affect the system.

5.2 Langevin Scattering

The ion-neutral interaction is dominated by the attractive polarization interaction, which is of the form

$$V(R) = -\frac{C_4}{2R^4} \tag{5.10}$$

with $C_4 = \alpha_0 Q^2/(4\pi\epsilon_0)^2$ being proportional to the neutral particle polarizability α_0. R is the internuclear separation. Classically one can define a critical impact parameter $b_c = (2\,C_4/E_c)^{1/4}$ [48]. Collisions with impact parameter $b > b_c$ lead to small deflections. Impact parameters $b < b_c$ result in inward-spiralling trajectories, which lead to almost uniformly distributed scattering angles into all directions as in hard-sphere scattering. For the motion of an ion in a neutral gas only large angle scattering is considered relevant as small deflections do not significantly change the ion's trajectory. The resulting cross-section $\sigma_L = \pi\, b_c^2$ is proportional to the inverse collision velocity, and leads to a scattering rate independent of the collision energy [47].

5.2.1 Energy Scale

Our aim is to determine the energy scale of the ion on its classical trajectory after many collisions such that the initial conditions for E_j can be neglected. Neither the Langevin scattering at its energy-independent rate, nor the ultracold neutral buffer gas, which we assume at $T = 0$, introduce such a scale. As a consequence the only energy scale in the system is defined by the excess micromotion, see Eqn. (5.5). This is in contrast to the case of a buffer gas with non-negligible temperature, where the energy scale is rather set by the temperature of the neutral gas [104].

To associate the excess-micromotion with an energy scale we define

$$E_{mm} = \frac{m_i}{2} v_{mm,e}^2 \tag{5.11}$$

with $v_{mm,e}$ being the full velocity amplitude of the micromotion for an ion in the centre of the ion trapping potential. $v_{mm,e}$ depends on the displacement $(\Delta x, \Delta y)$ caused by the uncompensated offset electric field. Note that when the offset electric field is compensated using a photon correlation measurement [92, 91], photon shot noise usually limits the lowest achievable E_{mm}.

Since $E_{mm,e}$ is the only energy scale in the colliding system it is sufficient to express

all energies in units of $E_{mm,e}$. This gives general results for any amplitude of uncompensated micromotion. It also implies that any statistical measure of ion energy has to scale with $E_{mm,e}$ and therefore with the square of the excess micromotion amplitude, as has been experimentally observed in section 4.4.

5.2.2 Energy Spectrum

In order to treat scattering in the presence of micromotion in its most general form we choose all trap frequencies $(\omega_{x,y,z}, \Omega_T)$ to have irrational ratios. We assume a very low homogeneous neutral atom density such that the scattering rate Γ is much smaller than the trap frequencies. This ensures that two consecutive collisions happen at uncorrelated positions.

We obtain the energy spectrum from the simulation by binning the secular energy after each collision on a logarithmic scale. This measures a logarithmic energy probability distribution $\mathrm{d}P(E)/\mathrm{d}\log(E)$. Fig. 5.1 shows such energy spectra for three different mass ratios of the atom and the ion. For heavier neutral atoms the mean energy of the ion increases and a tail in the spectrum towards higher energies becomes dominant. Even for equal masses ($\beta = 0.5$) the tail towards high energies is evident when compared to the thermal distribution with the same mean energy. For any mass ratio, the obtained spectrum distinctly differs from a thermal distribution, also because very low energies ($E \ll E_{mm}$) are extremely rare. This supports the validity of the classical treatment of trajectories and instantaneous collisions ($E > \hbar\Omega_T$).

A power law, $\mathrm{d}P(E)/\mathrm{d}\log(E) \propto E^{\alpha}$ nicely fits the tail in the spectrum towards high energies for $m_n > m_i$ or $\beta > 0.5$ [104]. As β is increased further, towards even heavier neutrals, the negative exponent α approaches 0, at which point the spectrum does not converge with time anymore and runaway heating starts to dominate the evolution of the ion's energy. The critical mass ratio parameter β_{crit} can be found by extrapolating the exponent $\alpha(\beta)$ towards $\alpha(\beta_{crit}) = 0$. The quantity β_{crit} is not a universal number but is a function of the trap geometry. It depends on the ratio $\frac{\omega_p}{\omega_z}$ or, expressed in the ion trap parameters a and q, on $\frac{q^2}{a} = (\frac{2\omega_p}{\omega_z})^2$. The dependency is explained by the fact that axial confinement leads to radial deconfinement and thereby to an increase of the ratio between average micromotion and secular energy. For three different cases the extrapolation to β_{crit} is shown in Fig. 5.2. Our data are compatible with the critical mass ratio previously found for a specific trap geometry [104]. For very elongated traps ($\omega_z \ll \omega_p$) we find $\beta_{crit} = 0.685$, corresponding to a mass ratio $\frac{m_n}{m_i} = 2.17$.

5.2.3 Average Energy and Lifetime of the Ion

To evaluate the effectiveness of buffer gas cooling for different mass ratios we calculate the average of the energy spectrum of the ion. As a physical measure, the arithmetic mean comes close to the definition of a temperature, albeit the clearly non-thermal distribution. We show the arithmetic mean in Fig. 5.3 for the case $\frac{q^2}{a} = 50$. Although the arithmetic mean diverges for $\alpha \geq -1$, the energy spectrum can still be normalized for $\alpha < 0$. In this range the median

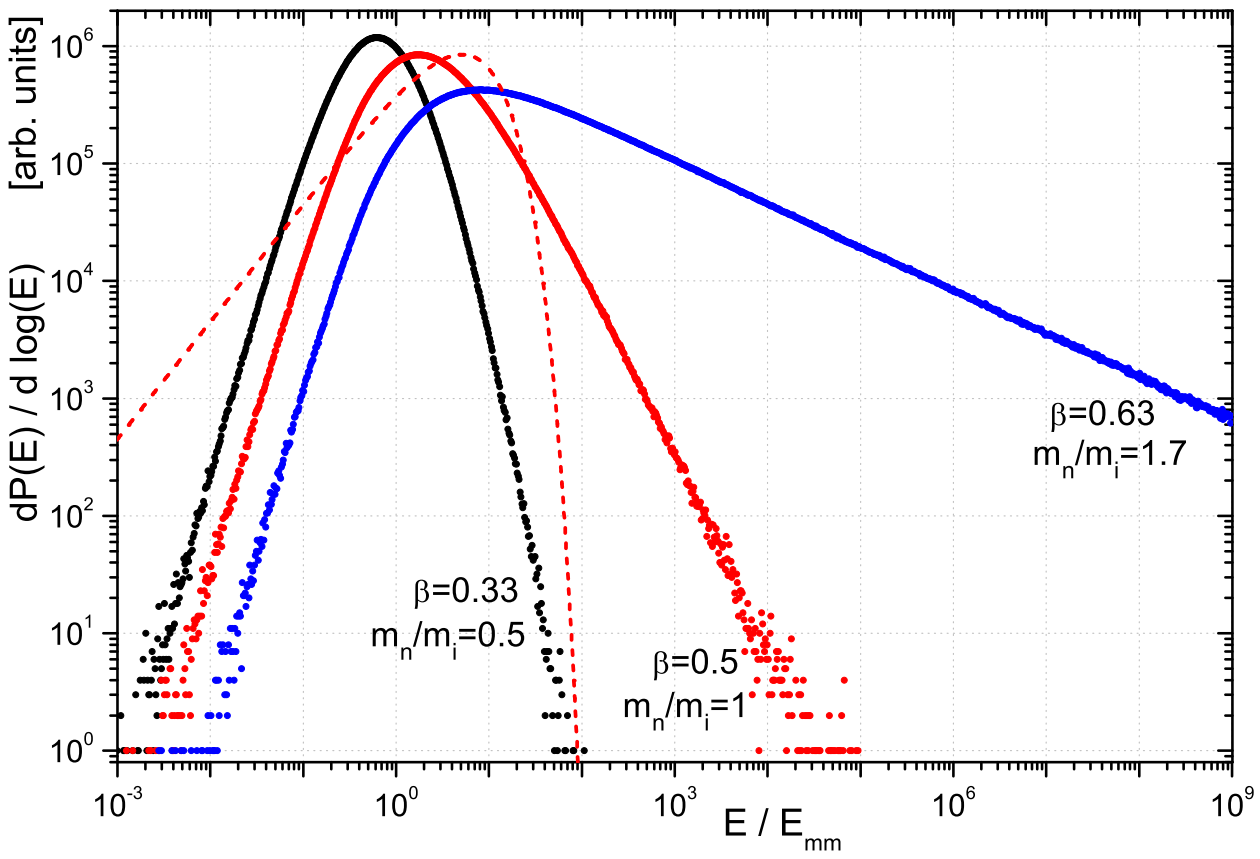

Figure 5.1: Energy spectra of the ion for three different mass ratios. 10^8 energies are sampled into logarithmically spaced bins with an energy resolution of 100 bins per decade. We choose $\Delta x = \Delta y$ and $c_z = 0$ and trap parameters $\frac{q^2}{a} = 50$. In the case where the ion mass is twice the neutral mass (black) the ion's mean energy is $0.8\,E_{mm}$, in the case for equal masses (red) $5\,E_{mm}$. The red dashed line corresponds to a thermal energy distribution with $5\,E_{mm}$. The spectrum for a lighter ion, $\frac{m_n}{m_i} = 1.7$ (blue), contains a significant contribution of very high energies, typically leading to quick ion loss due to finite trap depth.

continues to be a well defined statistical measure for the energy of the ion.

In experiments, a large probability density at high energies leads to a rapid ion loss due to a finite trap depth E_{td} [104, 103]. We have numerically evaluated the required trap depth E_{td} to limit the ion loss probability per collision to P_{loss} (Fig. 5.3). For large β we can approximate the required trap depth by $E_{td} = E_{mm}\ (P_{loss})^{1/\alpha}$. The results show that mass ratios with light neutrals are preferred for efficient buffer gas cooling. However, even for the heavy neutral scenario stable trapping and buffer gas cooling are possible for carefully chosen trap geometry, trap depth and micromotion compensation.

5.2.4 Higher Collision Rates

For all the results discussed so far the collision rate has been assumed very low, and as long as the condition $\Gamma \ll \omega$ is fulfilled the results remain unchanged. As the collision rate approaches

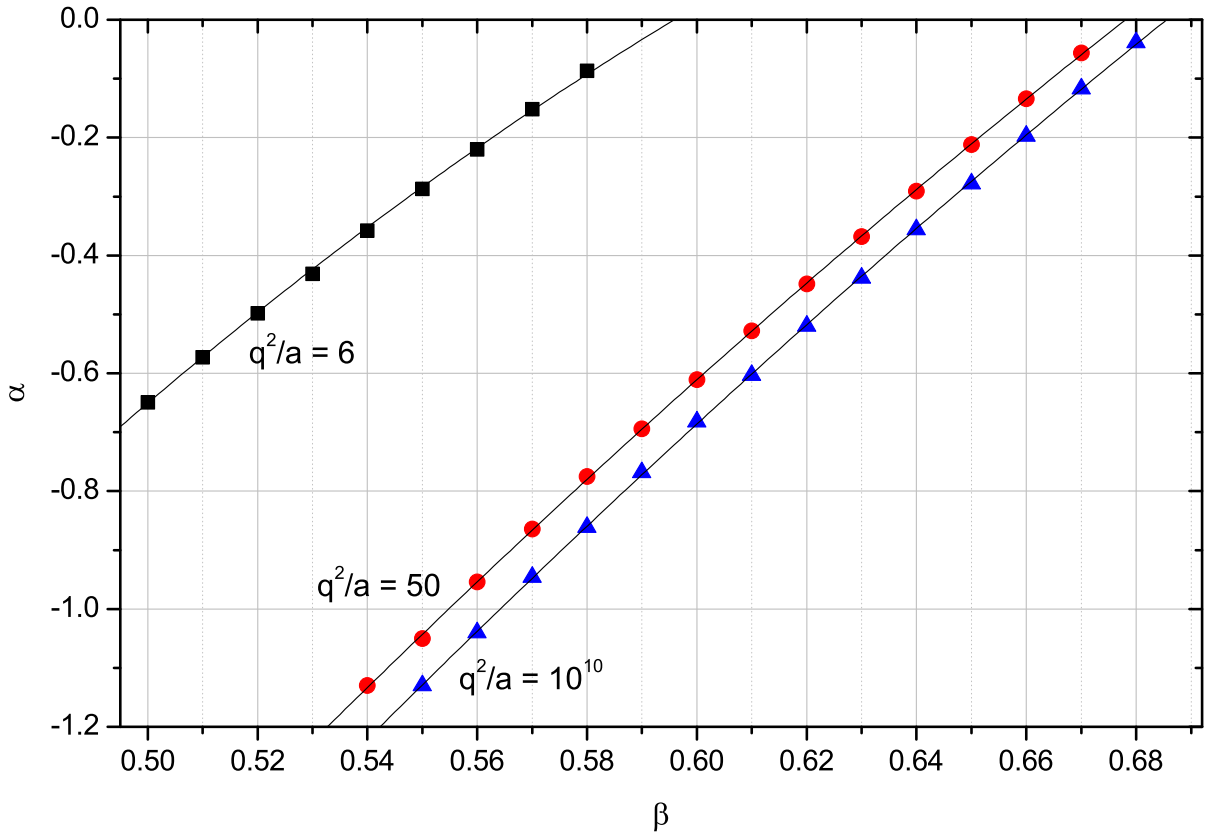

Figure 5.2: The exponents α obtained from fitting power laws to the high energy tails of the ion energy spectra are plotted against the mass ratio coefficient β. This is done for three different trap geometries, for a spherical trap ($\frac{q^2}{a} = 6$, black rectangles), for an elongated trap ($\frac{q^2}{a} = 50$, red circles) and for the extreme case with negligible axial confinement ($\frac{q^2}{a} = 10^{10}$, blue triangles). The data is fitted with second order polynomials to extrapolate to β_{crit} for which the exponent α becomes 0.

or even exceeds the trap frequency $\omega_{x,y}$, the probability to have consecutive collisions at correlated positions increases. Under this condition we observe a reduced median energy and an increased power law tail.

5.3 Quantum Scattering

Up to this point the classical Langevin model has been used to explore the ion's energy spectrum and its dependence on mass ratio, trap geometry and collision rates. Here we make use of a quantum mechanical description of the interaction process. The solution to the quantum mechanical scattering problem can be found by expanding the wavefunction into partial waves. In the regime where many partial waves contribute, the total elastic cross section scales like $E_c^{-1/3}$ [52]. The resulting energy dependent scattering rate and angular dependence lead to additional effects as compared to the Langevin model. These are necessary to explain

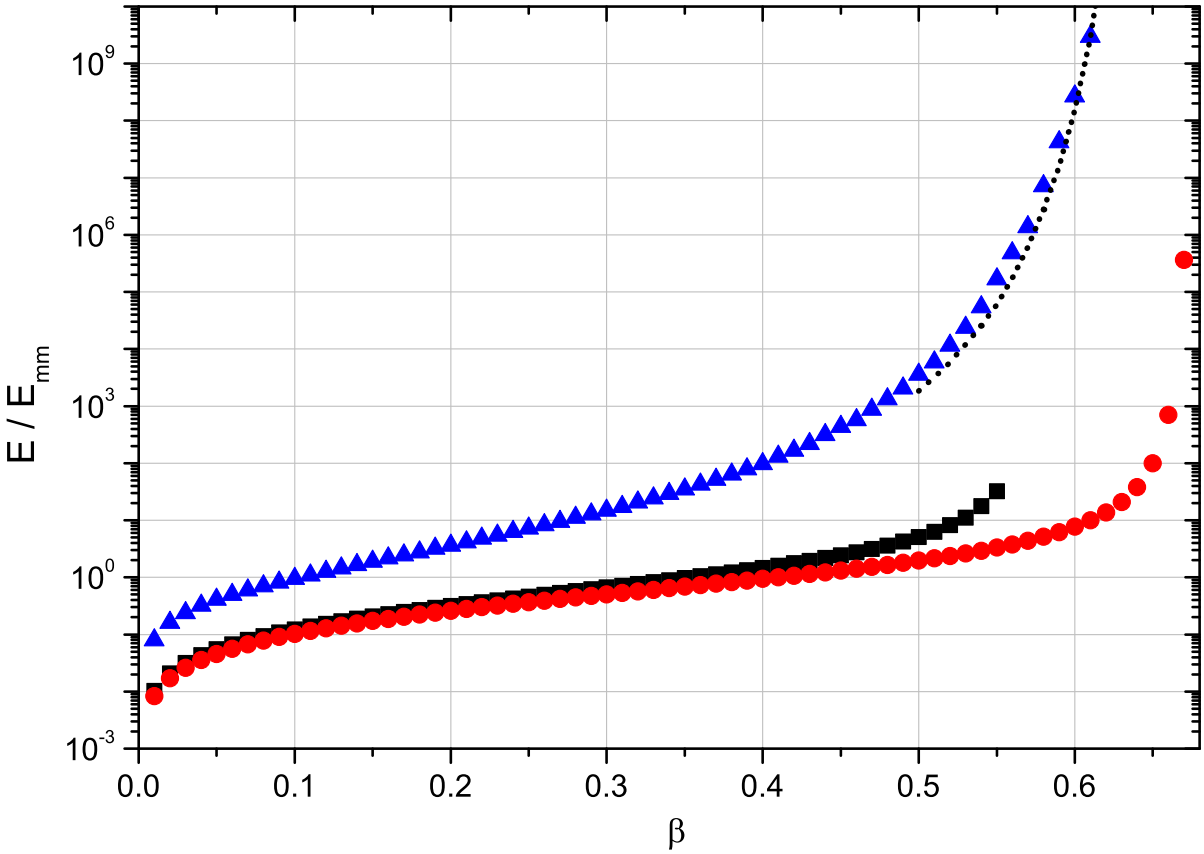

Figure 5.3: For different β the ion's arithmetic mean energy (black rectangles) and median energy (red circles) are shown in units of E_{mm}. The arithmetic mean is expected to diverge for $\beta > 0.554$. An example for the required trap depth for $P_{loss} < 10^{-5}$ is given (blue triangles) and compared to $E_{td} = E_{mm}\ (P_{loss})^{1/\alpha}$ (dotted line) using α obtained from power law fits to the tails of the energy spectra. All data are for $\frac{q^2}{a} = 50$.

the back-action on the neutral cloud, as observed in section 4.5.

We model the interaction potential by the long range polarization interaction of Eqn. (5.10) plus repulsion at short distances. The full differential cross-section is calculated using [108]

$$\frac{\mathrm{d}\sigma}{\mathrm{d}\Omega} = \frac{1}{k^2}\left|\sum_{l=0}^{\infty}(2l+1)\,e^{i\eta_l}\,\sin(\eta_l)\,P_l(\cos\theta)\right|^2 . \tag{5.12}$$

The angular momentum of a partial wave is $\hbar l$ and $\hbar k = \sqrt{2\mu E_c}$ is the collision momentum. The scattering phase η_l can be obtained by solving the radial Schrödinger equation which involves the centrifugal potential $\frac{\hbar^2\, l(l+1)}{2\mu R^2}$. The resulting centrifugal barrier increases in height with angular momentum ($\sim (\hbar l)^4$). Partial waves with $l < l_0 = 1/\hbar\sqrt{2\mu\sqrt{2C_4 E_c}}$ have a collision energy larger than the height of the centrifugal barrier, probe the deep potential well and are reflected from the hard core. The exact form of the potential, relevant to determine η_l, is typically not known. Therefore phase shifts η_l for $l < l_0$ are assumed to be uniformly

distributed within $[0, 2\pi)$ [45]. In this approximation each partial wave contributes with $\sigma_l = \frac{2\pi l}{k^2}$ to the total cross-section. Summing σ_l up to l_0 reproduces the Langevin cross-section.

The full cross-section includes additional contributions[4] from partial waves with $l > l_0$. As the centrifugal barrier is higher than the collision energy, these partial waves are scattered from the centrifugal barrier, if tunnelling effects are neglected. The phase shifts can be semiclassically approximated by [45, 52]

$$\eta_l = -\frac{\mu}{\hbar^2}\int_{R_0}^{\infty} \frac{V(R)}{\sqrt{k^2 - \frac{(l+1/2)^2}{R^2}}}\mathrm{d}R \tag{5.13}$$

with $R_0 = \frac{l+1/2}{k}$.

5.3.1 Modeling the Differential Cross-Section

The probability distribution for the deflection angle θ

$$I(\theta, E_c) = \frac{\mathrm{d}\sigma}{\mathrm{d}\theta} = \int_0^{2\pi} \frac{\mathrm{d}\sigma}{\mathrm{d}\Omega}\sin\theta\,\mathrm{d}\phi \tag{5.14}$$

is numerically calculated using Eqn. (5.12), Eqn. (5.13) and randomly distributed η_l for $l < l_0$. We sum Eqn. (5.12) for l up to 20000 and average over 100 different random sets of η_l. The differential cross-section calculated in this way depends on the reduced mass μ, the collision energy $E_c = \frac{\hbar^2 k^2}{2\mu}$ and C_4 only. For the case of a $^{174}\mathrm{Yb}^+$ ion colliding with a $^{87}\mathrm{Rb}$ atom, four probability distributions of the form Eqn. (5.14) are shown in Fig. 5.4. The main feature of $I(\theta, E_c)$ is a forward scattering peak, which gets more pronounced as the energy increases [54]. The integral of the differential cross-section reproduces the expected $E_c^{-1/3}$ energy dependence, and its magnitude is in agreement with [45].

To implement the differential cross-section in the Monte Carlo simulation a parameterization of the normalized $I(\theta, E_c)$ is used to create a function that returns a random θ for a given collision energy. The distribution $I(\theta, E_c)$ is modelled in four intervals using two power laws ($\propto \theta^p$), a flat top and a flat background. The parameters peak height, background offset and interval limits are energy dependent and are well approximated by power laws ($\propto E_c^{p'}$). These power laws are obtained from fits to differential cross-sections for more than 30 different energies E_c in the range between $k_B \times 1\,\mu\mathrm{K}$ and $k_B \times 100\,\mathrm{K}$. The θ-generating function uses these parameter functions and inverse transform sampling. Fig. 5.4b compares sampled output of the θ-generating function with the normalized differential cross-sections.

[4] In contrast to the quantum mechanical model, in a classical description the integral of these contributions diverges.

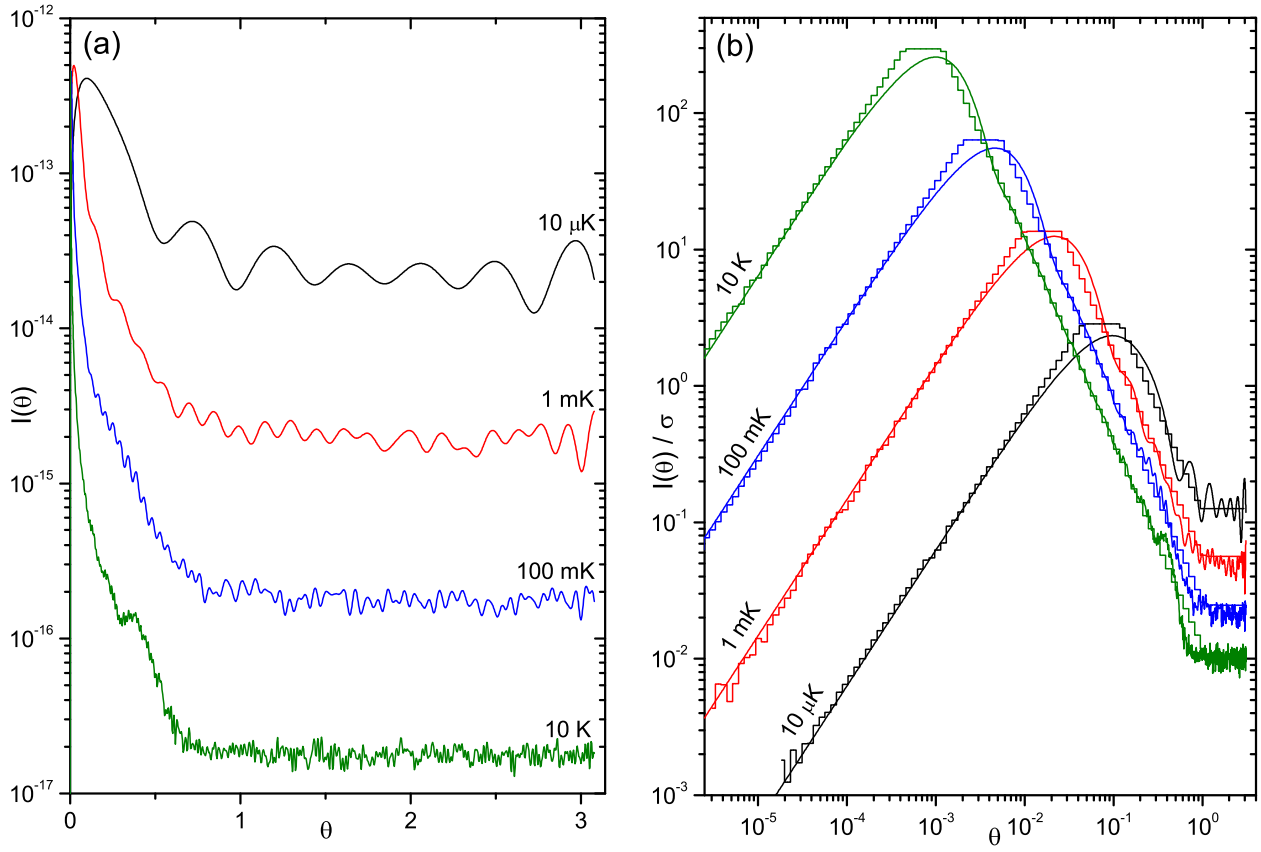

Figure 5.4: (a) The probability distributions $I(\theta, E_c)$ for the scattering angle θ in elastic collisions between $^{174}Yb^+$ and ^{87}Rb are numerically calculated. The unknown scattering phases for close encounters ($l < l_0$) are chosen randomly. The four curves are for different collision energies E_c. The forward scattering peak at small θ is more pronounced for higher energies. Its shape is emphasized in (b) where the scattering angle θ is displayed logarithmically. The normalized $I(\theta, E_c)$ (smooth lines) for the four different energies are compared with logarithmically binned output from the random θ-generating function (step like lines). The approximation is optimized to reproduce the height and position of the forward scattering peak.

5.3.2 Ion Energy Spectrum for Energy Dependent Scattering Rate

We have simulated the kinetics of the ion in an ultracold buffer gas using the parametrized differential cross-section to investigate how this affects the ion energy spectrum. Different from the Langevin case, the collision rate depends on the instantaneous ion energy. Therefore efficient simulation relies on the collision time sampling described in Appendix A. The ion energies are binned and weighted by the time the ion remains at the specific energy.

We have performed specific simulations for our ion trap with the frequencies $\omega_{x,y,z} = 2\pi \times \{151, 153, 42\}$ kHz, $\Omega_T = 2\pi \times 42.5$ MHz, excess micromotion parameters $\Delta x = \Delta y = 2\,\mu$m and neutral density $n = 10^{18}\,\mathrm{m}^{-3}$ for the system $^{174}Yb^+$ - ^{87}Rb, reproducing conditions comparable to the experiments described in section 4.4. We find good agreement with the previous results

from the Langevin model and conclude that the Langevin model is sufficient to describe the ion's energy statistics. Formally, however, the system does not necessarily scale only with the micromotion energy E_{mm} anymore, as the differential cross-section introduces its own energy scale. In the next section we will demonstrate that the full differential cross-section is necessary to predict effects on the cold neutral atoms.

5.3.3 Neutral cloud evolution

Ultracold neutral atomic clouds have atom numbers ranging up to 10^9. Compared to a room temperature buffer gas, this limited number of atoms and the good isolation from the environment allow the observation of collision effects on the neutral gas. The main observables are the number of neutral atoms N_a and their temperature T_a. In experiments, these values can be obtained from time-of-flight imaging and are suitable to verify the simulation model.

The back-action of the ion onto the neutral gas is a result of the energy transfer per collision. For general two-body elastic collisions it is given by

$$E_t = 4\,(1-\beta)\,E_c\,\sin^2(\theta/2)\;, \tag{5.15}$$

depending on the scattering angle θ. For very small deflections $\theta \ll 1$, resulting from the forward scattering peak in the differential cross-section, only very little energy is transferred to the neutral atom. The distribution of transferred energies E_t, shown in Fig. 5.5, can be understood as a convolution of the collision energy distribution and the energy dependent differential cross-section.

Fig. 5.5 also shows distributions for E_c and E_t obtained using the Langevin model for comparison. The Langevin collision rate is obviously smaller, explained by the different energy dependence of the cross-sections, $\sigma_L \propto E_c^{-1/2}$ vs $\sigma \propto E_c^{-1/3}$. The semiclassical distribution of E_c is also slightly shifted towards higher energies with respect to the Langevin E_c, since collisions are more likely to happen at higher energies. The transferred energies differ only little between to two models for $E_t \gtrsim k_B \times 0.03\,\mathrm{K}$. This reflects the statement that the ion's mobility is well described by Langevin type collisions. However, the significant peak at low E_t of the semiclassical distribution causes most of the effects on the cold neutral gas.

So far all the results were obtained assuming a uniform density distribution of neutral atoms. This will now be replaced by a spatial distribution for a thermal gas in a harmonic trap with temperature T_a and atom number N_a. Considering a finite trap depth $E_{td,a}$ for the neutral atoms, every collision with $E_t > E_{td,a}$ will lead to an atom loss, whereas every $E_t < E_{td,a}$ will increase the temperature T_a. The simplified model used in the simulation assumes immediate thermal equilibration of the neutral gas. Then a collision with $E_t < E_{td,a}$ simply increases T_a by $\frac{E_t}{3\,k_B\,N_a}$. The loss of an atom for $E_t > E_{td,a}$ will decrease N_a by 1 but also

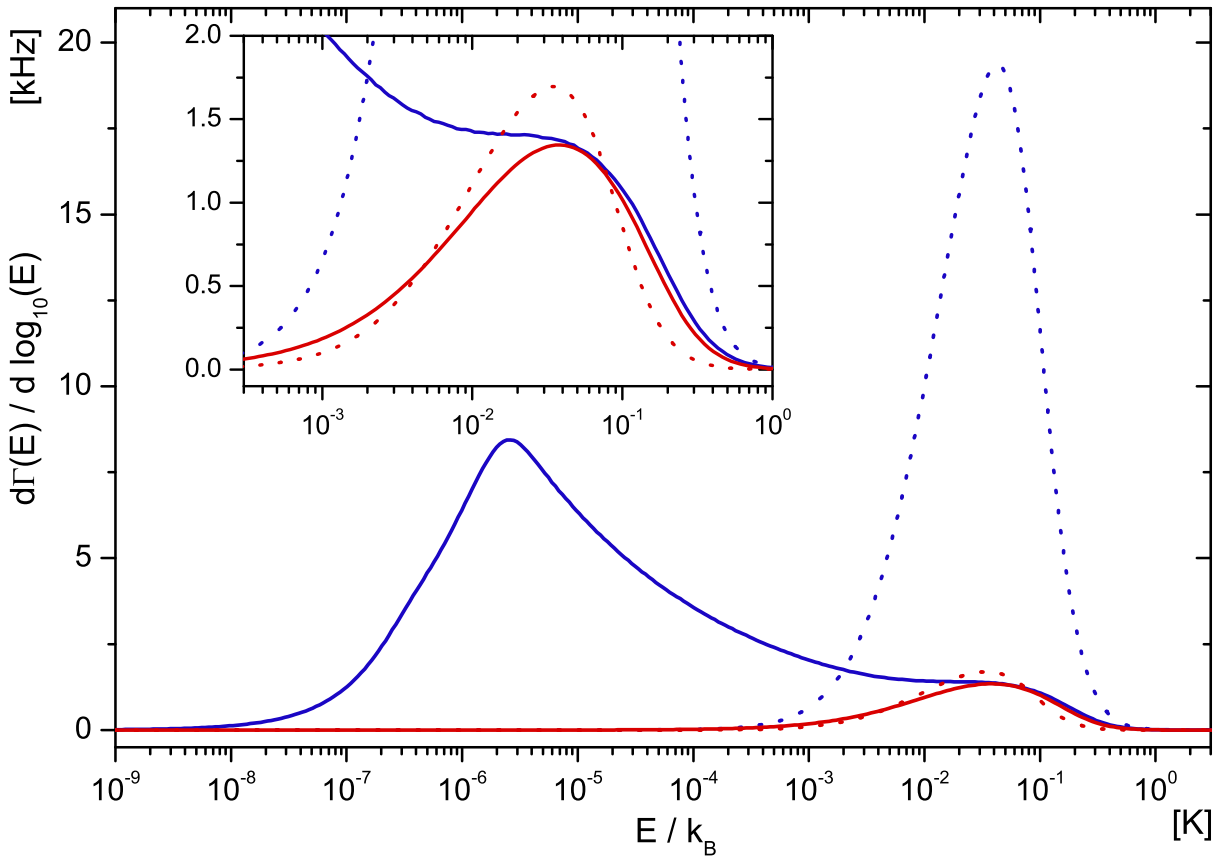

Figure 5.5: Distributions of collision energy E_c (dotted line) and transferred energy E_t (solid line). The data are obtained by binning 10^8 collisions on a logarithmic energy scale, comparing Langevin scattering (red) with the full semiclassical differential cross-section (blue). The vertical axis indicates the scattering rate in kHz per decade of energy at which collisions with the specific energies occur. The inset is a magnification of the region relevant for Langevin scattering. The settings for this simulation run are $n = 10^{18}\,\mathrm{m}^{-3}$ for the uniform neutral atom density and $\Delta x = \Delta y = 2\,\mu\mathrm{m}$. Note the similarity between the two models for large and the significant difference for small transferred energies E_t.

affect the temperature depending on the atom's energy. The new temperature is calculated

$$T_{a,f} = \frac{N_{a,i}\,3\,k_B\,T_{a,i} - \frac{3}{2}\,k_B\,T_{a,i} - E_{pot}(\vec{r})}{(N_{a,i}-1)\,3\,k_B} \tag{5.16}$$

using the total energy of the neutral cloud, and the potential and average kinetic energy of the lost atom known from the position $\vec{r}$ of the collision. This can lead to evaporative cooling or heating effects depending on the position of the ion in the neutral gas.

For ion trajectories larger than the size of the buffer gas the ion can only collide in the centre of the trap where its motional energy is mostly related to the secular motion rather than the micromotion. This suppresses the power law tail of the ion energy distribution and reduces the ion's average energy. Hence, using tight traps to confine the neutral atoms might

help to overcome the constraints on ion trap depth, trap geometry and mass ratio.

5.3.4 Comparison to Experimental Data

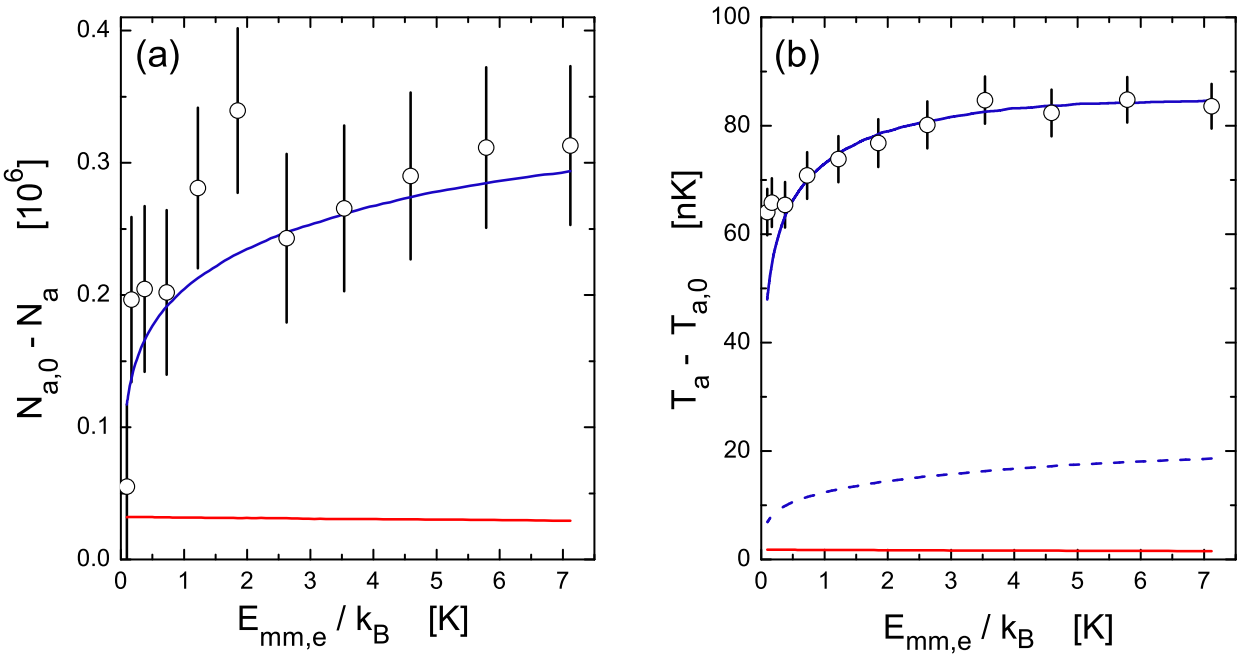

Figure 5.6: Comparison between experimental measurements (black circles) and the simulation predictions for neutral atom loss (a) and the neutral temperature increase (b). The semiclassical model (blue) fits the data well. The Langevin model (red) systematically underestimates the collision effects on the neutral atoms. The contribution of evaporative heating (Eqn. (5.16)) in the semiclassical model is indicated with the blue dashed line. The experimental data is from a measurement as described in section 4.5.

Here we compare the simulation predictions for the effects on neutral atoms with experimental data from $Yb^+ - Rb$ as described in section 4.5. The measured quantities are the loss of neutral atoms and temperature increase of a cold thermal cloud, after 8 s of interaction and for different excess-micromotion energies $E_{mm,e}$. Fig. 5.6 displays the data together with the simulation results.

Initial conditions for the neutral ^{87}Rb cloud in the simulation are given by $T_{a,0} = 250\,\mathrm{nK}$ and $N_{a,0} = 2.25 \cdot 10^6$. Neutral trap frequencies of $2\pi \times \{28, 28, 8\}\,\mathrm{Hz}$ result in an initial central density of $n(0) = 1.9 \cdot 10^{18}\,\mathrm{m}^{-3}$. The neutral trap depth is $E_{td,a} = k_B \cdot 8\,\mu\mathrm{K}$.

A single $^{172}Yb^+$ ion is trapped with parameters given in section 5.3.2. The excess micromotion parameters Δx and Δy are varied between 0 and 15 μm, and additionally there is micromotion along the trap symmetry axis with $c_z = 2\,\mu\mathrm{m}$. The excess-micromotion energy scale, $E_{mm,e}/k_B$ thus ranges from 90 mK to 7 K.

The simulation with the semiclassical cross-section predicts both the shape and the magnitude of the experimental results well. In contrast, the Langevin scattering is not suited to model these measurements because the ultracold atoms are highly sensitive to small energy

transfer E_t. They correspond to collisions with small deflection angles, which are neglected by the Langevin model, cf. Fig. 5.5.

Conclusion

In the course of this work we have been successful in combining a single trapped ion with a Bose-Einstein condensate for the first time. The ion is trapped by electric fields while the atoms are confined by magnetic fields or in an optical dipole trap. The resulting independent control over the two partite systems has been demonstrated. Relative positioning and motion is achieved by displacing one or the other trap centre. The average collision energy can be tuned by adding excess micromotion.

In our system of a Yb^+ ion being immersed in a Bose-Einstein condensate of ^{87}Rb elastic collisions are the dominating interaction process. They lead to sympathetic cooling of the ion by the ultracold neutral gas. After collisions, the neutral atoms can either be lost from their trap or, when having acquired only a small amount of kinetic energy, contribute to a temperature increase of the neutral cloud. These two effects can both be measured and they carry the mark of the differential cross-section. Due to the extremely low temperature of the neutral gas, we are highly sensitive to very small energy transfers appearing in forward scattering events which are typically not observed in other ion-neutral collision experiments. Inelastic processes have been measured to occur at rates a factor of 10^5 lower than the elastic ones. We have identified radiative and non- radiative charge exchange.

Physical models allow us to reach a better understanding of the relevant processes from the experimentally made observations. Monte-Carlo methods are well suited to model the interaction between a trapped ion and a neutral gas. By using such methods, we now understand the role of the ion-atom mass ratio, the excess micromotion, and the differential cross-section in great detail. Finding the numerical simulation results in good agreement with the experimental observations allows us to confidently make predictions about possible effects, such as cooling of the neutral gas by collisions with the ion.

In contrast to usual ion trapping experiments, where the repetition rate can be on the order of 100 cycles per second, with the Bose-Einstein condensate our repetition rate is reduced to about one cycle per minute. Working with a single ion thus makes the acquisition of statistically significant data demanding. Only a high degree of automization of continuous calibration and data acquisition processes allows a consequent measurement procedure. In our system this involves the automatic reload of single ions, continuous electric offset field compensation and laser frequency adjustment by spectroscopy on the single ion.

The available controls in our hybrid system are both a virtue and a challenge. On one

side they can allow for example the local probing or manipulation of a quantum gas. On the other side, they are challenging to be controlled, on a technical level, to achieve the necessary precision in the positioning or energy resolution. Future technical improvements are likely to expand the range of available collision energies to even lower values. This, in return, should allow to investigate coherent interaction processes between atoms and ions.

Appendix A

Collision Time Sampling

[1]A scattering rate Γ sets the probability for a collision to take place within a time interval $\mathrm{d}t$. In our case

$$\Gamma(t) = n(\vec{x})\,\sigma(E_c)\,v_{ion}(t) \tag{A.1}$$

with n being the neutral atom density, σ the cross-section and v_{ion} the velocity of the ion as defined in Eqn. (5.6). Usually the density is a function on the ion's position, the cross-section depends on the collision energy and v_{ion} oscillates rapidly in time, leading to a $\Gamma(t)$ with non-trivial time dependence. In the following we explain the method used to randomly generate collision times t with the exact distribution defined by $\Gamma(t)$.

In general, the process of an event (collision) taking place with a rate $\Gamma(t)$ can be modelled using a differential equation for the probability $Q(t)$ that the event has not yet happened after the time t,

$$\mathrm{d}Q(t) = -\Gamma(t)\,Q(t)\,\mathrm{d}t\ . \tag{A.2}$$

The probability distribution for an event to take place after the time t is defined by $P(t) = -\mathrm{d}Q/\mathrm{d}t$. In the simple case with constant $\Gamma(t) = \Gamma_0$ the solution is

$$P_{\Gamma_0}(t) = \Gamma_0\ \exp(-\Gamma_0\,t) \tag{A.3}$$

and a random time can be obtained using inverse transform sampling,

$$t = -1/\Gamma_0\ \log(r) \tag{A.4}$$

with r being a uniformly distributed random number in the interval $(0, 1]$. For time dependent $\Gamma(t)$ the analytic solution for the probability distribution function is

$$P(t) = \Gamma(t)\ \exp\Big(-\int_0^t \Gamma(t_1)\,\mathrm{d}t_1\Big)\ . \tag{A.5}$$

[1]Permission to reproduce this Appendix from [101] has been granted by IOP Publishing Ltd.

Non-trivial time dependence of $\Gamma(t)$ usually requires a numerical approach to sample t from Eqn. (A.5). One straight-forward method would be to discretize time into small steps, calculate $\Gamma(t)$ and its contribution to $P(t)$ for every step, thereby numerically integrating the function $P(t)$ up to a randomly chosen trigger value, at which point the event takes place.

However, another method is employed here, which proves to be much faster and does not suffer from discretization errors. It works for $\Gamma(t)$ that have an upper bound $\Gamma_m = \sup(\Gamma(t))$, or where such a condition can be enforced by introducing a cutoff. In the specific case of the trapped ion, all factors in Eqn. (A.1) are easily limited by considering the energies E_j defining the trajectory and the excess micromotion parameters and using the peak neutral density. This upper bound can be adjusted after each collision event having affected E_j or $n(\vec{x})$.

The algorithm works by advancing the system by a time t according to Eqn. (A.4) with $\Gamma_0 = \Gamma_m$. Then the rescaled rate

$$\gamma(t) = \Gamma(t)/\Gamma_m \tag{A.6}$$

is calculated for the resulting state of the system after the time t and an event takes place if $\gamma(t) > r$, with r being another uniformly distributed random number in the interval $[0, 1)$. If the event does not take place ($\gamma(t) \leq r$) the algorithm iteratively loops back to advance the system by an additional t, again according to Eqn. (A.4). The method is exact in that it reproduces the probability distribution function Eqn. (A.5). A proof follows below. The efficiency of the method is the ratio of the average of $\Gamma(t)$ and Γ_m, $\epsilon = \langle\Gamma(t)\rangle/\Gamma_m = \langle\gamma(t)\rangle$. This means that in order to generate N events it can be expected that $\Gamma(t)$ needs to be evaluated N/ϵ times.

Proof: We start from writing an expression for the probability distribution function $P_s(t)$ obtained with the suggested method. Since the final t can be the result of any number of iterations, $P_s(t)$ is a sum of all these possibilities, $P_s(t) = P_{s,1} + P_{s,2} + P_{s,3} + \ldots$, where $P_{s,i}$ is the probability that t results as the time of event after i iterations. The first few terms are given below.

$$P_{s,1} = \gamma(t)\, P_{\Gamma_m}(t) \tag{A.7}$$

$$P_{s,2} = \gamma(t) \int_0^t P_{\Gamma_m}(t_1)\, P_{\Gamma_m}(t - t_1) \big(1 - \gamma(t1)\big)\, \mathrm{d}t_1 \tag{A.8}$$

$$P_{s,3} = \gamma(t) \int_0^t \int_0^{t_1} P_{\Gamma_m}(t_2)\, P_{\Gamma_m}(t_1 - t_2)\, P_{\Gamma_m}(t - t_1) \big(1 - \gamma(t_1)\big) \big(1 - \gamma(t_2)\big)\, \mathrm{d}t_2\, \mathrm{d}t_1 \tag{A.9}$$

Note that the products of P_{Γ_m} (as defined in Eqn. (A.3)) in the integrals always combine to

$\Gamma_m^{(i-1)} P_{\Gamma_m}(t)$. Therefore $P_{\Gamma_m}(t)$ is taken out of the sum as a common prefactor,

$$P_s(t) = \gamma(t)\, P_{\Gamma_m}(t)\Big(1 + \Gamma_m \int_0^t \big(1-\gamma(t1)\big)\,\mathrm{d}t_1 + {\Gamma_m}^2 \int_0^t \int_0^{t_1} \big(1-\gamma(t_1)\big)\big(1-\gamma(t_2)\big)\,\mathrm{d}t_2\,\mathrm{d}t_1 + \dots\Big)\,. \quad \text{(A.10)}$$

Now the upper boundaries of all the partial integrals can be set equal to t, since they only induce ordering to the time series $\{t_1, t_2, \dots, t_n\}$. This rescales the terms by the number of possible orderings ($n!$). Then the partial integrals reduce to a single integral to the power of n,

$$\begin{aligned}\int_0^t \int_0^{t_1} \dots \int_0^{t_{n-1}} \big(1-\gamma(t_1)\big)\big(1-\gamma(t_2)\big)\dots\big(1-\gamma(t_n)\big)\,\mathrm{d}t_n \dots \mathrm{d}t_2\,\mathrm{d}t_1 \\ = \frac{1}{n!}\int_0^t \int_0^t \dots \int_0^t \big(1-\gamma(t_1)\big)\big(1-\gamma(t_2)\big)\dots\big(1-\gamma(t_n)\big)\,\mathrm{d}t_n \dots \mathrm{d}t_2\,\mathrm{d}t_1 \\ = \frac{1}{n!}\Big(\int_0^t \big(1-\gamma(t_1)\big)\,\mathrm{d}t_1\Big)^n\,. \quad \text{(A.11)}\end{aligned}$$

Combining this with Eqn. (A.10) gives

$$\begin{aligned}P_s(t) = \gamma(t)\, P_{\Gamma_m}(t) \sum_{n=0}^{\infty} \frac{{\Gamma_m}^n}{n!}\Big(\int_0^t \big(1-\gamma(t_1)\big)\,\mathrm{d}t_1\Big)^n \\ = \gamma(t)\, P_{\Gamma_m}(t) \exp\Big(\Gamma_m \int_0^t \big(1-\gamma(t_1)\big)\,\mathrm{d}t_1\Big)\,, \quad \text{(A.12)}\end{aligned}$$

and it follows with Eqn. (A.3) and Eqn. (A.6)

$$\begin{aligned}P_s(t) = \gamma(t)\,\Gamma_m \exp\Big(-\Gamma_m t + \Gamma_m \int_0^t \big(1-\gamma(t_1)\big)\,\mathrm{d}t_1\Big) \\ = \Gamma(t) \exp\Big(-\int_0^t \Gamma(t_1)\,\mathrm{d}t_1\Big)\,. \quad \text{(A.13)}\end{aligned}$$

This is identical to Eqn. (A.5) which proves that the method reproduces the exact probability distribution.

Appendix B

Structure of the Simulation Loop

[1]The following is a short description of how the main simulation loop has been implemented.

1) setup system configuration: ω_j, Ω_T and excess micromotion, β, neutral trap frequencies, T_a, N_a, $n(\vec{x})$, $\frac{\mathrm{d}\sigma}{\mathrm{d}\Omega}$, ...

2) select initial state $(E_j, \varphi_j)_{j\in\{x,y,z\}}$

3) calculate maximal collision rate Γ_m, considering $n_{max}(T_a, N_a)$ and E_j

4) increment time t by Eqn. (A.4)

5) calculate ion position and velocity,
using Eqn. (5.4),(5.5),(5.6), $(E_j, \varphi_j, t) \rightarrow (\vec{r}_{ion}, \vec{v}_{ion})$

6) calculate $\gamma(t)$ with Eqn. (A.6),
proceed to 7) with probability $\gamma(t)$,
else go back to 4)

7) choose collision parameters (θ, ϕ) according to $\frac{\mathrm{d}\sigma}{\mathrm{d}\Omega}$

8) update neutral atom parameters T_a, N_a,
using Eqn. (5.15),(5.16) and $E_{td,a}$

9) apply scattering Eqn. (5.7) to $\vec{v}_{ion}$

10) calculate new trajectory parameters,
using Eqn. (5.4),(5.5),(5.6), $(\vec{r}_{ion}, \vec{v}_{ion}, t) \rightarrow (E_j, \varphi_j)$

11) loop back to 3)

The setup of the system configuration in 1) contains mainly parameters which do not change during the collisions, such as trap frequencies or the atom-ion mass ratio. Exceptions

[1]Permission to reproduce this Appendix from [101] has been granted by IOP Publishing Ltd.

are the neutral atom number N_a and temperature T_a, which act as initial conditions. The initial state for the ion energy in `2)` is mostly unimportant, as the simulation will iterate over many collisions and the information of the initial state is lost after a few collisions. When looking at steady state statistics of the ion energy, the values after the first few collisions can simply be ignored, thus effectively letting the system evolve for a short time before measuring its properties. The points `3)` to `7)` implement the collision time sampling algorithm described in Appendix A. The maximally possible collision rate Γ_m is calculated from the peak density $n_{max}(T_a, N_a)$ of the neutral atoms and from the maximum value of $\sigma(E_c)\, v_{ion}(t)$. The latter is limited by the highest possible ion velocity, which depends on the secular energy E_j and the excess micromotion. The calculation of $\gamma(t)$ in `6)` uses the $\vec{v}_{ion}$ and $\vec{r}_{ion}$ obtained in `5)` to determine $\Gamma(t)$ with Eqn. (5.9). If a collision takes place at the chosen time t, `7)` gives the scattering angles according to the differential cross-section. `8)` simulates the back-action on the neutral atoms. `9)` modifies the velocity of the ion. In `10)` the new trajectory parameters E_j and φ_j are determined, to represent the motion of the ion up to the next collision.

Information on any system parameter can be retrieved at user-defined points within the simulation loop. The ion energy is typically registered after `10)`, the collision and transferred energies, E_c and E_t after `8)`. Random sampling is used in `4)` and `6)`, to determine the time of collision, and in `7)`, for the scattering angles.

Appendix C

Material Properties

Table C.1: Metal properties, for metals used in ion trap setup

	Copper [109]	Stainless Steel 304 [110]	Vespel SP1 [111]
Density [g/cm^3]	8.96	7.9	1.43
Specific Heat [J/kg/K]	384.6	500	-
Thermal Conductivity [W/m/K]	401	15	0.287
Thermal Expansion Coefficient [K^{-1}]	$16.5 \cdot 10^{-6}$	$16 \cdot 10^{-6}$	$50 \cdot 10^{-6}$
Electrical Resistiviy [Ω m]	$16.78 \cdot 10^{-9}$	$0.73 \cdot 10^{-6}$	$10^{12} - 10^{13}$

Table C.2: Selected ceramics properties [112]

	Shapal-M Soft	MACOR	Boron Nitride Grade AX05
Dielectric Strength [kV/mm]	40	40	40
Resistivity [Ω cm]	10^{12}	10^{14}	$> 10^{14}$
Loss tangent	0.001 @1 MHz	0.007 @8.6 GHz	0.001 @8.8 GHz
ϵ_r	7.1	5.68	4.0
Density [g/cm^3]	2.9	2.52	1.85
Specific Heat [J/kg/K]	790	790	350
Thermal Conductivity [W/m/K]	90	1.7	78
Thermal Expansion Coefficient	$4.4\,10^{-6}$ K^{-1}	$9.4\,10^{-6}$ K^{-1}	$1.0\,10^{-6}$ K^{-1}
Max Use Temperature	2200 K	1300 K	1150 K
Porosity	-	-	12.57%
Vickers Hardness [kg/mm^2]	390	230	15-24

Acknowledgements

Here, I would like to thank all the people who supported and helped me during the last years. Without them, the work of this PhD course and the good times I had would not have been possible in the same way.

First of all, I would like to thank my supervisor Michael Köhl for giving me the opportunity to work on the ion-BEC experiment. His idea for this setup, the dedication to the project and the time he spent working with us in the lab have allowed our experiment to be set up and successfully running within such a short time. The discussions with him about the observed physics have greatly helped me in understanding not only the details and background of our physical system, but also about scientific processes and methods in general. Also, the fact that he has been available for questions or discussions in and around the lab at almost any time is exceptional and hardly to outperform.

Also, I thank Stefan Palzer, Carlo Sias and Lothar Ratschbacher, who worked with me on the same project. Stefan Palzer, fellow PhD student, worked with me from when I arrived in Cambridge in June 2007 until the end of 2009. We shared a lot of good moments in the lab, such as the creation of the first MOT, the first BEC, and trapping our first ion. His design of the Yb Laser system and the effort to keep it running during the measurements have been crucial for the whole project. Carlo Sias, our Postdoc since the beginning of 2008, has handled a major part of work related to the neutral atoms. With a lot of endurance, he optimized our BEC system to achieve the best possible result. I also enjoyed the many inspiring discussions we had, which always lead to some kind of improvement of physical understanding. Lothar Ratschbacher has joined our team in 2009. His enthusiasm for the project and to understand every detail of the experiment, including electronics and software, have lead to many significant improvements, such as increased photon detection efficiency and enhancements of automization. With his communicative way, it is always a pleasure to work with him in the same team.

For the friendly and helpful atmosphere in our student office I would also like to thank Bernd Fröhlich, Micheal Feld, Enrico Vogt and Alexander Beck. I feel lucky to not only have worked next to, but also having spent some free time with them, and getting along well with all of them has made the last years even more enjoyable.

Thanks also to Pam Hadder, our group secretary, who has been a big help in numerous cases when dealing with suppliers, or also with more general, administrative matters. Her

kind and prompt advice has relieved me many times from such administrative tasks, which otherwise could have consumed a lot of my time.

I thank the workshop of the Cavendish Laboratory, Terry Stubbings, and Nigel Palfrey, for their commitment in manufacturing many of the special mechanical parts for our setup, and for their advice and help on how to use some of the machines myself. Also, I am grateful to Maurice Goodrick and his team for the advice in printed-circuit-board assembly and soldering, and for allowing me to use their facilities.

I am grateful for funding support from the Overseas Research Studentship (ORS) award.

Especially, I would like to thank my parents and Rebecca, who patiently and continuously supported me during my time here in Cambridge.

Bibliography

[1] M.H. Anderson, J.R. Ensher, M.R. Matthews, C.E. Wieman, and E.A. Cornell. Observation of Bose-Einstein condensation in a dilute atomic vapor. *Science*, 269:198, 1995.

[2] K. B. Davis, M. O. Mewes, M. R. Andrews, N. J. van Druten, D. S. Durfee, D. M. Kurn, and W. Ketterle. Bose-einstein condensation in a gas of sodium atoms. *Phys. Rev. Lett.*, 75(22):3969–3973, Nov 1995.

[3] C. Raman, M. Köhl, R. Onofrio, D. S. Durfee, C. E. Kuklewicz, Z. Hadzibabic, and W. Ketterle. Evidence for a critical velocity in a Bose-Einstein condensed gas. *Phys. Rev. Lett.*, 83:2502, September 1999.

[4] K. W. Madison, F. Chevy, W. Wohlleben, and J. Dalibard. Vortex formation in a stirred Bose-Einstein condensate. *Phys. Rev. Lett.*, 84:806, January 2000.

[5] M. R. Andrews, C. G. Townsend, H.-J. Miesner, D. S. Durfee, D. M. Kurn, and W. Ketterle. Observation of interference between two Bose condensates. *Science*, 275(5300):637–641, 1997.

[6] I. Bloch, T. W. Hänsch, and T. Esslinger. Measurement of the spatial coherence of a trapped Bose gas at the phase transition. *Nature*, 403:166, January 2000.

[7] Immanuel Bloch, Jean Dalibard, and Wilhelm Zwerger. Many-body physics with ultracold gases. *Rev. Mod. Phys.*, 80:885, 2008.

[8] M. Greiner, O. Mandel, T. Esslinger, T.W. Hänsch, and I. Bloch. Quantum phase transition from a superfluid to a Mott insulator in a gas of ultracold atoms. *Nature*, 415:39, 2002.

[9] Iulia Buluta and Franco Nori. Quantum simulators. *Science*, 326(5949):108–111, 2009.

[10] Ferdinand Brennecke, Tobias Donner, Stephan Ritter, Thomas Bourdel, Michael Köhl, and Tilman Esslinger. Cavity QED with a Bose-Einstein condensate. *Nature*, 450(7167):268, Nov 2007.

[11] Yves Colombe, Tilo Steinmetz, Guilhem Dubois, Felix Linke, David Hunger, and Jakob Reichel. Strong atom–field coupling for Bose–Einstein condensates in an optical cavity on a chip. *Nature*, 450(7167):272–276, 2007.

[12] E. Fischer. Die dreidimensionale Stabilisierung von Ladungsträgern in einem Vierpolfeld. *Z. Phys.*, 156:1–26, 1959.

[13] W. Paul. Electromagnetic traps for charged and neutral particles. *Rev. Mod. Phys.*, 62(3):531–540, Jul 1990.

[14] R. Blatt, P. Gill, and R.C. Thompson. Current perspectives on the physics of trapped ions. *Journal of Modern Optics*, 39:193–220(28), 1992.

[15] T. Rosenband, D. B. Hume, P. O. Schmidt, C. W. Chou, A. Brusch, L. Lorini, W. H. Oskay, R. E. Drullinger, T. M. Fortier, J. E. Stalnaker, S. A. Diddams, W. C. Swann, N. R. Newbury, W. M. Itano, D. J. Wineland, and J. C. Bergquist. Frequency ratio of Al^+ and Hg^+ single-ion optical clocks; Metrology at the 17th decimal place. *Science*, 319(5871):1808–1812, MAR 28 2008.

[16] J. I. Cirac and P. Zoller. Quantum computations with cold trapped ions. *Phys. Rev. Lett.*, 74(20):4091–4094, May 1995.

[17] A. M. Steane and D. M. Lucas. Quantum Computing with Trapped Ions, Atoms and Light. *Fortschritte der Physik*, 48:839–858, 2000.

[18] R. Blatt and D.J. Wineland. Entangled states of trapped atomic ions. *Nature*, 453:1008–1014, 2008.

[19] C. Monroe, D. M. Meekhof, B. E. King, W. M. Itano, and D. J. Wineland. Demonstration of a fundamental quantum logic gate. *Phys. Rev. Lett.*, 75(25):4714–4717, Dec 1995.

[20] D. Leibfried, B. DeMarco, V. Meyer, D. Lucas, M. Barrett, J. Britton, W. M. Itano, B. Jelenković, C. Langer, T. Rosenband, and D. J. Wineland. Experimental demonstration of a robust, high-fidelity geometric two ion-qubit phase gate. *Nature*, 422:412–415, Mar 2003.

[21] F. Schmidt-Kaler, H. Häffner, M. Riebe, S. Gulde, G. P. T. Lancaster, T. Deuschle, C. Becher, C. F. Roos, J. Eschner, and R. Blatt. Realization of the Cirac-Zoller controlled-NOT quantum gate. *Nature*, 422:408–411, March 2003.

[22] M. Riebe, K. Kim, P. Schindler, T. Monz, P. O. Schmidt, T. K. Körber, W. Hänsel, H. Häffner, C. F. Roos, and R. Blatt. Process tomography of ion trap quantum gates. *Phys. Rev. Lett.*, 97(22):220407, Dec 2006.

[23] J. P. Home, D. Hanneke, J. D. Jost, J. M. Amini, D. Leibfried, and D. J. Wineland. Complete Methods Set for Scalable Ion Trap Quantum Information Processing. *Science*, 325:1227–, Sep 2009.

[24] O.P. Makarov, R. Côté, H. Michels, and W.W. Smith. Radiative charge-transfer lifetime of the excited state of $NaCa^+$. *Phys. Rev. A*, 67(4):042705, 2003.

[25] A. J. Daley, P. O. Fedichev, and P. Zoller. Single-atom cooling by superfluid immersion: A nondestructive method for qubits. *Phys. Rev. A*, 69(2):022306, 2004.

[26] Corinna Kollath, Michael Köhl, and Thierry Giamarchi. Scanning tunneling microscopy for ultracold atoms. *Phys. Rev. A*, 76(6):063602, 2007.

[27] C. Zipkes, S. Palzer, C. Sias, and M. Köhl. A trapped single ion inside a Bose-Einstein condensate. *Nature*, 464:388, 2010.

[28] C. Zipkes, S. Palzer, L. Ratschbacher, C. Sias, and M. Köhl. Cold heteronuclear atom-ion collisions. *Phys. Rev. Lett.*, 105(13):133201, Sep 2010.

[29] Marko Cetina, Andrew Grier, Jonathan Campbell, Isaac Chuang, and Vladan Vuletić. Bright source of cold ions for surface-electrode traps. *Phys. Rev. A*, 76(4):041401, Oct 2007.

[30] S. Schmid, A. Härter, and J. Hecker-Denschlag. Dynamics of a cold trapped ion in a Bose-Einstein condensate. *Phys. Rev. Lett.*, 105(13):133202, Sep 2010.

[31] K. Ravi, Seunghyun Lee, Arijit Sharma, G. Werth, and S. A. Rangwala. Combined ion and atom trap for low temperature ion-atom physics. *arxiv-preprint*, 2010.

[32] AA Abrikosov and LP Gorkov. Contribution to the theory of superconducting alloys with paramagnetic impurities. *Soviet Physics JETP-USSR*, 12(6):1243, 1961.

[33] Ali Yazdani, B. A. Jones, C. P. Lutz, M. F. Crommie, and D. M. Eigler. Probing the local effects of magnetic impurities on superconductivity. *Science*, 275(5307):1767–1770, 1997.

[34] SH Pan, EW Hudson, KM Lang, H Eisaki, S Uchida, and JC Davis. Imaging the effects of individual zinc impurity atoms on superconductivity in $Bi_2Sr_2CaCu_2O_{8+\delta}$. *Nature*, 403(6771):746–750, 2000.

[35] E. J. Yarmchuk, M. J. V. Gordon, and R. E. Packard. Observation of stationary vortex arrays in rotating superfluid helium. *Phys. Rev. Lett.*, 43(3):214, Jul 1979.

[36] Y. Sherkunov, B. Muzykantskii, N. d'Ambrumenil, and B. D. Simons. Probing ultracold Fermi atoms with a single ion. *Phys. Rev. A*, 79(2):023604, 2009.

[37] J. Goold, H. Doerk, Z. Idziaszek, T. Calarco, and Th. Busch. Ion-induced density bubble in a strongly correlated one-dimensional gas. *Phys. Rev. A*, 81(4):041601, Apr 2010.

[38] Michał Krych, Wojciech Skomorowski, Filip Pawłowski, Robert Moszynski, and Zbigniew Idziaszek. Sympathetic cooling of the Ba^+ ion by collisions with ultracold Rb atoms: Theoretical prospects. *Phys. Rev. A*, 83(3):032723, Mar 2011.

[39] Pavel Soldán and Jeremy M. Hutson. Interaction of $NH(X^3\Sigma^-)$ molecules with rubidium atoms: Implications for sympathetic cooling and the formation of extremely polar molecules. *Phys. Rev. Lett.*, 92(16):163202, 2004.

[40] Philipp Treutlein, David Hunger, Stephan Camerer, Theodor W. Hänsch, and Jakob Reichel. Bose-Einstein condensate coupled to a nanomechanical resonator on an atom chip. *Phys. Rev. Lett.*, 99(14):140403, 2007.

[41] Eric R. Hudson. Method for producing ultracold molecular ions. *Phys. Rev. A*, 79(3):032716, Mar 2009.

[42] Hauke Doerk, Zbigniew Idziaszek, and Tommaso Calarco. Atom-ion quantum gate. *Phys. Rev. A*, 81:012708, 2010.

[43] A. J. Leggett, S. Chakravarty, A. T. Dorsey, Matthew P. A. Fisher, Anupam Garg, and W. Zwerger. Dynamics of the dissipative two-state system. *Reviews of Modern Physics*, 59(1):1–85, 1987.

[44] A. Recati, P. O. Fedichev, W. Zwerger, J. von Delft, and P. Zoller. Atomic quantum dots coupled to a reservoir of a superfluid Bose-Einstein condensate. *Phys. Rev. Lett.*, 94(4):040404, Feb 2005.

[45] R. Côté and A. Dalgarno. Ultracold atom-ion collisions. *Phys. Rev. A*, 62(1):012709, 2000.

[46] Bo Gao. Universal properties in ultracold ion-atom interactions. *Phys. Rev. Lett.*, 104(21):213201, May 2010.

[47] P. Langevin. *Ann. Chim. Phys.*, 5:245, 1905.

[48] E. Vogt and G.H. Wannier. Scattering of ions by polarization forces. *Phys. Rev.*, 95(5):1190, 1954.

[49] D. L. Albritton, T. M. Miller, D. W. Martin, and E. W. McDaniel. Mobilities of mass-identified H_3^+ and H^+ ions in hydrogen. *Phys. Rev.*, 171(1):94, Jul 1968.

[50] Z. Idziaszek, T. Calarco, and P. Zoller. Controlled collisions of a single atom and an ion guided by movable trapping potentials. *Phys. Rev. A*, 76(3):033409, 2007.

[51] Z. Idziaszek, T. Calarco, P.S. Julienne, and A. Simoni. Quantum theory of ultracold atom-ion collisions. *Phys. Rev. A*, 79(1):010702, 2009.

[52] H.S.W. Massey and C.B.O. Mohr. Free paths and transport phenomena in gases and the quantum theory of collisions. ii. the determination of the laws of force between atoms and molecules. *Proc. Roy. Soc. A*, 144(851):188–205, 1934.

[53] R. Côté. From classical mobility to hopping conductivity: Charge hopping in an ultracold gas. *Phys. Rev. Lett.*, 85(25):5316–5319, Dec 2000.

[54] P. Zhang, A. Dalgarno, and R. Côté. Scattering of Yb and Yb^+. *Phys. Rev. A*, 80:030703, 2009.

[55] A.T. Grier, M. Cetina, F. Oručević, and V. Vuletić. Observation of cold collisions between trapped ions and trapped atoms. *Phys. Rev. Lett.*, 102(22):223201, 2009.

[56] R. Côté, V. Kharchenko, and M. D. Lukin. Mesoscopic molecular ions in Bose-Einstein condensates. *Phys. Rev. Lett.*, 89(9):093001, 2002.

[57] R. V. Krems. Cold controlled chemistry. *Phys. Chem. Chem. Phys.*, 10:4079, 2008.

[58] E.A. Donley, N.R. Claussen, S.T. Thompson, and C.E. Wieman. Atom-molecule coherence in a Bose-Einstein condensate. *Nature*, 417:529, 2002.

[59] T. Kraemer, M. Mark, P. Waldburger, J. G. Danzl, C. Chin, B. Engeser, A. D. Lange, K. Pilch, A. Jaakkola, H.-C. Nägerl, and R. Grimm. Evidence for efimov quantum states in an ultracold gas of caesium atoms. *Nature*, 440:315, 2006.

[60] K.-K. Ni, S. Ospelkaus, M. H. G. de Miranda, A. Pe'er, B. Neyenhuis, J. J. Zirbel, S. Kotochigova, P. S. Julienne, D. S. Jin, and J. Ye. A High Phase-Space-Density Gas of Polar Molecules. *Science*, 322(5899):231, 2008.

[61] M. Drewsen, A. Mortensen, R. Martinussen, P. Staanum, and J.L. Sørensen. Nondestructive identification of cold and extremely localized single molecular ions. *Phys. Rev. Lett.*, 93:243201, 2004.

[62] Peter F. Staanum, Klaus Højbjerre, Roland Wester, and Michael Drewsen. Probing isotope effects in chemical reactions using single ions. *Phys. Rev. Lett.*, 100:243003, 2008.

[63] S. Willitsch, M.T. Bell, A.D. Gingell, S.R. Procter, and T.P. Softley. Cold reactive collisions between laser-cooled ions and velocity-selected neutral molecules. *Phys. Rev. Lett.*, 100:043203, 2008.

[64] Peter F. Staanum, Klaus Højbjerre, Peter S. Skyt, Anders K. Hansen, and Michael Drewsen. Rotational laser cooling of vibrationally and translationally cold molecular ions. *Nature Physics*, 6:271, 2010.

[65] T. Schneider, B. Roth, H. Duncker, I. Ernsting, and S. Schiller. All-optical preparation of molecular ions in the rovibrational ground state. *Nature Physics*, 6:275, 2010.

[66] David Smith. The ion chemistry of interstellar clouds. *Chemical Reviews*, 92(7):1473–1485, 1992.

[67] B. Roth, P. Blythe, H. Wenz, H. Daerr, and S. Schiller. Ion-neutral chemical reactions between ultracold localized ions and neutral molecules with single-particle resolution. *Phys. Rev. A*, 73:042712, 2006.

[68] E.L. Raab, M. Prentiss, A. Cable, S. Chu, and D.E. Pritchard. Trapping of neutral sodium atoms with radiation pressure. *Phys. Rev. Lett.*, 59:2631, 1987.

[69] T. Esslinger, I. Bloch, and T.W. Hänsch. Bose-Einstein condensation in a quadrupole-Ioffe-configuration trap. *Phys. Rev. A*, 58:2664, 1998.

[70] W. Petrich, M.H. Anderson, J.R. Ensher, and E.A. Cornell. Stable, tightly confining magnetic trap for evaporative cooling of neutral atoms. *Phys. Rev. Lett.*, 74:3352, 1995.

[71] K.B. Davis, M.-O. Mewes, M.A. Joffe, M.R. Andrews, and W. Ketterle. Evaporative cooling of sodium atoms. *Phys. Rev. Lett.*, 74:5202, 1995.

[72] S. Palzer, C. Zipkes, C. Sias, and M. Köhl. Quantum transport through a Tonks-Girardeau gas. *Phys. Rev. Lett.*, 103:150601, 2009.

[73] S. Palzer. *Single Impurities in a Bose-Einstein Condensate*. PhD thesis, University of Cambridge, 2010.

[74] F.G. Major and H.G. Dehmelt. Exchange-collision technique for the rf spectroscopy of stored ions. *Phys. Rev.*, 170:91, 1968.

[75] D.J. Wineland, C. Monroe, W.M. Itano, D. Leibfried, B.E. King, and D.M. Meekhof. Experimental issues in coherent quantum-state manipulation of trapped atomic ions. *J.Res.Natl.Inst.Stand.Tech.*, 103:259, 1998.

[76] D. Leibfried, R. Blatt, C. Monroe, and D. Wineland. Quantum dynamics of single trapped ions. *Rev. Mod. Phys.*, 75(1):281–324, Mar 2003.

[77] S. Gulde. Experimental realization of quantum gates and the deutsch-jozsa algorithm with trapped 40Ca+ ions. 2003.

[78] L. Deslauriers, S. Olmschenk, D. Stick, W. K. Hensinger, J. Sterk, and C. Monroe. Scaling and suppression of anomalous heating in ion traps. *Phys. Rev. Lett.*, 97(10):103007, Sep 2006.

[79] C. Zipkes. Ion trap design. First year report, University of Cambridge, 2008.

[80] M.A. Levine, R.E. Marrs, J.R. Henderson, D.A. Knapp, and M.B. Schneider. The electron-beam ion trap - a new instrument for atomic physics measurements. 1988.

[81] N. Kjaergaard, L. Hornekaer, A. M. Thommesen, Z. Videsen, and M. Drewsen. Isotope selective loading of an ion trap using resonance-enhanced two-photon ionization. *Applied Physics B: Lasers and Optics*, 71:207–210, 2000.

[82] A. Braun, Chr Paape, Chr Balzer, W. Neuhauser, and Chr Wunderlich. Resonance enhanced isotope-selective photoionization of YbI for ion trap loading. *arXiv*, 0712.0969, 2007.

[83] M.J. Madsen. *Advanced Ion Trap Development and Ultrafast Laser-Ion Interactions.* PhD thesis, University of Michigan, 2006.

[84] C.B. Alcock, V.P. Itkin, and M.K. Horrigan. Vapor pressure of the metallic elements. *Canadian Metallurgical Quarterly*, 23, 1994.

[85] D.A. Steck. Rubidium 87 D line data. Technical report, Los Alamos National Laboratory, 2001.

[86] U. Schünemann, H. Engler, R. Grimm, M. Weidemller, and M. Zielonkowskic. Simple scheme for tunable frequency offset locking of two lasers. *Review of Scientific Instruments*, 70:242–243, 1999.

[87] G.C. Bjorklund, M.D. Levenson, W. Lenth, and C. Ortiz. Frequency modulation (FM) spectroscopy. *Applied Physics B*, 32:145, 1983.

[88] L. Ratschbacher. Exploration of an atom-ion hybrid cold matter quantum system. First year report, University of Cambridge, 2010.

[89] T. Stöferle. *Exploring Atomic Quantum Gases in Optical Lattices.* PhD thesis, Swiss Federal Institute of Technology Zurich, 2006.

[90] S. Ejtemaee, R. Thomas, and P.C. Haljan. Optimization of Yb^+ fluorescence and hyperfine-qubit detection. *Phys. Rev. A*, 82(6):063419, Dec 2010.

[91] D.J. Berkeland, J.D. Miller, J.C. Bergquist, W.M. Itano, and D.J. Wineland. Minimization of ion micromotion in a Paul trap. *Journal of Applied Physics*, 83(10):5025–5033, 1998.

[92] R. Blümel, C. Kappler, W. Quint, and H. Walther. Chaos and order of laser-cooled ions in a paul trap. *Phys. Rev. A*, 40(2):808–823, Jul 1989.

[93] N. Akerman, S. Kotler, Y. Glickman, Y. Dallal, A. Keselman, and R. Ozeri. Single-ion nonlinear mechanical oscillator. *Phys. Rev. A*, 82(6):061402, Dec 2010.

[94] S. Garcia. Integrating a fiber-based cavity in a linear paul trap. Report, University of Cambridge, 2010.

[95] J.H. Wesenberg, R.J. Epstein, D. Leibfried, R.B. Blakestad, J. Britton, J.P. Home, W.M. Itano, J.D. Jost, E. Knill, C. Langer, R. Ozeri, S. Seidelin, and D.J. Wineland. Fluorescence during Doppler cooling of a single trapped atom. *Phys. Rev. A*, 76(5):053416, 2007.

[96] R.J. Epstein, S. Seidelin, D. Leibfried, J.H. Wesenberg, J.J. Bollinger, J.M. Amini, R.B. Blakestad, J. Britton, J.P. Home, W.M. Itano, J.D. Jost, E. Knill, C. Langer, R. Ozeri, N. Shiga, and D.J. Wineland. Simplified motional heating rate measurements of trapped ions. *Phys. Rev. A*, 76(3):033411, 2007.

[97] W.H. Press, S.A. Teukolsky, W.T. Vetterling, and B.P. Flannery. *Numerical Recipes in C: The Art of Scientific Computing*. Cambridge University Press, 1992.

[98] F. Dalfovo, S. Giorgini, L.P. Pitaevskii, and S. Stringari. Theory of Bose-Einstein condensation in trapped gases. *Review of Modern Physics*, 71:463, 1999.

[99] A. Ridinger and N. Davidson. Particle motion in rapidly oscillating potentials: The role of the potential's initial phase. *Phys. Rev. A*, 76(1):013421, Jul 2007.

[100] A. Ridinger and C. Weiss. Manipulation of quantum particles in rapidly oscillating potentials by inducing phase hops. *Phys. Rev. A*, 79(1):013414, Jan 2009.

[101] C. Zipkes, L. Ratschbacher, C. Sias, and M. Köhl. Kinetics of a single trapped ion in an ultracold buffer gas. *New Journal of Physics*, 13(5):053020, 2011.

[102] Y. Moriwaki and T. Shimizu. Effect of a heavy collision partner on ion loss from a radio frequency trap. *Japanese Journal of Applied Physics*, 37(Part 1, No. 1):344–348, 1998.

[103] M. Green, J. Wodin, R. DeVoe, P. Fierlinger, B. Flatt, G. Gratta, F. LePort, M. Montero Díez, R. Neilson, K. O'Sullivan, A. Pocar, S. Waldman, D. S. Leonard, A. Piepke, C. Hargrove, D. Sinclair, V. Strickland, W. Fairbank, K. Hall, B. Mong, M. Moe, J. Farine, D. Hallman, C. Virtue, E. Baussan, Y. Martin, D. Schenker, J.-L. Vuilleumier, J.-M. Vuilleumier, P. Weber, M. Breidenbach, R. Conley, C. Hall, J. Hodgson, D. Mackay, A. Odian, C. Y. Prescott, P. C. Rowson, K. Skarpaas, and K. Wamba. Observation of single collisionally cooled trapped ions in a buffer gas. *Phys. Rev. A*, 76(2):023404, Aug 2007.

[104] R.G. DeVoe. Power-law distributions for a trapped ion interacting with a classical buffer gas. *Phys. Rev. Lett.*, 102(6):063001, 2009.

[105] T. Kim. *Buffer gas cooling of ions in a radio frequency quadrupole ion guide*. PhD thesis, McGill University, 1997.

[106] A. Kellerbauer, T. Kim, R.B. Moore, and P. Varfa. Buffer gas cooling of ion beams. *Nucl. Instrum. Methods Phys. Res., Sect. A*, 469:276 – 285, 2001.

[107] S. Schwarz. *Nucl. Instrum. Methods Phys. Res., Sect. A*, 566:233–243, 2006.

[108] J.J. Sakurai. *Modern Quantum Mechanics*. Addison-Wesley, 1994.

[109] http://www.wikipedia.org/.

[110] http://www.bssa.org.uk/topics.php?article=96.

[111] http://www.boedeker.com/vespel_p.htm.

[112] http://www.precision-ceramics.co.uk.

List of Figures